Reduced-Order Modeling and Adaptive Observer Design for Lithium-Ion Battery Cells

by

Damas Wilks Limoge

Submitted to the Department of Mechanical Engineering
in partial fulfillment of the requirements for the degree of

Master of Science

at the

MASSACHUSETTS INSTITUTE OF TECHNOLOGY

June 2017

Author . . . .
Department of Mechanical Engineering
May 12, 2017

Certified by . . . .
Anuradha M. Annaswamy
Senior Research Scientist
Thesis Supervisor

Accepted by . . . .
Rohan Abeyaratne
Chairman, Department Committee on Graduate Theses

Reduced-Order Modeling and Adaptive Observer Design for Lithium-Ion Battery Cells

by

Damas Wilks Limoge

Submitted to the Department of Mechanical Engineering
on May 12, 2017, in partial fulfillment of the
requirements for the degree of
Master of Science

Abstract

This thesis discusses the design of a control-oriented modeling approach to Lithium-Ion battery modeling, as well as the application of adaptive observers to this structure. It begins by describing the fundamental problem statement of a battery management system (BMS), and why this is challenging to solve. It continues by describing, in brief, several different modeling techniques and their use cases, then fully expounds two separate high fidelity models. The first model, the ANCF, was initiated in previous work, and has been updated with novel features, such as dynamic diffusion coefficients. The second model, the ANCF II, was developed for this thesis and updates the previous model to better solve the problems facing the construction of an adaptive observer, while maintaining its model accuracy. The results of these models are presented as well.

After establishing a model with the desired accuracy and complexity, foundational observers are designed to estimate the states and parameters of the time-varying ionic concentrations in the solid electrode and electrolyte, as well as an a-priori estimate of the molar flux. For the solid electrode, it is shown that a regressor matrix can be constructed for the observer using both spatial and temporal filters, limiting the amount of additional computation required for this purpose. For the molar flux estimate, it is shown that fast convergence is possible with coefficients pertaining to measurable inputs and outputs, and filters thereof. Finally, for the electrolyte observer, a novel structure is established to restrict learning only along unknown degrees of freedom of the model system, using a Jacobian steepest descent approach. Following the results of these observers, an outline is sketched for the application of a machine learning algorithm to estimate the nonlinear effects of cell dynamics.

Thesis Supervisor: Anuradha M. Annaswamy
Title: Senior Research Scientist

Acknowledgments

I would like to acknowledge and thank my advisor, Dr. Anuradha Annaswamy, for her expertise and guidance along the course of this research. I would also like to thank Dr. Benjamin Jenkins for his parallel work in adaptive observers applied to the single-particle model, and Pierre Bi for his prior work on the ANCF model allowing for its extension. Finally, I would like to thank my friends and family for their ongoing support.

Contents

List of Figures

List of Tables

Chapter 1

Introduction

With the advent of the mobile information age, the population has demanded energy storage capable of producing the magnitude of power necessary to energize the devices of modernity. The answer has come in the form of high energy density battery cells, used to power myriad technologies. These range from smaller mobile computing devices, such as cellphones and laptops, to the more demanding nature of larger energy sinks, like that of an electric vehicle. However, unlike more physically explicit energy storage devices, where one can calculate the energy potential of a fossil fuel or measure the pressure of a compressed air tank, the exact status of a cell is generally speaking unknown, with a reliance on empirical models or cutting-edge computing means. All of this is done in the interest of providing a safe, reliable means of utility for a cell, while optimizing its performance.

The performance of these cells is an area of intense research, from improving the capacity with new materials to using an algorithmic approach, and it is this research that drives the practical application of the technology to further heights. With respect to algorithms that increase the capabilities of cells, the foundational strength of any given approach is beholden to the quality of the underlying model, another area of research in literature. Only with a high fidelity model can designers begin to have full knowledge of the cell, allowing for advanced approaches to control. This thesis will focus on the construction of accurate models to be used with adaptive methods for estimation.

1.1 Battery Overview

The multitude of cell types allows for a wide variety of applications. In fact, electrochemical battery technology is a long-standing focus, beginning in the first century BCE in the Persian civilization, while the ubiquity of the electrochemical cell came in the late 1700's from the efforts of Luigi Galvani and Alessandro Volta [49]. Since then, the field has grown rapidly, with many types of chemistry leveraging a wide variance in capability. The particular choice of chemistry is dependent on application, with an onus placed on the designer to choose one with more benefits than shortcomings.

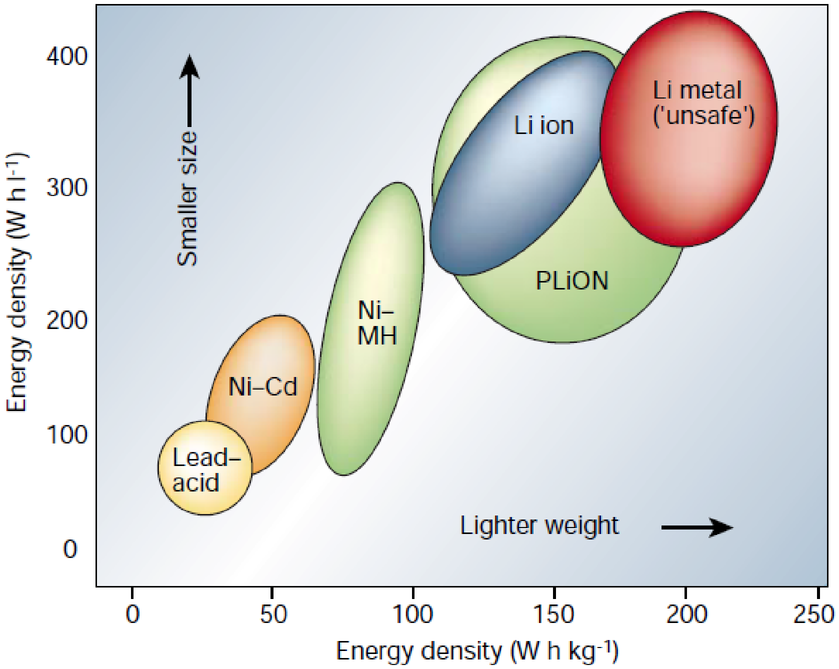

Figure 1-1: A comparison of the energy density of several battery chemistries [56].

A popular chemistry variant is that of the Lithium-ion (Li-ion) battery. These cells provide a high energy density, combined with minimal self-discharge when in an unused state, making them ideal candidates for use in technology as production costs decline [11]. This is depicted in Figure 1-1, showing a comparison of several battery chemistries. It is notable that several common battery types have lower energy densities, such as the Lead-acid batteries found in automobiles, or the Nickel-Cadmium batteries that are common in households. Lithium metal is, however, useful for an anode material as it is the lightest, with an equivalent weight $M = 6.94\,\mathrm{g\,mol^{-1}}$, and has the highest potential, with an electropositivity $\phi = -3.04\,\mathrm{V}$, of any metal [56]. Lithium-ion batteries, therefore, pose a unique opportunity for lightweight, small-size batteries. A distinction is made between a battery pack and an electrochemical cell, whereas battery packs combine several cells for the purpose of higher voltage, in a series orientation, and higher capacity, in a parallel orientation. These packs can be designed through custom means, but often have issues with individual cell health, as a function of imbalance amongst the current state of ion intercalation.

In the simplest terms, a Li-ion cell operates by transferring positively charged Lithium ions from a negative volume (anode) to a positive volume (cathode), in the case of discharge, or a vice-versa for charging, through an electrically insulating material called a separator. These ions are drawn to the opposing side by a potential imbalance, due to the disassociation of electrons in the form of current running through an implicit load, then carried via an electrolyte and intercalate into the opposing solid, working to balance the potential difference between volumes. Figure 1-2 depicts this action, with a nominal load attached to show the transition of electrons.

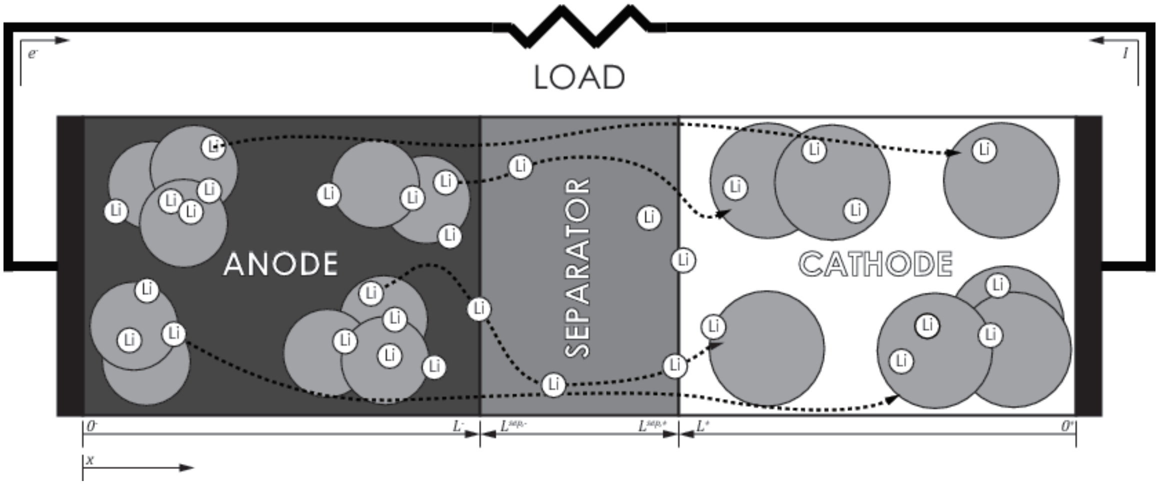

Figure 1-2: An image depicting the function of a Li-ion cell.

Intuitively, the instantaneous capability of a cell is a function of the total Lithium available for intercalation, as well as the parameters which govern the transfer of these ions, the values of which are unmeasurable directly in the normal operation of a cell.

This notion is the motivation for a battery management system (BMS), which tries to track such values to optimize, while maintaining safety, the performance of a cell.

1.2 Motivation for Battery Management Systems

Chapter 2 will discuss the full motivation of developing BMSs, outlining proposed techniques for safe operation of a battery. The purpose of the battery management system is to provide a desired power for a given load, and estimating two defining metrics of a cell's state [11]. The first is state of charge (SoC), which describes the capacity of a cell at a given point, as a function of available Lithium. The second is state of health (SoH), which describes the relative health of a battery, as a function of the degradation of its internal parameters. More explicative definitions of these metrics will be provided in Chapter 2.

The consequences of incorrect assessments of either of these metrics have been shown to be devastating. In recent years, multiple examples of these consequences have manifested in instances of battery packs catching fire, often in high profile circumstances, including the battery fire on-board a Boeing Dreamliner in 2014 [34], the repeated battery fires of the "hoverboard" products in 2015 and 2016 [13], and the battery failures within the Samsung Galaxy Note 7 in 2016 [25]. These are only examples of the last several years, which should make clear the magnitude of the problem faced while handling this technology. Many of these failures have been attributed to manufacturing defects, which is a misestimation of the SoH of a cell, or aggressive use of the batteries, which is a control scheme that does not properly account for the SoC of the cell. With a proper BMS, many of these problems could have been avoided, but the current state of the industry does not integrate complex algorithms into their products. The stakes are even higher when considering the problem from the perspective of an electric vehicle manufacturer. The batteries in use in these automobiles are an order of magnitude or more larger in capacity than a cell phone or a child's toy, thus substantially increasing the risk to users. Conversely, the viability of the technology is dependent on fast charging and discharging, to provide reasonable drive time and power to consumers. If the industry is to advance into the mainstream, it is necessary for new, advanced BMSs to be developed in conjunction with the vehicles themselves. These systems will be reliant on accurate estimates of parameters and states of the cells, using novel electrochemical models as the foundation for their success.

1.3 Modeling Overview

Chapter 3 discusses a variety of approaches and techniques for the modeling of batteries. There are two prevailing architectures of these models, namely simplified approximations that sacrifice intuitive physical parameters for computational simplicity, and complex electrochemical models that generate high accuracy with many parameters. There are virtues and shortcomings to either approach, and it is the responsibility of the BMS designer to choose, with a-priori knowledge, what the expected model needs to be capable of handling.

The simplified approximation approach generally relies on creating a model using a non-physical facsimile of the dynamics of the cell, understanding that the diffusion and potential characteristics can be abstracted to provide tractable computational complexity. One such model is the Kinetic Battery Model [46], while another is any variety of Equivalent Circuit Model [59] [28], both of which will be discussed further in Chapter 3. The alternative approach, an electrochemical model, is based on physical descriptions of the diffusion and potential within the cell. A popular foundation for these models is the Doyle-Fuller-Newman (DFN) variant [15] [14], which is an oft implemented model using several partial differential equations and an algebraic constraint to describe the system. There are several instances in literature of using the DFN model with other model order reduction techniques [31] [33] [7] [8], which will be elaborated in Chapter 3, but one technique that remains popular for its retention of physical parameters is the single particle model [41] [48] [47]. This is the coarsest simplification of the DFN, and assumes no ionic variation in the electrolyte.

Finally, Chapter 3 reviews the novel modeling contributions made by this thesis and its predecessor [5], known as the ANCF and ANCF II models. These models incorporate third-order polynomial descriptions of the physical dynamics, while also maintaining a minimal number of states and parameters for subsequent use in an adaptive observer. The intention behind these models is to match the voltage output of the battery at high charging and discharging levels, while also maintain the few parameters mentioned. This is achieved, in the ANCF, with excellent accuracy of simulation results, and the third-order polynomial basis function representation of concentrations and the algebraic constraint. Pushing the minimal states to their limit, the importance of which will be discussed with adaptive observers, the ANCF II utilizes a mixed basis function technique, with linear basis functions for states that are less susceptible to high order dynamics, while maintaining the third-order polynomial for concentrations with high gradients. Around this second model, a set of adaptive observers are created, in the interest of state and parameter estimation.

1.4 Adaptive Observer Overview

Chapter 4 discusses the application of adaptive observers to the models established in Chapter 3. Adaptive observers have been in literature [37] for some time now, but their application to battery models is nascent. The premise of adaptive observers is the creation of an equivalent system, which uses both the inputs and the outputs of a system, filtered to create a regressor. This regressor has associated parameters that can define the nonminimal form of the system, which includes parameters for all coefficients of the associated transfer function's numerator and denominator. Therefore, with the proper input and output signals, the full system can be estimated, including the states and parameters of the system matrices.

The first presentation of the adaptive observer in Chapter 4 is an establishment of the notation for the equivalent system in the vector regressor form. The distinction here is that a single regressor vector has its own associated single-input, single-output system, with a set of parameters unique to that system. This system has shown successful results [6], but often relies on a very high order of persistent excitation for successful convergence, as well as adaptive gains. This latter portion contributes an additional N integration terms to the already $2N+1$ parameters of the nonminimal system, without additional linearly independent regressor terms which makes the simulation cumbersome.

The second presentation of the adaptive observer builds on the first implementation by creating a matrix regressor. In short, this matrix is similar to the vector regressor, but instead, each column represents a filtered form of the equivalent system, to create a matrix with a rank greater than or equal to the number of nonminimal parameters, $2N+1$. If a proper filter is chosen, this requires less persistent excitation of the equivalent system, and is therefore more enticing of an option for creating observers on highly unknown systems.

Finally, this observer structure is built around the ANCF II model. The model is separated in such a way as to allow separate observers to be used for the electrolyte and solid electrode dynamics, utilizing the matrix regressor form for each. Results for this research are shown, with novel techniques in many facets. This approach has many challenges, given the structure of the model, and the required assumptions needed for the observers to operate. Parts of the system are unobservable at certain points, and therefore, the sensitivity of the observers needs to be adjusted. Future work needed for the successful implementation of these observers is also discussed, as it relates to the topic of machine learning.

1.5 Preliminary Summary of Results and Contributions Made

The major contributions of this thesis can be seen in Chapters 3 and 4. With respect to modeling, this thesis contributed to both the ANCF model, by way of removing an ad-hoc determination of the electrolyte diffusion coefficient that made it difficult to run varying simulation input profiles without a calculation of the diffusion coefficient a-priori, as discussed in Section 3.4. Furthermore, this thesis contributed an additional reduced-order model that identified the portions of the dynamics in need of a high order basis function, while eliminating the additional terms for less dynamic states. This approach is discussed at length in Section 3.5, and it is shown that a comparable accuracy is achieved, with results established in Tables 3.2 and 3.3.

After establishing the accuracy of the ANCF II model in Chapter 3, Chapter 4 describes the design and construction of adaptive observers applied to this model. In Section 4.3.1, a novel observer is constructed using the matrix-regressor approach established in literature, but combining the temporal filters with spatial filters. In Section 4.3.2, a novel approach to making an a-priori estimate of the molar flux is established, using measurements of output voltage, input currents and filters of the latter. Finally, in Section 4.3.3, a completely new adaptive observer approach is derived using a directed Jacobian parameter update for a subset of parameters that represent the physical unknowns of a system within a known model structure. This method is inspired by gradient descent algorithms, but is implemented on-line for parameter and state estimation.

Chapter 2

Battery Management Systems

The role of the battery management system (BMS) is to provide on-line, accurate estimations of two distinct metrics of the status of a cell, as discussed briefly in Chapter 1.2. These metrics are the state of charge (SoC), a description of the capacity of the battery at a given state of ion intercalation, and the state of health (SoH), a description of the relative degradation of parameters of a cell over time. These two metrics can be used to define control schemes for a cell, as well as anticipate when a battery must be replaced.

There are many instantiations of the BMS, ranging in sophistication from simplistic, linearized models, to advanced versions that incorporate state of the art methods for measuring the SoC and SoH. A block diagram of a BMS is shown in Figure 2-1, highlighting the use of available measurements for purposes of state identification. The choice of implementation is often determined by the specific application, for example, devices that pull small currents from a battery, such as a cellphone, do not need to rely on advanced battery management systems, as the dynamics of the battery under those conditions can generally operate within the linear range of cell dynamics. This often means that the battery is over-sized for the necessary capacity, to avoid entering the fringe conditions of the operation of the cell. These fringe conditions are, in fact, nonlinear, and therefore require a more complex algorithm to safely operate within. This, however, limits the ability to charge the battery at a high rate, as intuition suggests. Conversely, if the operating conditions of the cell are of a high

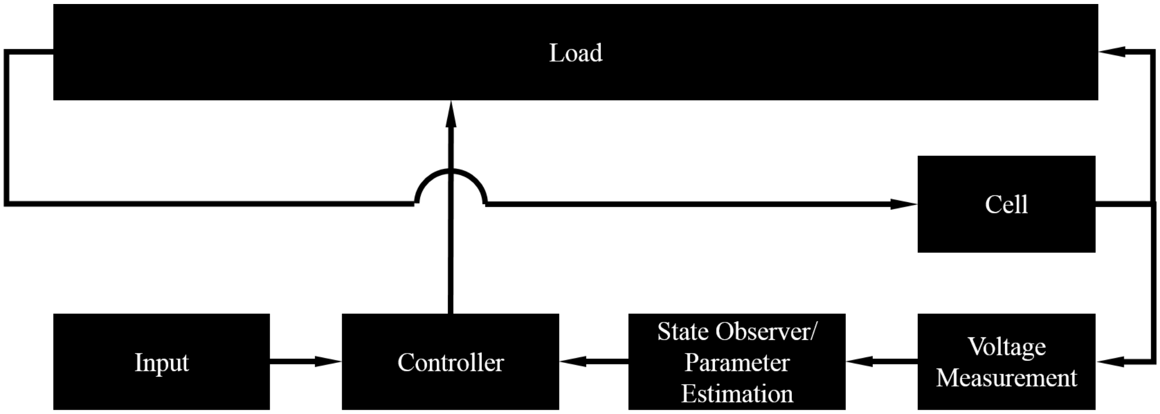

Figure 2-1: A block diagram of a battery management system in operation with cell measurements.

magnitude, such as that of an electric vehicle (EV), the need for a more advanced BMS becomes apparent. Low estimates, with an assumption of low gasoline prices and constant EV cost, predict a market share of 60% by 2040 for EV's [51], over the current share of <0.1% of plug-in EV's worldwide [45]. This represents a huge challenge, as the success of the EV market is highly sensitive to the cost of the vehicle, as well as the preference of vehicle cost for a consumer [51]. One of the primary drivers of an EV's cost is the battery, and the two approaches for reducing this cost include improved electrochemical capacities, which have been recognized in significant ways with a 14% annual reduction in costs between 2007 and 2014 [42], and sophisticated means of identifying the SoC and SoH of a battery pack.

2.1 State and Parameter Identification Problem

The role of a BMS is a nominally simple one: to predict the status of a battery pack through two metrics, those of SoC and SoH, ensuring safe use and operation of the cell while optimizing the performance through informed control schemes. The difficulty comes in the observability of these metrics, as they are not directly measurable outside of a laboratory setting. This motivates the need for estimation of the states and parameters of a cell, to fully characterize its status at a given time. The metric of SoC is a measurement that denotes the intercalated lithium in a solid particle at its surface, normalized by the maximum capacity of that solid, defined as local utilization. This is a measurement of the charge available in the solid electrode, analogous to a fuel gauge in a vehicle. Because the total quantity of lithium ions in the cell is conserved, albeit in the electrolyte as well as the solid, it is sufficient to calculate the SoC of a single volume, namely the anode or cathode [11]. Within the duration of a charge cycle, this is a rapidly varying state that is dependent on the diffusion of ions into the solid particles, as a function of current and cell potentials. The accurate estimation of the SoC is highly valuable, as it ensures that a cell can be operated within its safe limits without being oversized. Specifically, if the SoC is underestimated, the capacity of a cell is underutilized, while if the SoC is overestimated, the cell can be discharged or charged past its safe limits. Therefore, the accurate estimation of the SoC is driven by the desire for reducing the cost of a battery under a notional load cycle, as well as safe operation within that cycle.

Conversely, the SoH is a slow-changing metric that defines the degradation of physical parameters of the cell over its lifetime. This value is often attributed to two causations [35]: capacity fade of the cell, as a function of the fraction of the cell volume available for intercalation, as well as the increase of impedance due to the internal ohmic resistance of the cell, known as interphase resistivity. The phenomenon of changing SoH is characterized by long timelines, much longer than that of the change in SoC, with nominal capacity reduction of a cell reaching 25% after two years [35]. A higher impedance reduces the available power discharge, as well as increases the heat dissipation within the cell, causing potentially a 20% reduction in power availability [35]. At some point this degradation becomes untenable, motivating a cell to be recycled, but without a way of estimating SoH, this threshold is left to the intuition of users and a heuristic approach relying on expected degradation or servicing time to determine the health of a battery offline. Without a quantitative measurement to support this decision, users of electric vehicles or other devices containing batteries may be frustrated with the unacceptably low capacity of the battery, or exposed to the dangerous potential of charging or discharging past the safe limit of a battery. Therefore, regardless of the application, some sort of BMS is needed, even in its most simple form, to ensure the usability of these products. These exist, and can be used to some success, assuming the battery remains within a fairly benign operational subset.

2.2 Simplified Monitoring Systems

In the interest of simplicity, many monitoring systems have been proposed to abstract much of the complex dynamics of the cell, as discussed in Chapter 1 and extrapolated in Chapter 3. These models maintain the simplest form of cell dynamics, while allowing an easy implementation for designers. One such method is called "coulomb counting" [40] [43], and is presented as a juxtaposition to the BMS implementation discussed in detail throughout this thesis. The notation of a battery model will be established more significantly in Chapter 3, but the elementary form is presented herein, hopefully without the loss of clarity. As discussed in Section 2.1, the SoC is a metric describing the local utilization. As such, this is a ratio of the concentration in a solid particle, as a function of its location in space, x; the point of interest on the radius of the particle, r; the time of interest, t; and the maximum concentration possible in that sphere, $c_{s,max}$. Of course, this means there are infinite SoCs across the cell, at every conceivable point within the sphere.

To aggregate this data into a measurable value, a bulk utilization is defined [11], as in Equation (2.1),

$$SOC^{\pm}(t) \triangleq \frac{3}{L^{\pm}\left(R_p^{\pm}\right)^3} \int_{0^{\pm}}^{L^{\pm}} \int_{0}^{R_p^{\pm}} r^2 \frac{c_s^{\pm}(x,r,t)}{c_{s,max}^{\pm}} dr dx \tag{2.1}$$

where $SOC^{\pm}(t)$ denotes the SoC of the anode $(-)$ or cathode $(+)$, $L^{\pm}$ denotes the length of the volume of the electrode, as shown in Figure 1-2, $R_p^{\pm}$ is the full radius of the particle, r is the specific position on the radius, $c_s^{\pm}(x,r,t)$ is the solid concentration and $c_{s,max}^{\pm}$ is the theoretical capacity of the cell. In this form, SoC is still not directly measurable, however the form can be altered to be estimable by an accurate measurement of current [43], as shown in Equation (2.2).

$$SOC^{\pm}(t) = SOC^{\pm}(t_0) \mp \int_{t_0}^{t} \frac{I(\tau)}{cap^{\pm}} d\tau \tag{2.2}$$

$SOC^{\pm}(t_0)$ is the initial value of the SoC, while $I(\tau)$ is the current profile over time, and $cap^{\pm}$ is the nominal capacity of the battery during the experiment. By measuring the open-circuit potential of the cell, one can determine the initial SoC, $SOC(t_0)$, and with accurate current measurements, determine the bulk SoC of a cell. However, the nominal capacity is a measurement of the degraded capacity from the theoretical capacity. This can be determined by charging and discharging the cell between preset voltages, and measuring the amount of time until it reaches those points. This is inconvenient to do regularly, but can be achieved. Subsequently, since the measurement is an integration of the current, errors tend to accumulate based on minimal measurement noise, leading to inaccurate estimates. Subsequently, the nominal capacity is used as a definition of SoH, such as shown in Equation (2.3) [40],

$$SOH^{\pm} \triangleq \frac{cap^{\pm}}{c^{\pm}_{s,max}} \times 100\% \tag{2.3}$$

where $SOH^{\pm}$ is the SoH of the anode or cathode. Using Equations (2.2) and (2.3), one can generate a rudimentary BMS, but the sensitivity to highly accurate current measurements and offline data does not engender confidence for high fidelity estimates. Furthermore, a bulk SoC ignores the potential for concentration gradients, which are possible with severe current profiles, and pose an equal threat of over-charging or discharging in a localized area of the cell. Instead, a more advanced means of estimation is necessary to ensure a more refined approach.

2.3 Advanced Battery Management Systems

The primary difference between an advanced battery management system (ABMS) and the conventional implementation of a BMS is the inclusion of an electrochemical model [11], as shown in Figure 2-2. Instead of relying on high-level abstractions, the

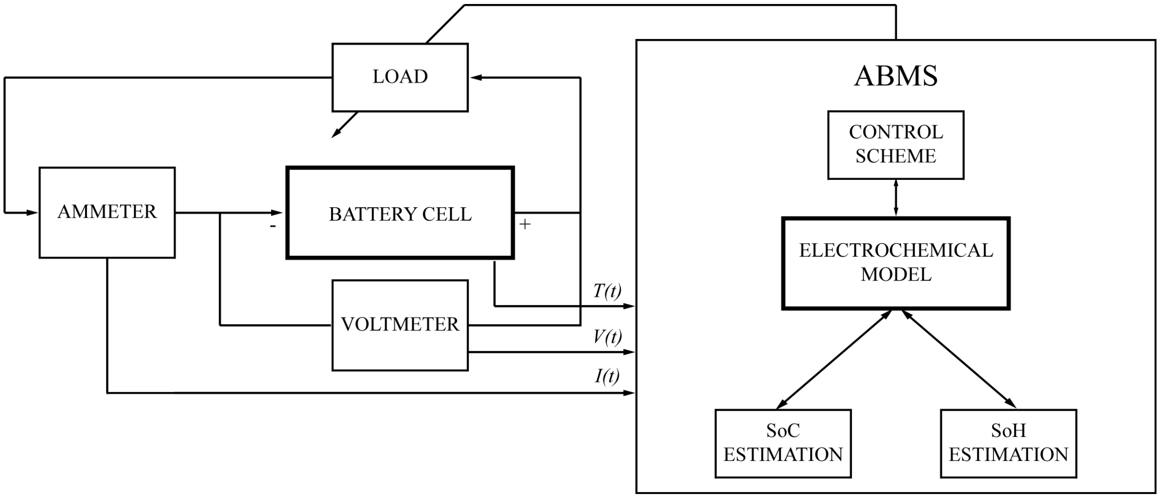

Figure 2-2: A block diagram of an advanced battery management system in operation with cell measurements and inclusive of an electrochemical model.

states of the battery are directly tracked using observers to inform more nuanced control approaches. Often, a standard BMS relies on set voltage and current limits, such that,

$$\begin{aligned} V_{min} \leq & V(t) \leq V_{max} \\ I_{min} \leq & I(t) \leq I_{max} \end{aligned} \tag{2.4}$$

where V_{min} and V_{max} represent the low and high voltage limits, respectively; I_{min} and I_{max} represent the discharging and charging current limits, $V(t)$ is the measured voltage of the cell, and $I(t)$ is the measured current through the cell. These bounds are often based on empirically defined safety limits, but have the effect of limiting the capacity, as shown in Figure 2-3, or, after years of parameter degradation, allowing operation outside of a truly safe range, as shown in the evolution of Figure 2-3 by the hypothetical representation in Figure 2-4. Understanding the true capacity of a battery at any time, allows for more properly sized cells for a given purpose, reducing weight and cost, while also having stronger guarantees on safety.

Beyond ensuring that the safe operating limits are known accurately, as determined by the SoC in conjunction with the SoH, it also possible to limit the type of operating conditions that encourage the degradation of parameters leading to the

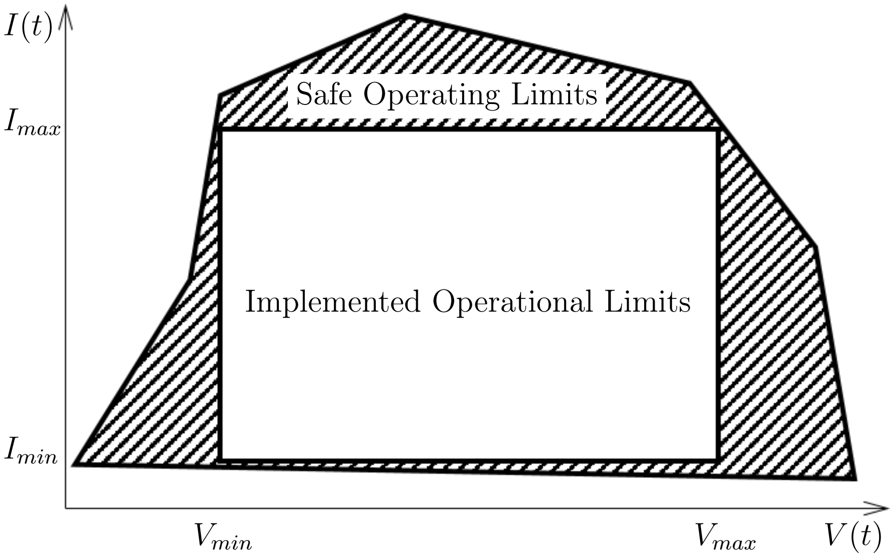

Figure 2-3: Depiction of the capacity limits imposed by constant bounds of voltage and current operation. The white box represents the standard BMS, while the cross-hatch shows a hypothetical safe operating range outside of the conventional implementation.

depiction shown in Figure 2-4. A more rigorous explanation of the notation is presented in Chapter 3, but the underlying concept is that new features of the cell can be considered with the use of an ABMS. One such occurrence is lithium plating of the electrode on the surface of the solid particle [3], as caused by an overpotential side reaction. The overpotential is defined as,

$$\eta_{sr}(x,t) = \phi_s(x,t) - \phi_e(x,t) - \mathcal{U}(x,t) - R_f(x,t)j(x,t) \tag{2.5}$$

where $\eta_{sr}(x,t)$ is the overpotential of a side reaction of the cell, $\phi_s(x,t)$ is the solid potential of the cell, $\phi_e(x,t)$ is the electrolyte potential of the cell, $\mathcal{U}(x,t)$ is the open-circuit potential of the cell, $R_f(x,t)$ is the film resistance and $j(x,t)$ is the molar flux. For simplicity purposes, we can eliminate $R_f(x,t)j(x,t)$, as the molar flux is much less than zero, or $|j(x,t)| \approx 0$. Additionally, for side reactions, the overpotential is also zero, $\mathcal{U}(x,t) = 0$, and therefore the overpotential for this particular case is considered as shown in Equation (2.6).

$$\eta_{sr}(x,t) = \phi_s(x,t) - \phi_e(x,t) \tag{2.6}$$

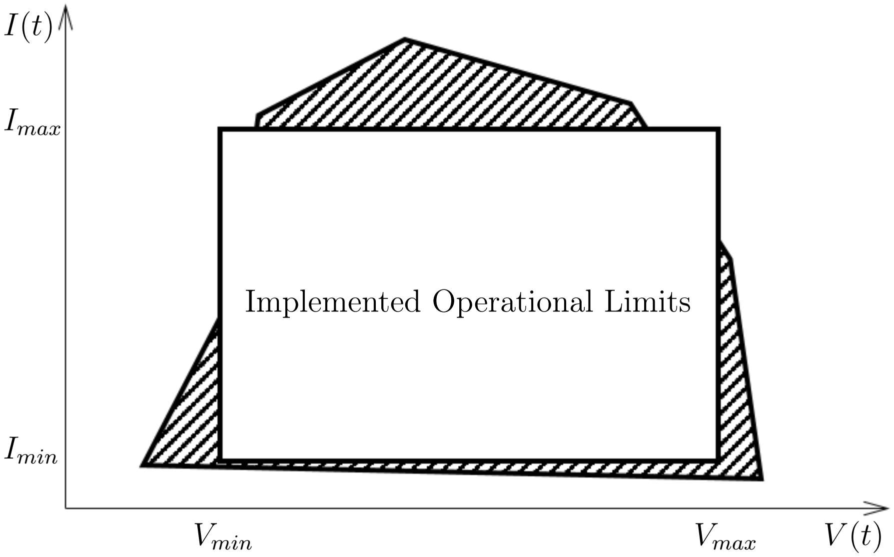

Figure 2-4: The time evolution of Figure 2-3 over several years, where parameter degradation has limited the safe operational range to less than that imposed by the constant limits. Again, the white box represents the standard BMS, while the cross-hatch shows the hypothetical safe operating range.

Using this definition of the side reaction overpotential, a simple control constraint available only to an ABMS can be defined as shown in Equation (2.7).

$$\eta_{sr}(x,t) > 0 \tag{2.7}$$

This definition applies to all points in the cell, and only by identifying the states across the cell, instead of a bulk SoC, is this control scheme possible, thus reducing the fatigue stress of a cell. Therefore, as discussed as the fundamental distinction between a BMS and an ABMS, a strong, control-oriented model must be developed as the foundation for any parameter or state identification. Modeling is a well-discussed element of the literature regarding Li-ion batteries, and is covered in Chapter 3.

Chapter 3

Battery Modeling

At the heart of advanced monitoring systems is an implementation of a high fidelity battery model to match the dynamics of the measured inputs and outputs. By using an effective model, the management of the cell has a higher fidelity with the internal states of the actual cell. The difficulty is in finding the balance between a model with a few number of states, allowing for tractable observer construction, while also maintaining the appropriate degrees of freedom to allow for accurate simulation. A wide swath of literature is focused on adjusting this problem with myriad strategies.

This chapter will address the state of various models in literature, with a focus on the progress made by this research. Section 3.1 summarizes the structure of a battery, as discussed previously in Section 1.1. Section 3.2 discuss non-physical approximations, such that the dynamics are established with analogous systems, as opposed to the underlying electrochemical properties. Section 3.3 discusses electrochemical models, with a specific focus on the Doyle-Fuller-Newman model. This section also focuses on the model-order reduction techniques, with a highlight on the solution to the Single Particle Model. Section 3.4 discusses the culmination in work by the author and a previous graduate student in developing a battery model for control purposes, while Section 3.5 discusses an extension of this model to fix some of its limiting issues in the observer models. Finally, Section 3.6 shows validation efforts for the models, and draws comparisons between them, as well as distinctions.

3.1 Battery Structure

The underlying principles of the Li-ion battery cell that are the focus of a given model is the available energy, as a function of lithium concentrations, for discharge or charge. The diffusion principles are assumed to be the same for either charging or discharging, with only a change in sign of the input current. The role of a battery model is to replicate these diffusion principles as closely as possible to a real cell, while also maintaining design constraints regarding computational complexity. Therefore, the structure is separated into three distinct volumes, that of the anode, a negatively charged volume; the cathode, a positively charged volume; and the separator, an electrically insulating volume that allows the passage of ions, but not charge. Through this structure, the passage and concentrations of ions is enabled by the transfer mechanism of an electrolyte, which define the state metrics described in Section 2.1. Frequently, the dynamics are normalized against a singular, dominant direction, called the x-direction, for purposes of simplification. This then allows the designer to focus solely on the bulk reactions in this direction, instead of relying on a 3D model beholden to precise geometric measurements of vastly varying scales. However, the underlying desire of these models is still to replicate voltage as a function of current, or vice-versa, which allows for models that are completely agnostic of electrochemical diffusion principles.

3.2 Analogous System Approximations

In the interest of simplifying the dynamics of a battery cell, approximations have been developed that abstract the electrochemical diffusion discussed in Section 3.3. The advantage of these models is a clear grasp on the time-dependent dynamics of the model, while having sufficient replication of the battery output. Generally speaking, there are limitations to these models at higher discharge rates, but can be suitable for the complex simulation of electrical grids and large battery packs. Section 3.2.1 discusses the equivalent circuit model, an approximation based on a circuit representation of the cell that uses various parallel and series impedance to reproduce the dynamics. Section 3.2.2 discusses the kinetic battery model, which uses an analogous system of two volumes, one that represents the energy available for use, and the other representing the difference in total available charge. These types of models are frequently used, but the presentation of them is not exhaustive of the variety of analogous system approximations.

3.2.1 Equivalent Circuit Model

Equivalent circuit models are prevalent in literature [20], with myriad approaches. The premise is to devise a battery model that replicates the performance of a cell using common circuit components. The advantage in this approach is elements that are easy to model, extraordinarily well understood, and subsequently easy to parameterize for empirical fitting. This section will cover a simple approach to the modeling strategy [58], and also examine an extension of that approach [21].

An early attempt at the equivalent circuit model [59] is that of the first order RC circuit, as shown in Figure 3-1. The voltage of the cell is denoted as V_c, and is a function of an open-circuit potential, V_0, and an overpotential due to the impedance of internal resistances. The mathematical representation begins with Kirchoff's law,

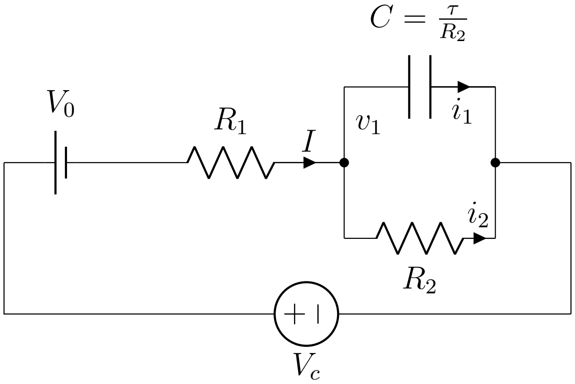

Figure 3-1: Equivalent circuit model for empirically fitted parameters to simulation data [59].

as a sum of currents such that,

$$I = i_1 + i_2 \tag{3.1}$$

Subsequently a definition of each of the currents is established,

$$\begin{aligned} i_1 &= C\frac{dv_1}{dt} \\ i_2 &= \frac{v_1}{R_2} \end{aligned} \tag{3.2}$$

These are then substituted back into Equation (3.1), to yield,

$$I = \frac{v_1}{R_2} + C\frac{dv_1}{dt} \tag{3.3}$$

with an equivalent representation in the Laplace domain,

$$\frac{I(s)}{\frac{1}{R_2} + Cs} = V_1(s) \tag{3.4}$$

To solve for the overpotential, $V_c - V_0$, the final relationship in the Laplace domain is established, substituted with Equation (3.4),

$$\begin{aligned} V_c(s) - V_0 - \frac{I(s)}{\frac{1}{R_2} + Cs} &= I(s)R_1 \\ \frac{V_c(s) - V_0}{I(s)} &= \frac{R_1R_2Cs + R_1 + R_2}{R_2Cs + 1} \end{aligned} \tag{3.5}$$

Then, by fitting the parameters V_0, R_1, R_2 and C to empirical data, the model is representative of the dynamics of a battery cell. It should be noted that either a voltage profile, V_c, or a current profile can be used as an input for this model.

The simple equivalent circuit shown in Figure 3-1 was extended, as shown in Figure 3-2 [21]. Each additional filter, for $i = [1 \ldots n]$, has an associated voltage drop across the elements, $V_i = v_i - v_{i+1}$, defined by Equation (3.6).

$$\frac{dV_i}{dt} = \frac{1}{R_iC_i}V_i + \frac{1}{C_i}I \tag{3.6}$$

A hysteresis factor, V_h, is defined as,

$$\frac{dV_h}{dt} = \Gamma(T)|I|(H(z, \mathrm{sgn}(\dot{z}), T) - V_h) \tag{3.7}$$

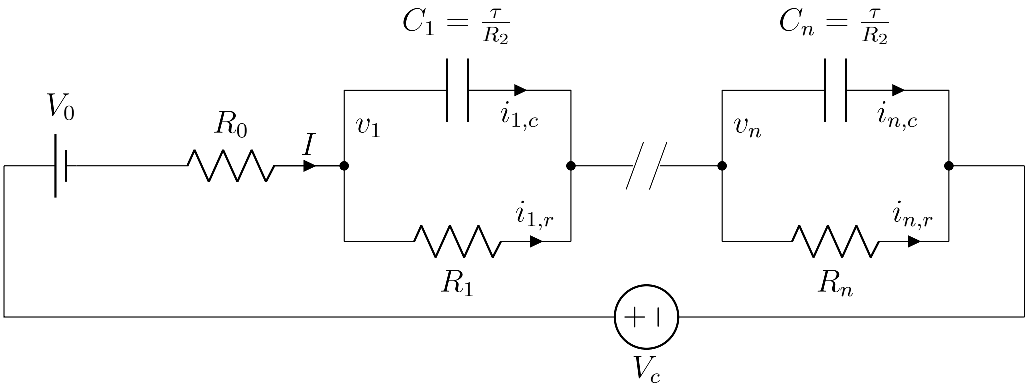

Figure 3-2: Extended equivalent circuit model [21].

where $\Gamma(T)$ is a hysteresis coefficient as a function of temperature, T; and H is a maximum hysteresis value as a function of the SoC, shown as z in this notation, and the temperature, T. This hysteresis value is used to correct for the difference in charging and discharging dynamics. Subsequently, the full cell voltage can be defined as shown in Equation (3.8).

$$V_c = V_0 - R_0 I - \sum_{i=1}^{n} V_i - V_h \tag{3.8}$$

These models have been proposed with corrections made for temperature effects and hysteresis. The downside is an inability to estimate parameters, as the model is dependent on constant recalibration, and abstracts the value of SoC, relying on the coulomb-counting discussed in Section 2.2. A model that attempts to correct this latter shortcoming, but still maintains the benefits of a highly simplified structure, is the Kinetic Battery Model.

3.2.2 Kinetic Battery Model

The Kinetic Battery model (KiBaM) has been present for several decades, and was originally designed for use with lead-acid batteries [30]. The concept has recently been applied to Li-ion batteries [46], and is used in modeling microgrid control algorithms [60]. The advantage of the KiBaM is its analytically simple derivation, and use of an analogous mechanical system formulation. An image of this formulation is shown in Figure 3-3. The qualitative notion of the model is two reservoirs that dictate the charge of the system. Tank 1 has a width, C, that is available for use, while tank 2 has the unity difference width, $1 - C$. Their heights are denoted with q_1 and q_2 for tank 1 and tank 2, respectively, and their maximum height is bound by q_m. There is an impedance between tanks, k', as well as before discharge, R_0. The dynamics are governed by two expressions, shown in Equation (3.9).

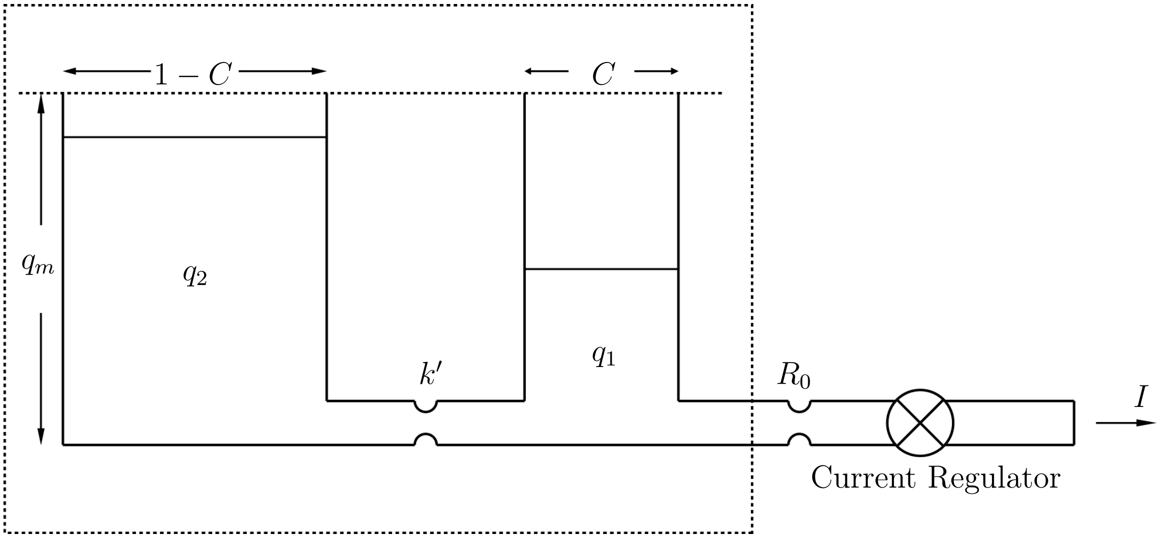

Figure 3-3: A graphical depiction of the kinetic battery model, as presented in literature [30].

$$\begin{aligned} \frac{dq_1}{dt} &= -I - k'(h_1 - h_2) \\ \frac{dq_2}{dt} &= k'(h_1 - h_2) \end{aligned} \tag{3.9}$$

Where the heights of the tanks, h_1 and h_2, are defined as,

$$\begin{aligned} h_1 &= \frac{q_1}{C} \\ h_2 &= \frac{q_2}{1 - C} \end{aligned} \tag{3.10}$$

Subsequently, the impedance, k, is normalized for mathematical convenience,

$$k = \frac{k'}{C(1 - C)} \tag{3.11}$$

Substituting these expressions into Equation (3.9) yields,

$$\begin{aligned} \frac{dq_1}{dt} &= -I - k(1-C)q - 1 + kCq_2 \\ \frac{dq_2}{dt} &= k(1-C)q_1 - kCq_2 \end{aligned} \tag{3.12}$$

For each instance of the model, the current is calculated as a $I = P_{need}/V_{sys}$, where the battery voltage is assumed to be at the system level.

This particular model formulation is well suited for applications where the voltage is well determined, such as that from power generation units in a microgrid. It does not, however, allow for both SoC estimation and SoH estimation, and needs, as the ECM models do, to be fit empirically to models first. The thematic shortcomings of these models pertain to a lack of physical parameters that allow for simultaneous SoC and SoH estimation. To correct these problems, many instances in literature have sought to better demonstrate battery dynamics with electrochemical models. The extent of these models, as well as methods for model order reduction, are discussed in Section 3.3.

3.3 Electrochemical Models

The basic dynamics captured by electrochemical lithium-ion models can be considered as the reversible transport of lithium ions from a negatively charged volume (anode) to a positively charged volume (cathode). The transport mechanism is an electrolyte, that passes through an electrically insulating porous separator, which allows the passage of ions between volumes, but not an exchange of charge. The difference in potential of these volumes is the driving electrical force in the implicit circuit, while the diffusion of the lithium particles can most simply be considered as a function of the resulting current. The resulting physical ports of such a system are voltage, current and temperature. A widely used model in the field of ABMS research is the Doyle-Fuller-Newman model.

3.3.1 Doyle-Fuller-Newman Model

The Doyle-Fuller-Newman (DFN) analytical model [15] [57] combines a series of PDE equations with an algebraic constraint due to the reaction kinetics. Also referred to as the pseudo two dimensional (P2D) model, the DFN model considers reaction dynamics in the Li-ion cell along the x-axis, and a radial dimension, r, along which the electrode volumes are discretized into spherical solids, such as that shown in Figure 1-2. The dynamics of the lithium concentration in the solid electrode along the radius of the pseudo-sphere, $c_s^{\pm}(x, r, t)$, where the superscript $\pm$ denotes the specific volume in the anode and cathode, respectively, can be defined as,

$$\frac{\partial c_s^{\pm}(x,r,t)}{\partial t} = \frac{1}{r^2}\frac{\partial}{\partial r}\left(D_s^{\pm} r^2 \frac{\partial c_s^{\pm}(x,r,t)}{\partial r}\right) \tag{3.13}$$

where $D_s^{\pm}$ denotes the solid diffusion coefficient. The boundary conditions for this expression are shown below as,

$$\begin{aligned} \left.\frac{\partial c_s^{\pm}(x,r,t)}{\partial r}\right|_{r=0} &= 0 \\ \left.\frac{\partial c_s^{\pm}(x,r,t)}{\partial r}\right|_{r=R_p^{\pm}} &= -\frac{j(x,t)}{D_s^{\pm}} \end{aligned} \tag{3.14}$$

Similarly, the resulting dynamics in electrolyte concentration, $c_e(x, t)$, can be defined by,

$$\frac{\partial c_e(x,t)}{\partial t} = \frac{\partial}{\partial x}\left(\left(D_e(x,t)\frac{\partial c_e(x,t)}{\partial x}\right) + \frac{t_a^0}{F\epsilon_e} i_e(x,t)\right) \tag{3.15}$$

where $D_e(x, t)$ denotes the electrolyte diffusion coefficient as a function of electrolyte concentration; F, the Faraday constant; ϵ_e, the electrolyte volume fraction; t_a^0, the transference number of the anions; and $i_e(x, t)$, the electrolyte current, as defined by,

$$\frac{\partial i_e(x,t)}{\partial x} = a_s^{\pm} F j(x,t). \tag{3.16}$$

In Equation (3.16), $a_s^{\pm}$, denotes the specific electrode interfacial area. The molar flux,

$j(x,t)$, is given by an expression known as the *Butler-Volmer reaction kinetics* [39], which relates the molar flux to the overpotential of the cell,

$$j(x,t) = \frac{i_0(x,t)}{F}\left(\exp\left(\frac{\alpha_a F}{RT}\eta^{\pm}(x,t)\right) - \exp\left(-\frac{\alpha_c F}{RT}\eta^{\pm}(x,t)\right)\right) \tag{3.17}$$

where $\alpha_{a/c}$ is the transfer coefficient for anions/cations. If the transfer coefficient is equal to 0.5 for both cations and anions, a common assumption, the exchange current density, $i_0(x,t)$, is defined by,

$$i_0(x,t) = k_{eff}\sqrt{c_{ss}^{\pm}(x,t)c_e(x,t)\left(c_{s,max}^{\pm} - c_{ss}^{\pm}(x,t)\right)} \tag{3.18}$$

where k_{eff} is the effective reaction constant, $c_{ss}^{\pm}$ is the solid concentration at the surface of the pseudo-sphere, or $c_{ss}^{\pm} = c_s^{\pm}(x, R_p, t)$, where R_p is the full radius of the pseudo-sphere, and $c_{s,max}^{\pm}$ is the maximum concentration of the solid electrode. The overpotential, $\eta^{\pm}(x,t)$, is given by,

$$\begin{aligned} \eta^{\pm}(x,t) =& \phi_s^{\pm}(x,t) - \phi_e(x,t) \\ & - \mathcal{U}^{\pm}(c_{ss}^{\pm}) - FR_f^{\pm} j(x,t) \end{aligned} \tag{3.19}$$

which depends on the volume's open circuit potential (OCP), $\mathcal{U}^{\pm}(c_{ss}^{\pm})$, and the interphase resistivity, $R_f^{\pm}$, which is an internal resistance that causes a voltage drop within the cell. For most new cells, $R_f^{\pm}$ is negligible. $\mathcal{U}^{\pm}(c_{ss}^{\pm})$, is an empirically defined value of the potential as a function of the surface concentration of the solid [18].

Additionally, the variation of the solid potential, $\phi_s^{\pm}(x,t)$, is defined as,

$$\frac{\partial \phi_s^{\pm}(x,t)}{\partial x} = \frac{i_e(x,t) - I(t)}{\sigma^{\pm}} \tag{3.20}$$

where $I(t)$ is the input current and $\sigma^{\pm}$ is the effective conductivity of the electrode. Similarly, the spatiotemporal dynamics of the electrolyte potential, $\phi_e^{\pm}(x,t)$, can be expressed as,

$$\frac{\partial \phi_e^{\pm}(x,t)}{\partial x} = -\frac{i_e(x,t)}{\kappa(x,t)} + \frac{2RT\,(1-t_c^0)}{F}\left(1+\frac{d\ln f_{c/a}(x,t)}{d\ln c_e(x,t)}\right)\left(\frac{\partial \ln c_e(x,t)}{\partial x}\right) \tag{3.21}$$

where R is the ideal gas constant, T is the temperature of the cell, and t_c^0 is the transference number of cations. Both the ionic conductivity, $\kappa(x,t)$, and the mean molar activity coefficient, $f_{c/a}$, are functions of electrolyte concentration.

Finally, the cell voltage, $V(t)$ can be calculated by finding the difference of the solid potentials at the current collectors, specifically,

$$V(t) = \phi_s^{+}(0^{+},t) - \phi_s^{-}(0^{-},t) \tag{3.22}$$

In summary, the isothermal DFN model is fully described by Equations (3.13) - (3.22). Other literature provides greater details on boundary conditions, thermal behavior, chemical dynamics and further explanation of the terms and physical nature of the variables [11] [15].

3.3.2 Model Order Reduction

Whether the model in question is the DFN, single particle model (SPM), or extended SPM (ESPM), the use of a PDE often introduces significant complexities for a number of system specific goals, such as estimation, prediction, or control. For this purpose, a reduced-order model, consisting of finite-dimensional rational transfer functions, is often useful. To this end, a number of model-order reduction (MOR) techniques have been reported in literature (see references in the survey paper, [16]). These methods are briefly presented below, with a focus on the derivation of an ODE, which results in a significant reduction in the simulation complexity.

Padé Approximation [31]

As the name suggests, this approach consists of deriving the underlying transfer function between the molar flux of lithium ions, often as a linear function of input current, and the solid electrode, starting from a diffusion PDE, which typically consists of time-delays, and subsequently applying Padé approximations. Denoting a typical MOR transfer function as,

$$\tilde{G}(s) = \frac{b_0 + b_1 s + b_2 s^2 + ... + b_q s^q}{s(a_0 + a_1 s + a_2 s^2 + ... + a_q s^q)} \tag{3.23}$$

the order q is determined so that the frequency response of $\tilde{G}(s)$ is matched to the total system dynamics, which manifest as a transcendental transfer function corresponding to the PDE in Equation (3.13), around specific operational frequencies, such that q is an arbitrarily low order linear system. After initial model order reduction, these techniques have a numerical complexity of $O(q^2)$.

Balanced Truncation [33]

In the case of balanced truncation, starting from Equation (3.13), a full order finite-difference model can be constructed for each electrode, and represented in standard state-space representation,

$$\begin{aligned} \dot{x} &= Ax + Bu \\ y &= Cx + Du \end{aligned} \tag{3.24}$$

for $x \in \mathbb{R}^{N \times 1}$. A nonsingular transformation, T, can be found, such that T is chosen to ensure the controllability and observability grammians are equal, leading to,

$$\begin{aligned} \dot{\tilde{x}} &= \tilde{A}\tilde{x} + \tilde{B}u \\ y &= \tilde{C}\tilde{x} + Du \end{aligned} \tag{3.25}$$

where $\tilde{x} = Tx$, such that $\tilde{A} = TAT^{-1}$, $\tilde{B} = TB$, and $\tilde{C} = CT^{-1}$. The diagonal of the resulting grammians from Equation (3.25) can be sorted in descending order of observable (or controllable) states to reduce the dimension of the system matrix to q, such that $q << N$. Again, the subsequent complexity for dynamical simulation is $O(q^2)$. It should be noted that with this model order reduction, the parameters, $\tilde{A}$, $\tilde{B}$

and $\tilde{C}$, no longer retain physical value, and additional matrix multiplications would need to be conducted to determine the original parameters, A, B and C, increasing the order to $O(q^2 + N^2)$.

Proper Orthogonal Decomposition [7]

To perform proper orthogonal decomposition, dominant singular values of simulation data are found to construct a reduced order model projected on the subspace, $\Phi_q \in \mathbb{R}^{q \times q}$, in the form,

$$\begin{aligned} \dot{\hat{x}} &= \Phi_q^\top A \Phi_q \hat{x} + \Phi_q^\top B u \\ y &= C \Phi_q \hat{x} \end{aligned} \tag{3.26}$$

for $\hat{x} \in \mathbb{R}^{q \times 1}$, where q is chosen as a tenable number of states for accuracy and numerical complexity, again resulting in $O(q^2)$ dynamical calculations. It should be noted that here, too, the reduced states, $\hat{x}$, and system matrix, $\hat{A} = \Phi_q^\top A \Phi_q$, have lost physical meaning through the order reduction, but replicate the results of the system well.

Orthogonal Collocation of Finite Elements [8]

Yet another model order reduction technique proposed in literature is through a finite element method, solved with orthogonal collocation at points optimally chosen within the solid to reduce the number of equations [8]. The locations of these points are defined by the Jacobi polynomial, P_N, shown in Equation (3.27), of an order equal to the number of desired collcation points, given by,

$$(1-x)^a x^b P_N^{(a,b)} = \frac{(-1)^N G(b+1)}{G(N+b+1)} \frac{d^N}{dx^N} \left((1-x)^{N+a} x^{N+b} \right) \tag{3.27}$$

where $G(s) = \frac{c_s(s)}{j(s)}$ is the transfer function of the solid concentration, and a and b represent a nonlinear distribution of points along the solid, $x \in \begin{bmatrix} 0, & 1 \end{bmatrix}$, such that a higher b will clump collocation points to the surface of the particle, while a higher

a will concentrate points at the center of the solid. In the worst case, this solution requires $O(N^2)$ calculations.

It is important to note that all of the above MOR techniques, listed in *a)* through *d)*, are applied to the solution of the PDE within the solid electrode, and do not focus on the electrolyte concentration, $c_e(x,t)$, or its ODE counterpart.

PDE Observer Approach

Significant effort in literature [36] [55] has been focused on incorporating the observer structure into the PDE formulation of the DFN model. One approach is to use the SPM PDE formulation, and in the observer reference model include additional boundary state error injection [36], such that,

$$\begin{aligned}\frac{\partial \hat{c}(r,t)}{\partial t} &= \epsilon \frac{\partial^2 \hat{c}(r,t)}{\partial^2 r} + p_1(r)\tilde{c}(1,t)\\ \hat{c}(0,t) &= 0 \\ \frac{\partial \hat{c}(1,t)}{\partial r} - \hat{c}(1,t) &= -q\rho I(t) + p_{10}(t)\tilde{c}(1,t)\end{aligned} \tag{3.28}$$

where $p_1(t)$ and p_{10} are the injection gains, and the observer error is defined as $\tilde{c}(r,t) = c(r,t) - \hat{c}(r,t)$. While producing consistent PDE observer results, as can be proven by subtracting the observer structure from the plant structure in a stability analysis [36], this approach is still limited by the dynamics of the SPM, which ignore the effects of the electrolyte. This is referred to as a back-stepping observer, and has been shown to yield successful results with respect to state estimation in the solid electrode [36] [55]. In the approach proposed in this paper, based on the ANCF [50], variations in the solid electrode and electrolyte are addressed by the method outlined below.

3.3.3 Single Particle Model

In the interest of simplifying the defining equations of the DFN model, expressed in Equations (3.13) - (3.22), further assumptions have been proposed [41] [48] [47], arriving at what is known as the Single Particle Model (SPM).

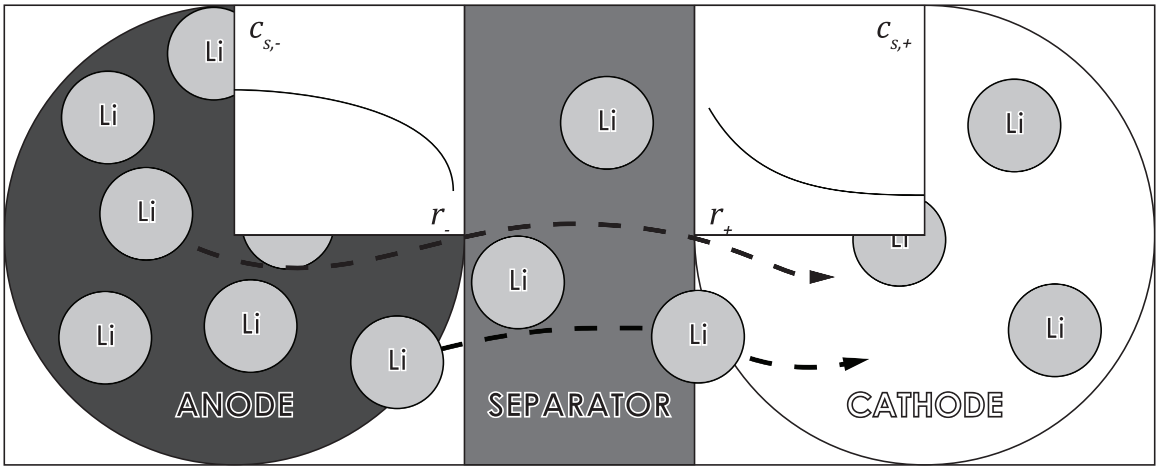

Figure 3-4: Coarse discretization scheme of the single particle model.

In the formulation of the SPM, the solid electrodes are discretized at the lowest resolution possible, specifically one pseudo-sphere per electrode. Furthermore, in the simplest form of the SPM, any variation in the electrolyte concentration is ignored, as seen in Figure 3-4, which disregards the dynamics of Equation (3.15) as well as Equation (3.21). This manifests as,

$$\begin{aligned} \frac{\partial c_e(x,t)}{\partial t} &= 0 \\ \frac{\partial c_e(x,t)}{\partial x} &= 0 \end{aligned} \tag{3.29}$$

which allows for an analytical solution to the model. However, an electrolyte concentration is still defined, such that $c_e(x,t) = c_{e,0}$. It can be shown that Equation (3.16) can be solved with boundary conditions to produce a definition of the molar flux as,

$$j^{\pm}(t) = \mp \frac{I(t)}{F a^{\pm} L^{\pm}} \tag{3.30}$$

Using this definition, and applying it to the Butler-Volmer Kinetics described in Equation (3.17), one can calculate an explicit definition of the solid potential at the current collectors,

$$\begin{aligned}\phi_s^{\pm}(t) =& \frac{2RT}{F}\sinh^{-1}\left(\frac{I(t)}{2a^{\pm}L^{\pm}k_{eff}\sqrt{c_{e,0}c_{ss}^{\pm}(t)\left(c_{s,max}^{\pm}-c_{ss}^{\pm}(t)\right)}}\right)\\ &+\mathcal{U}^{\pm}(c_{ss}^{\pm}(t))+\frac{R_f^{\pm}}{a^{\pm}L^{\pm}}I(t)\end{aligned} \tag{3.31}$$

Finally, the voltage can be defined as,

$$V(t) = \phi_s^{+}(t) - \phi_s^{-}(t) \tag{3.32}$$

where the two solid potentials are taken as the voltages at the current collectors. The definition of the solid dynamics remains mostly unchanged, except for the removal of the x term in favor of a volume distinction, namely $\pm$, as a convention previously introduced. This is shown in Equation (3.33).

$$\frac{\partial c_s^{\pm}(r,t)}{\partial t} = \frac{1}{r^2}\frac{\partial}{\partial r}\left(D_s^{\pm}r^2\frac{\partial c_s^{\pm}(r,t)}{\partial r}\right) \tag{3.33}$$

In this equation it is clear that some type of linearization for purposes of turning the PDE into an ODE, or an explicit PDE solution, is needed. This is the focus of many of the model order reduction techniques discussed in Section 3.3. The structure of the boundary conditions of this equation remain, but are adjusted using the explicit definition of the molar flux, $j^{\pm}(t)$, shown in Equation (3.30).

$$\begin{aligned}\left.\frac{\partial c_s^{\pm}(r,t)}{\partial r}\right|_{r=0} &= 0\\ \left.\frac{\partial c_s^{\pm}(r,t)}{\partial r}\right|_{r=R_p^{\pm}} &= \pm\frac{I(t)}{D_s^{\pm}Fa^{\pm}L^{\pm}}\end{aligned} \tag{3.34}$$

The initial condition is defined as,

$$c_s^{\pm}(r,0) = c_{s,0}^{\pm}(r) \tag{3.35}$$

while the definition of surface concentration remains unchanged,

$$c_{ss}^{\pm}(t) = c_s^{\pm}\left(R_p^{\pm}, t\right) \tag{3.36}$$

These equations define the simplified structure of the SPM, based on the assumptions of negligible concentration variation in the electrolyte.

Even though these assumptions help in reducing the computational burden of the model, they result in a degraded fidelity at higher currents. Despite the latter, it has been shown that the SPM is highly useful in developing control schemes [11] [35] [52] [12] and estimation methods [23]. With the intent of better replicating the effects of high discharge cycles, the SPM has more recently been extended to include electrolyte variation [44] [19] (ESPM). This implies that Equations (3.15) and (3.21) can no longer be neglected, which contributes additional complexity, but more fidelity at higher currents.

3.4 ANCF Model

In this section, a reduced-order model of the Li-ion cell is derived using the absolute nodal coordinate formulation (ANCF). Originally designed to replicate the nonlinear effects of highly flexible beams [50] [61], the same principles allow the proposed model to capture the significant variation of the electrolyte concentration, $c_e(x,t)$; molar flux, $j(x,t)$; and volume projections of solid electrode concentrations, $\bar{c}_s(x,t)$ and $q(x,t)$. The approach using the latter three states is based on a third order polynomial description of the spatial variations of the solid concentration, which allows for the reduction of the problem from a PDE to that of an ODE of the volume averaged projection of the concentration [54].

3.4.1 Basis Functions

In order to introduce the underlying spatial approximation, the model construction begins using a pseudostate variable, $\theta(x,t)$, which can be conceptualized as a surrogate variable for various electrochemical states, including electrolyte concentration, $c_e(x,t)$, molar flux, $j(x,t)$, average solid concentration within the pseudo-sphere, $\bar{c}_s(x,t)$, and a surface concentration difference, $q(x,t)$. The solid electrodes and separator are discretized into N nodes, which, in turn, define $N-1$ elements along the dominant spatial dimension, x. An element length is defined as,

$$l' = \frac{L}{N-1} \tag{3.37}$$

where L is the full compartment length of the anode, cathode as well as the separator. For each element, i, a local coordinate, $s_i(x,i)$, can be defined such that,

$$s_i(x,i) = \frac{x-(i-1)l'}{l'} \tag{3.38}$$

for every element, $i \in \begin{bmatrix} 1 & \cdots & N\text{ - }1 \end{bmatrix}$, in a volume. An indexing function is also defined,

$$\chi_i(x) = \begin{cases} 1 & \text{if } x \in \begin{bmatrix} il\text{'}, & (i{+}1)l\text{'} \end{bmatrix}, \\ 0 & \text{else.} \end{cases} \tag{3.39}$$

A basis function in the form of a cubic polynomial is chosen, as its four associated degrees are sufficient to characterize the spatial variations of the problem under consideration. This polynomial is chosen to be a function of the absolute nodal dimension, s_i, and is given by,

$$\theta_i(s_i,t) = \alpha_i(t) + \beta_i(t)s_i + \gamma_i(t)s_i^2 + \delta_i(t)s_i^3 \tag{3.40}$$

The pseudostate variable, $\theta(x,t)$, is then approximated over a compartment using the polynomial in Equation (3.40) and the indexing function in Equation (3.39) as,

$$\theta(x,t) \approx \sum_{i=1}^{N-1} \chi_i(x)\theta_i(s_i,t) \tag{3.41}$$

To determine the time-varying coefficients in Equation (3.40), four generalized boundary conditions,

$$\begin{aligned} \theta_i(0,t) &= \psi_i(t) \\ \left.\frac{\partial \theta_i(s_i,t)}{\partial s_i}\right|_{s_i=0} &= l' \frac{\partial \psi_i(t)}{\partial x} \\ \theta_i(1,t) &= \psi_{i+1}(t) \\ \left.\frac{\partial \theta_i(s_i,t)}{\partial s_i}\right|_{s_i=1} &= l' \frac{\partial \psi_{i+1}(t)}{\partial x} \end{aligned} \tag{3.42}$$

are used, where the quantity $\psi_i(t)$ represents the time-dependent value of $\theta(s_i,t)$ at the i^{th} node. Using the boundary conditions of Equation (3.96) to solve for Equation (3.40), the basis function is then determind as,

$$\begin{aligned} \theta_i(s_i,t) =& \psi_i(t)(1-3s_i^2+2s_i^3) + l' \frac{\partial \psi_i(t)}{\partial x}(s_i - 2s_i^2 + s_i^3) \\ &+ \psi_{i+1}(t)(3s_i^2 - 2s_i^3) + l' \frac{\partial \psi_{i+1}(t)}{\partial x}(-s_i^2 + s_i^3) \end{aligned} \tag{3.43}$$

Equation (3.43) is rewritten using a vector notation,

$$\theta_i(s_i,t) = \boldsymbol{s}_i^\top \boldsymbol{\theta}_i(t) \tag{3.44}$$

where the state vector is defined by,

$$\boldsymbol{\theta}_i(t) = \begin{bmatrix} \psi_i(t) & l' \frac{\partial \psi_i(t)}{\partial x} & \psi_{i+1}(t) & l' \frac{\partial \psi_{i+1}(t)}{\partial x} \end{bmatrix}^\top \tag{3.45}$$

and the coordinate weight vector,

$$\boldsymbol{s}_i = \begin{bmatrix} 1 - 3s_i^2 + 2s_i^3 \\ s_i - 2s_i^2 + s_i^3 \\ 3s_i^2 - 2s_i^3 \\ -s_i^2 + s_i^3 \end{bmatrix} \tag{3.46}$$

which defines the shape vector. The expression in (3.46) is rewritten as,

$$\boldsymbol{s}_i = \left[\begin{array}{cccc} \mathrm{s}_1^i & \mathrm{s}_2^i & \mathrm{s}_3^i & \mathrm{s}_4^i \end{array} \right]^\top \tag{3.47}$$

This implies that if a pseudostate pair is defined,

$$\boldsymbol{\psi}^i(t) = \left[\begin{array}{cc} \psi_i(t) & l' \frac{\partial \psi_i(t)}{\partial x} \end{array} \right]^\top \tag{3.48}$$

the element notation of Equation (3.44), can be rewritten as,

$$\theta_i(s_i, t) = \left[\begin{array}{cc} \mathrm{s}_1^i & \mathrm{s}_2^i \end{array} \right] \boldsymbol{\psi}^i(t) + \left[\begin{array}{cc} \mathrm{s}_3^i & \mathrm{s}_4^i \end{array} \right] \boldsymbol{\psi}^{i+1}(t) \tag{3.49}$$

The use of these pseudostate pairs in the reconstruction of the actual spatiotemporal variable $\theta(x, t)$ is illustrated in Figure 3-5.

With the pseudostate pair in Equation (3.48), a complete state vector can be written, with respect to the variable $\theta(x, t)$ as,

$$\boldsymbol{\theta}(t) = \left[\begin{array}{cccccc} \boldsymbol{\psi}^1(t) & \boldsymbol{\psi}^2(t) & \boldsymbol{\psi}^3(t) & \cdots & \boldsymbol{\psi}^{N-1}(t) & \boldsymbol{\psi}^N(t) \end{array} \right]^\top \tag{3.50}$$

This, in turn, allows the underlying approximation in Equation (3.41) to be rewritten as,

$$\theta(x, t) \approx \left[\begin{array}{c} \mathrm{s}_1^1 \\ \mathrm{s}_2^1 \\ (\mathrm{s}_3^1 + \mathrm{s}_1^2) \\ (\mathrm{s}_4^1 + \mathrm{s}_2^2) \\ \vdots \\ (\mathrm{s}_3^{N-1} + \mathrm{s}_1^N) \\ (\mathrm{s}_4^{N-1} + \mathrm{s}_2^N) \\ \mathrm{s}_3^N \\ \mathrm{s}_4^N \end{array} \right]^\top \boldsymbol{\theta}(t) \tag{3.51}$$

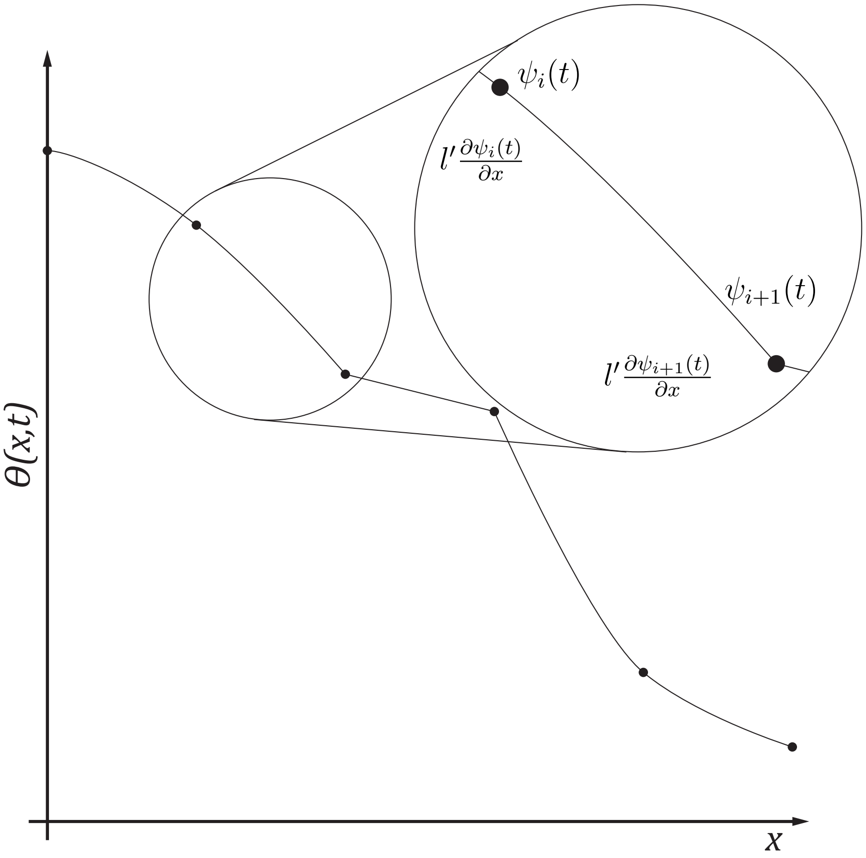

Figure 3-5: Nodal identities of the ANCF model, allowing for high order dynamics to be captured with two states per node.

By applying the profile approximation in Equation (3.51) to the electrolyte concentration, the average solid concentration, surface concentration differential, and the molar flux, an approximation can be obtained for $c_e(x,t)$ in Equation (3.15), $\bar{c}_s(x,t)$ in Equation (3.13), $q(x,t)$ in Equation (3.60), and $j(x,t)$ in Equation (3.56), as $\boldsymbol{c}_e(t)$, $\bar{\boldsymbol{c}}_s(t)$, $\boldsymbol{q}(t)$, and $\boldsymbol{j}(t)$, respectively.

3.4.2 Solid Dynamics

In order to apply the ANCF approximation in Equation (3.51) to the transport in the solid electrode, an approximation is introduced with respect to variation in the r-direction [54], shown to be valid for low to medium input currents [8] [54]. This approximation is briefly summarized below. The profile of the concentrate is assumed to permit an expansion,

$$c_s^{\pm}(x,r,t) = \alpha(x,t) + \beta(x,t)\left(\frac{r}{R_p^{\pm}}\right)^2 + \gamma(x,t)\left(\frac{r}{R_p^{\pm}}\right)^4 \tag{3.52}$$

where $\alpha(x,t)$, $\beta(x,t)$ and $\gamma(x,t)$, are unknown variables in x and t. By defining two new variables,

$$\bar{c}_s(x,t) = \int_{r=0}^{R_p^{\pm}} 3\left(\frac{r}{R_p^{\pm}}\right)^2 c_s^{\pm}(x,r,t)\,d\left(\frac{r}{R_p^{\pm}}\right) \tag{3.53}$$

and

$$q(x,t) = \int_{r=0}^{R_p^{\pm}} 3\left(\frac{r}{R_p^{\pm}}\right)^2 \left(\frac{\partial}{\partial r} c_s^{\pm}(x,r,t)\right) d\left(\frac{r}{R_p^{\pm}}\right) \tag{3.54}$$

one can solve for the unknown parameters, $\alpha(x,t)$, $\beta(x,t)$ and $\gamma(x,t)$, using Equations (3.52) and (3.13). Using appropriate boundary conditions, these terms can be defined in terms of $\bar{c}_s(x,t)$, $q(x,t)$ and the surface concentration, $c_{ss}(x,t) = c_s^{\pm}(x, R_p^{\pm}, t)$, such that,

$$\begin{aligned}
\alpha(x,t) &= \frac{39}{4}c_{ss}(x,t) - 3R_p^{\pm}q(x,t) - \frac{35}{4}\bar{c}_s(x,t) \\
\beta(x,t) &= -35c_{ss}(x,t) + 10R_p^{\pm}q(x,t) + 35\bar{c}_s(x,t) \\
\gamma(x,t) &= \frac{105}{4}c_{ss}(x,t) - 7R_p^{\pm}q(x,t) - \frac{105}{4}\bar{c}_s(x,t)
\end{aligned} \tag{3.55}$$

After including these terms in Equation (3.52), three equations are required to solve for $\bar{c}_s(x,t)$, $q(x,t)$ and $c_{ss}(x,t)$. The first equation is found by solving Equation (3.13) substituted with Equation (3.52), and solved at the boundary $r = R_p^{\pm}$, results in the expression,

$$c_{ss}(x,t) = \bar{c}_s(x,t) + \frac{8R_p^{\pm}}{35}q(x,t) - \frac{R_p^{\pm}}{35D_s^{\pm}}j(x,t) \tag{3.56}$$

The second equation uses the left hand side of Equation (3.13) to define a bulk residue of the solid dynamics, such that,

$$\int_{r=0}^{R_p^{\pm}} 3\left(\frac{r}{R_p^{\pm}}\right)^2 \left[\frac{\partial c_s^{\pm}}{\partial t} - \frac{1}{r^2}\frac{\partial}{\partial r}\left(D_s^{\pm} r^2 \frac{\partial c_s^{\pm}}{\partial r}\right)\right] d\left(\frac{r}{R_p^{\pm}}\right) = 0 \tag{3.57}$$

Reducing this expression results in the following equation,

$$\frac{\partial \bar{c}_s(x,t)}{\partial t} = -\frac{3}{R_p^{\pm}} j(x,t) \tag{3.58}$$

where the dynamics of the average solid concentration, $\bar{c}_s(x,t)$, is a function of the molar flux, $j(x,t)$. The final equation in Equation (3.55) is simplified as,

$$\int_{r=0}^{R_p^{\pm}} 3\left(\frac{r}{R_p^{\pm}}\right)^2 \frac{\partial}{\partial r}\left[\frac{\partial c_s^{\pm}}{\partial t} - \frac{1}{r^2}\frac{\partial}{\partial r}\left(D_s^{\pm} r^2 \frac{\partial c_s^{\pm}}{\partial r}\right)\right] d\left(\frac{r}{R_p^{\pm}}\right) = 0 \tag{3.59}$$

Reduction of this expression yields,

$$\frac{\partial q(x,t)}{\partial t} = -\frac{30 D_s^{\pm}}{\left(R_p^{\pm}\right)^2} q(x,t) - \frac{45}{2\left(R_p^{\pm}\right)^2} j(x,t) \tag{3.60}$$

where the time variation of $q(x,t)$ is an ODE forced by $j(x,t)$.

With the above, rather than Equation (3.13), simplified electrode transport dynamics are obtained, given by Equations (3.56), (3.58), and (3.60). Using the corresponding profile approximation in Equation (3.51) for $\bar{c}_s(x,t)$ in (3.58) and $q(x,t)$ in (3.60), one can derive the corresponding ordinary differential equations for $\bar{\boldsymbol{c}}_s(t) \in \mathbb{R}^{2N}$ and $\boldsymbol{q}(t) \in \mathbb{R}^{2N}$ as,

$$\frac{d\bar{\boldsymbol{c}}_s(t)}{dt} = -\frac{3}{R_p^{\pm}} \boldsymbol{j}(t) \tag{3.61}$$

$$\frac{d\boldsymbol{q}(t)}{dt} = -\frac{30 D_s^{\pm}}{\left(R_p^{\pm}\right)^2} \boldsymbol{q}(t) - \frac{45}{2\left(R_p^{\pm}\right)^2} \boldsymbol{j}(t) \tag{3.62}$$

where $\boldsymbol{j}(t)$ is the corresponding approximation to the molar flux, $j(x,t)$.

3.4.3 Electrolyte Dynamics

In order to derive the ODE for $c_e(x,t)$, the elemental profile approximation in Equation (3.41) is used, rather than the nodal representation in Equation (3.51). Denoting the left hand side of Equation (3.15) in terms of $c_{e,i}(s_i,t)$ as $R(s_i,t)$, the vector notation of Equation (3.44) is used to derive the relation,

$$R(s_i,t) = \boldsymbol{s}_i^\top \frac{d\boldsymbol{c}_{e,i}(t)}{dt} - \frac{D_i(t)}{(l')^2}\frac{d^2\boldsymbol{s}_i^\top}{ds_i^2}\boldsymbol{c}_{e,i}(t) - \frac{t_a^0 a}{\epsilon_e}\boldsymbol{s}_i^\top \boldsymbol{j}_i(t) \tag{3.63}$$

The term $R(s_i,t)$ denotes an approximation error and is referred to as a residue function [53]. In an effort to reduce this approximation error to zero, an additional constraint is imposed,

$$\int_0^1 \boldsymbol{s}_i R(s_i,t) ds_i = 0 \tag{3.64}$$

commonly utilized in a Galerkin approach [53]. Equation (3.64) can be expanded as,

$$\begin{aligned} 0 &= \int_0^1 \boldsymbol{s}_i\boldsymbol{s}_i^\top ds_i \frac{d\boldsymbol{c}_{e,i}(t)}{dt} - \frac{D_i(t)}{(l')^2}\int_0^1 \boldsymbol{s}_i \frac{d^2\boldsymbol{s}_i^\top}{ds_i^2} ds_i \boldsymbol{c}_{e,i}(t) - \frac{t_a^0 a}{\epsilon_e}\int_0^1 \boldsymbol{s}_i\boldsymbol{s}_i^\top ds_i \boldsymbol{j}_i(t) \\ &= \mathrm{M}\frac{d\boldsymbol{c}_{e,i}(t)}{dt} - \frac{D_i(t)}{(l')^2}\mathrm{K}\boldsymbol{c}_{e,i}(t) - \frac{t_a^0 a}{\epsilon_e}\mathrm{M}\boldsymbol{j}_i(t) \end{aligned} \tag{3.65}$$

where the first integration matrix, M is defined by,

$$\mathrm{M} = \int_0^1 \boldsymbol{s}_i\boldsymbol{s}_i^\top ds_i \tag{3.66}$$

and the second integration matrix, K, by,

$$\mathrm{K} = \int_0^1 \boldsymbol{s}_i \frac{d^2\boldsymbol{s}_i^\top}{ds_i^2} ds_i \tag{3.67}$$

The effective diffusion coefficent, $D_i(t)$, constant across an element, is defined by,

$$D_i = \bar{D}_{e,i}(t)\epsilon_e^b \tag{3.68}$$

where ϵ_e is the electrolyte volume fraction, b is the Bruggeman coefficient, and the element-averaged electrolyte diffusion coefficient, $\bar{D}_e$ is evaluated,

$$\bar{D}_{e,i}(t) = 2.582 \times 10^{-9} e^{\left(-2.856\times10^{-3}\bar{\boldsymbol{c}}_{e,i}(t)\right)} \tag{3.69}$$

and $\bar{\boldsymbol{c}}_{e,i}(t)$ denotes the average electrolyte concentration for an element, given by,

$$\bar{\boldsymbol{c}}_{e,i}(t) = \int_0^1 \boldsymbol{s}_i^\top \boldsymbol{c}_{e,i}(t) ds_i \tag{3.70}$$

The complete set of equations that define the electrolyte dynamics will now be constructed. Equation (3.66) is rewritten as,

$$\mathrm{M}^i = \int_0^1 \begin{bmatrix} \mathrm{M}_{11}^i & \mathrm{M}_{12}^i \\ \mathrm{M}_{21}^i & \mathrm{M}_{22}^i \end{bmatrix} ds_i \tag{3.71}$$

where the submatrices of M^i are defined as,

$$\mathrm{M}_{jk}^i = \int_0^1 \begin{bmatrix} \mathrm{s}_{2j-1}^i \mathrm{s}_{2k-1}^i & \mathrm{s}_{2j-1}^i \mathrm{s}_{2k}^i \\ \mathrm{s}_{2j}^i \mathrm{s}_{2k-1}^i & \mathrm{s}_{2j}^i \mathrm{s}_{2k}^i \end{bmatrix} ds_i, \tag{3.72}$$

for $j, k = 1, 2$, and s_j^i denotes the jth element of the vector $\boldsymbol{s}_i$, as shown in Equation (3.47). Similarly, Equation (3.67) can be written as,

$$\mathrm{K}^i = \int_0^1 \begin{bmatrix} \mathrm{K}_{11}^i & \mathrm{K}_{12}^i \\ \mathrm{K}_{21}^i & \mathrm{K}_{22}^i \end{bmatrix} ds_i \tag{3.73}$$

where the submatrices of K^i, are defined as,

$$\mathrm{K}_{jk}^i = \int_0^1 \begin{bmatrix} \mathrm{s}_{2j-1}^i \frac{d^2\mathrm{s}_{2k-1}^i}{ds_i^2} & \mathrm{s}_{2j-1}^i \frac{d^2\mathrm{s}_{2k}^i}{ds_i^2} \\ \mathrm{s}_{2j}^i \frac{d^2\mathrm{s}_{2k-1}^i}{ds_i^2} & \mathrm{s}_{2j}^i \frac{d^2\mathrm{s}_{2k}^i}{ds_i^2} \end{bmatrix} ds_i, \tag{3.74}$$

for $j, k = 1, 2$. Using Equations (3.65), (3.71) and (3.73), a set of ODEs that describes the electrolyte dynamics can be written as,

$$\begin{aligned} 0 = &\left(\mathrm{M}_{21}^{i-1} \frac{d\boldsymbol{c}_e^{i-1}}{dt} + \left(\mathrm{M}_{11}^{i} + \mathrm{M}_{22}^{i}\right) \frac{d\boldsymbol{c}_e^{i}}{dt} + \mathrm{M}_{12}^{i+1} \frac{d\boldsymbol{c}_e^{i+1}}{dt} \right) \\ &- \frac{1}{(l')^2} \left(D_{i-1}\mathrm{K}_{21}^{i-1}\boldsymbol{c}_e^{i-1} + \left(D_i\mathrm{K}_{11}^{i} + D_{i-1}\mathrm{K}_{22}^{i}\right)\boldsymbol{c}_e^{i} + D_i\mathrm{K}_{12}^{i+1}\boldsymbol{c}_e^{i+1} \right) \\ &+ \left(\frac{t_a^0 a}{\epsilon_e}\right) \left(\mathrm{M}_{21}^{i-1}\boldsymbol{j}^{i-1} + \left(\mathrm{M}_{11}^{i} + \mathrm{M}_{22}^{i}\right)\boldsymbol{j}^{i} + \mathrm{M}_{12}^{i+1}\boldsymbol{j}^{i+1} \right) \end{aligned} \tag{3.75}$$

where $\boldsymbol{c}_e^i$ and $\boldsymbol{j}^i$ denote the state pair corresponding to $\boldsymbol{c}_e(t)$ and $\boldsymbol{j}(t)$, respectively, defined as in Equation (3.48). The equation for the electrolyte dynamics, Equation (3.65), can be combined in vector form as,

$$0 = \mathbf{M}\frac{d\boldsymbol{c}_e(t)}{dt} - \frac{1}{(l')^2}\mathbf{K}\boldsymbol{c}_e(t) - \frac{t_a^0 a}{\epsilon_e}\mathbf{M}\boldsymbol{j}(t) \tag{3.76}$$

where the full system integration matrix, $\mathbf{M} \in \mathbb{R}^{2N\times 2N}$, is defined by,

$$\mathbf{M} = \begin{bmatrix} \mathrm{M}_{11}^1 & \mathrm{M}_{12}^1 & 0 & 0 \\ \mathrm{M}_{21}^1 & \mathrm{M}_{22}^1 + \mathrm{M}_{11}^2 & \mathrm{M}_{12}^2 & 0 \\ 0 & \mathrm{M}_{21}^2 & \ddots & \mathrm{M}_{12}^N \\ 0 & 0 & \mathrm{M}_{21}^{N-1} & \mathrm{M}_{22}^N \end{bmatrix} \tag{3.77}$$

while the matrix, $\mathbf{K} \in \mathbb{R}^{2N\times 2N}$, is defined by,

$$\mathbf{K} = \begin{bmatrix} D_1\mathrm{K}_{11}^1 & D_1\mathrm{K}_{12}^1 & 0 & 0 \\ D_1\mathrm{K}_{21}^1 & (D_1\mathrm{K}_{22}^1 + D_2\mathrm{K}_{11}^2) & D_2\mathrm{K}_{12}^2 & 0 \\ 0 & D_2\mathrm{K}_{21}^2 & \ddots & D_N\mathrm{K}_{12}^N \\ 0 & 0 & D_{N-1}\mathrm{K}_{21}^{N-1} & D_N\mathrm{K}_{22}^N \end{bmatrix} \tag{3.78}$$

In summary, Equation (3.65), which describes the ODE counterpart of the electrolyte dynamics, can be rewritten as,

$$\frac{d\boldsymbol{c}_e(t)}{dt} = \frac{1}{(l')^2}\mathbf{M}^{-1}\mathbf{K}\boldsymbol{c}_e(t) + \frac{t_a^0 a}{\epsilon_e}\boldsymbol{j}(t) \tag{3.79}$$

3.4.4 Butler-Volmer Kinetics

The final component of the ANCF model is the differential algebraic constraint imposed by the Butler-Volmer kinetics. For this purpose, Equation (3.20) is differentiated with respect to x, and Equation (3.16) is substituted to yield,

$$\frac{\partial^2 \phi_s^{\pm}(x,t)}{\partial x^2} = \frac{a^{\pm}F}{\sigma^{\pm}} j(x,t) \tag{3.80}$$

Integrating Equation (3.80) twice, while substituting in the ANCF expansions from Equation (3.44) corresponding to $\phi_s^{\pm}(x,t)$, produces,

$$\phi_{s,i}(s_i,t) = \frac{a^{\pm}F}{\sigma^{\pm}}(l')^2 \iint \boldsymbol{s}_i^{\top}\boldsymbol{j}_i(t)ds_i ds_i + l'\frac{\partial \phi_{s,i}}{\partial x}s_i + \phi_{s,i}. \tag{3.81}$$

Similarly, using Equation (3.21), an ANCF formulation of the electrolytic potential is derived as,

$$\begin{aligned}\phi_{e,i}(s_i,t) = &-\frac{I(t)}{\kappa_{eff}}s_i - \frac{\sigma^{\pm}}{\kappa_{eff}}\left(\phi_{s,i}(s_i,t) - \phi_{s,i}\right) \\ &+ \frac{2RT\left(1-t_c^0\right)}{F}\left(\ln\left(c_{e,i}(s_i,t)\right) - \ln\left(c_{e,i}\right)\right) + \boldsymbol{\phi}_{e,i}\end{aligned} \tag{3.82}$$

Subsequently, an ANCF formulation of the overpotential, derived from Equation (3.19), can be defined such that,

$$\eta_i(s_i,t) = \phi_{s,i}(s_i,t) - \phi_{e,i}(s_i,t) - \mathcal{U}_i(c_{ss,i}(s_i,t)) \tag{3.83}$$

which ignores ohmic losses, thereby allowing the last term in Equation (3.19) to be set to zero. The Butler-Volmer kinetics, Equation (3.17), can then be fully described in the absolute nodal coordinates, using $j_i(s_i,t)$ as an algebraic constraint,

$$j_i(s_i,t) = i_0(c_{e,i}(s_i,t), c_{ss,i}(s_i,t)) \left[\exp\left(\frac{\alpha_c F}{RT}\eta_i(s_i,t)\right) - \exp\left(\frac{\alpha_a F}{RT}\eta_i(s_i,t)\right)\right] \quad (3.84)$$

where the exchange current density, i_0, is defined by,

$$i_0(c_{e,i}(s_i,t), c_{ss,i}(s_i,t)) = k^{\pm} c_{e,i}(s_i,t)^{\alpha_a}\left(c^{\pm}_{s,max} - c_{ss,i}(s_i,t)\right)^{\alpha_a} c_{ss,i}(s_i,t)^{\alpha_c} \quad (3.85)$$

To solve this equation, a residue, $\boldsymbol{R}_i(s_i,t)$, is defined as,

$$\begin{aligned}\boldsymbol{R}_i(s_i,t) =& i_0(c_{e,i}(s_i,t), c_{ss,i}(s_i,t)) \left[\exp\left(\frac{\alpha_c F}{RT}\eta_i(s_i,t)\right) - \exp\left(\frac{\alpha_a F}{RT}\eta_i(s_i,t)\right)\right] \\ & - j_i(s_i,t)\end{aligned} \quad (3.86)$$

The goal is to choose j_i so that this residue is minimized, which can be accomplished using the orthogonal collocation method [8]. For this purpose, checking points, d_j, are chosen in the interval $s_i \in [0,1]$ as roots of the Gauss-Legendre polynomial [1]. The molar flux, j_i, is then chosen so that the expression,

$$0 = \int_0^1 \delta_i(s_i - d_j)\boldsymbol{R}_i(s_i,t)ds_i, \qquad j = 1,\ldots,4 \quad (3.87)$$

through a nonlinear solver [32]. Such a determination of the flux requires k iterations to bring the residue $R_i(d_j,t)$ down to an appropriately small value. As shown in Section 3.4.6, the use of a damped least squares algorithm can be employed for these iterations, with the corresponding k chosen so as to reduce the norm of $R_i(d_j,t)$ to less than 10^{-6}.

3.4.5 Overall ANCF Model

The complete ANCF model is determined by the ordinary differential equations in Equations (3.61), (3.62) and (3.79), with the molar flux approximation $\boldsymbol{j}(t)$ determined so that the residue, $\boldsymbol{R}_i$ in Equation (3.86) is minimized. As the latter involves numerical iterations at each time step, numerical integration of the underlying ODE is somewhat complex.

The overall ANCF algorithm is summarized below, in Algorithm 1, which includes numerical integration of ODEs, as well as the numerical iterations associated with algebraic constraint. Algorithm 1 proceeds with an initialization of $\bar{\boldsymbol{c}}_s(t) \in \mathbb{R}^{2N}$ from Equation (3.61), $\boldsymbol{c}_e(t) \in \mathbb{R}^{2N-1}$ from Equation (3.79), and $\boldsymbol{q}(t) \in \mathbb{R}^{2N}$ from Equation (3.62), at $t = 0$, with an arbitrary initialization as $\boldsymbol{j}(t) = \boldsymbol{0}$. For $\boldsymbol{s}_i \in [0, 1]$, d_j is calculated as the roots of the Gauss-Legendre polynomial [1]. With these values, $\bar{\boldsymbol{c}}_{s,0}$, $\boldsymbol{c}_{e,0}$, $\boldsymbol{q}_0$ and $\boldsymbol{j}_0$, $c_{ss}(s_i, 0)$ is determined using Equation (3.56), and therefore

Algorithm 1: ANCF Li-ion Cell Model

```
function ANCF($\bar{\boldsymbol{c}}_{s,0}, \boldsymbol{q}_0, \boldsymbol{c}_{e,0}, \epsilon_R, T_f, I$)
$\bar{\boldsymbol{c}}_s \leftarrow \bar{\boldsymbol{c}}_{s,0}$
$l \leftarrow 1$
$\boldsymbol{q}^l \leftarrow \boldsymbol{q}_0$
$\boldsymbol{c}_e^l \leftarrow \boldsymbol{c}_{e,0}$
$\boldsymbol{j}^l \leftarrow \boldsymbol{0}$
calculate $d_j$
do
    $k \leftarrow 0$
    do
        for $i \in [1, N]$ do
            compute $\phi_{e,i}(I)$, $\phi_{s,i}$, $\mathcal{U}_i$
            compute $\eta_i$
            for $j \in [1, 4]$ do
                compute $\boldsymbol{R}_i^k(d_j)$
                // nonlinear solve
                solve $\frac{\partial \boldsymbol{R}_i^k}{\partial j^{l,k}} \Delta j_i^{l,k}(d_j) = -\boldsymbol{R}_i^k(d_j)$
            end
        end
        $\boldsymbol{j}^{l,k+1} \leftarrow \boldsymbol{j}^{l,k} + \Delta \boldsymbol{j}^{l,k}$
        $k \leftarrow k + 1$
    while $\left\|\boldsymbol{R}^k\right\| > \epsilon_R$
    $\boldsymbol{j}^l \leftarrow \boldsymbol{j}^{l,k}$
    $\bar{\boldsymbol{c}}_s^{l+1} \leftarrow \bar{\boldsymbol{c}}_s^l + \Delta t f(\bar{\boldsymbol{c}}_s^l, \boldsymbol{j}^l)$
    $\boldsymbol{q}^{l+1} \leftarrow \boldsymbol{q}^l + \Delta t f(\boldsymbol{q}_s^l, \boldsymbol{j}^l)$
    $\boldsymbol{c}_e^{l+1} \leftarrow \boldsymbol{c}_e^l + \Delta t f(\boldsymbol{c}_e^l, \boldsymbol{j}^l)$
    $l \leftarrow l + 1$
while $t_l \leq T_f$
```

$\mathcal{U}(c_{ss}(s_i, 0))$ from Equation (3.83). Using Equations (3.81) to (3.83), the residue $\boldsymbol{R}_i(s_i, t)$ is determined and minimized using a nonlinear solver. The corresponding argument that minimizes $\boldsymbol{R}_i$ determines $\boldsymbol{j}(t)$ over the element s_i, and this process is repeated for all s_i. Using $\boldsymbol{j}(\tau)$, Equations (3.61), (3.62), and (3.79) are integrated to determine $\overline{\boldsymbol{c}}_s$, $\boldsymbol{q}$, $\boldsymbol{c}_e$ at $t = \tau$. This process is repeated at each timestep, for all s_i, $i = 1, \ldots, N$, leading to the overall ANCF-based solution. Table 3.1 shows the parameters used in the simulations described in Section 3.6 for all models.

3.4.6 Computational Complexity

The ANCF model presented above is an ODE of order $N_c = 6N - 2$, given by Equations (3.61), (3.62) and (3.79), with $N_j = 2N-2$ nonlinear algebraic constraints, given in Equation (3.87), with the reduction by two due to boundary conditions. As will be validated in the following section, the value of the ANCF lies in its concurrent realization of reduced computational complexity through model order reduction and fidelity to the truth model, while maintaining a tangible relationship to physical parameters. As noted above, at each timestep, k iterations are needed to determine j, and therefore the entire computational complexity of the ANCF is $O(N_c^2 + 4kN_j^2)$. Defining $N_T = N_c + N_j$, it can be seen that for $N = 6$, $N_c = 34$ and $N_j = 10$, such that $N_T = 44$.

In comparison with the computational complexity of the ANCF, it should be noted that the complexity of other MOR methods described in Section 3.3.2 is of the order $O(q^2)$. In addition, these methods can achieve a desired accuracy with $q = 3$ states in comparison with $N_T = 44$ with the ANCF. It should be noted, however, that connection to the underlying physics and electrochemistry in these models is nonexistent, with a slight exception in the case of Padé approximation. In the latter, the moments can be matched around $s = x$, where x is any physical parameter [16], but the transition from the spatiotemporal domain to the frequency domain for purposes of parameter estimation is complex, and presents a realistically intractable transformation.

The methods based on orthogonal collocation of finite elements [8] (OCFE) also has reduced-order and is computationally simpler than the full order DFN finite volume solution, with a complexity of $O(N^2)$, where $N \approx 1600$. Such a high number of states is clearly undesirable for state and parameter estimation during the short cycling times that result from high discharge rates. In contrast, the ANCF method results in comparable accuracy with much fewer states.

Rather than provide a comparison through computation times, the computational complexity of the proposed algorithm is presented as the order of complexity, O(.). Such a metric is widely used, and offers a degree of freedom for the designer to choose complexity as a function of node quantity, which directly effects the accuracy of any simulation. Specific simulation times are dependent on several elements, most importantly the processor capabilities of a given simulation computer, as well as the implementation of the nonlinear solution. If a user defines an explicit derivation of the Jacobian of the residual, $\frac{\partial \boldsymbol{R}_i^k}{\partial j^{l,k}}$, the solution speed is greatly improved. It is, however, possible to implement a method with a numerically perturbed Jacobian, which slows the convergence of the residual of the algebraic constraint, but allows for rapid development of the model. For the purposes of ubiquity, the computational complexity is presented for comparison of numerical methods.

3.5 ANCF II Model

While working with the ANCF model, it became clear that some of the goals pertaining to an observer would be complicated by the structure of the ANCF, and with modifications, the model could be better suited to the design of observers. This adjustment pertains to reducing the number of algebraic constraints, and subsequently reducing the overall number of states, but presumably comes at a cost, which is the loss of fidelity with respect to the higher-order model. Section 3.5.1 discusses the approach to reducing the constraints and states, through the usage of mixed basis functions. Section 3.5.2, discusses how this affects the expression of the solid dynamics, while Section 3.5.3 discusses the effect on the electrolyte dynamics. Finally, Section 3.5.4 explicates the changes to the Butler-Volmer kinetics, dictating the forcing functions for the dynamics in both the solid electrodes and electrolyte.

3.5.1 Mixed Basis Functions

The accuracy of the ANCF is founded on its use of polynomial basis functions, as described in Section 3.4.1. This can be a detriment for an observer because of the high number of degrees of freedom for its characterization. The full ANCF model implementation comes from a homogeneous structure, without consideration for where high degrees of freedom are needed, versus where limited state variables would benefit the observer construction. To remedy this fact, a second basis function is presented using a new pseudostate variable, $\theta^*(x,t)$, as well as the previous pseudostate variable, $\theta(x,t)$. These can again be conceptualized as surrogate variables for other concentration states, such as the bulk solid concentration, $\bar{c}_s^*(x,t)$, and solid concentration differential, $q^*(x,t)$; and the molar flux constraint, $j^*(x,t)$, in the case of $\theta^*(x,t)$, and the electrolyte concentration for $\theta(x,t)$. The distinction being made in notation is of a different basis function, specifically a linear basis function that is used to approximate the states with a * superscript, and the same polynomial basis from Section 3.4.1 otherwise. The solid electrode and separator volumes are again discretized into N nodes, defining $N-1$ elements along the dominant spatial dimension, x. The element length remains defined as,

$$l' = \frac{L}{N-1} \tag{3.88}$$

using L as the full length of the volume in question. A local coordinate, $\bar{x}_i(x,i)$, is defined as,

$$\bar{x}_i(x,i) = \frac{x-(i-1)l'}{l'} \tag{3.89}$$

for all elements, $i \in [1 \quad \dots \quad N-1]$, in the volumes. The change in notation is intended to add clarity with regards to the different basis functions. The same indexing function is defined,

$$\chi_i(x) = \begin{cases} 1 & \text{if } x \in \Big[\; il\text{'}, \quad (i{+}1)l\text{'} \; \Big], \\ 0 & \text{else.} \end{cases} \tag{3.90}$$

The characteristic polynomial remains for $\theta_i(\bar{x}_i, t)$,

$$\theta_i(\bar{x}_i, t) = \alpha_i(t) + \beta_i(t)\bar{x}_i + \gamma_i(t)\bar{x}_i^2 + \delta_i(t)\bar{x}_i^3 \tag{3.91}$$

but is altered for $\theta_i^*(\bar{x}_i, t)$,

$$\theta_i^*(\bar{x}_i, t) = \alpha_i(t) + \beta_i(t)\bar{x}_i \tag{3.92}$$

Using the indexing function of Equation (3.90), in conjunction with Equations (3.91) and (3.92), the full approximation is generated for each basis function, such that,

$$\theta(x, t) \approx \sum_{i=1}^{N-1} \chi_i(x)\theta_i(\bar{x}_i, t) \tag{3.93}$$

$$\theta^*(x, t) \approx \sum_{i=1}^{N-1} \chi_i(x)\theta_i^*(\bar{x}_i, t) \tag{3.94}$$

The same boundary conditions are used for Equation (3.91) as were delineated previously,

$$\begin{aligned} \theta_i(0, t) &= \psi_i(t) \\ \left.\frac{\partial \theta_i(\bar{x}_i, t)}{\partial \bar{x}_i}\right|_{\bar{x}_i=0} &= l' \frac{\partial \psi_i(t)}{\partial x} \\ \theta_i(1, t) &= \psi_{i+1}(t) \\ \left.\frac{\partial \theta_i(\bar{x}_i, t)}{\partial \bar{x}_i}\right|_{s_i=1} &= l' \frac{\partial \psi_{i+1}(t)}{\partial x} \end{aligned} \tag{3.95}$$

while Equation (3.92) uses a subset of those boundary conditions,

$$\begin{aligned} \theta_i(0,t) &= \psi_i(t) \\ \theta_i(1,t) &= \psi_{i+1}(t) \end{aligned} \tag{3.96}$$

Again, $\psi_i(t)$ represents the time-dependent value of either $\theta_i(\bar{x}_i,t)$ or $\theta_i^*(\bar{x}_i,t)$ at the i^{th} node. Herein lies the value of the new basis function, which has fewer degrees of freedom to estimate. However, the advantage of using the higher order polynomial basis functions was higher fidelity, and thus, a judicious choice must be made of where to apply the linear basis functions. The solution, then to Equation (3.91) becomes,

$$\begin{aligned} \theta_i(\bar{x}_i,t) =& \psi_i(t)(1-3\bar{x}_i^2+2\bar{x}_i^3) + l'\frac{\partial\psi_i(t)}{\partial x}(\bar{x}_i-2\bar{x}_i^2+\bar{x}_i^3) \\ &+ \psi_{i+1}(t)(3\bar{x}_i^2-2\bar{x}_i^3) + l'\frac{\partial\psi_{i+1}(t)}{\partial x}(-\bar{x}_i^2+\bar{x}_i^3) \end{aligned} \tag{3.97}$$

while the solution to Equation (3.92) becomes,

$$\theta_i^*(\bar{x}_i,t) = \psi_i(t)(1-\bar{x}_i) + \psi_{i+1}(t)(\bar{x}_i) \tag{3.98}$$

Equation (3.97) is again rewritten using a vector notation,

$$\theta_i(\bar{x}_i,t) = \boldsymbol{s}_i^\top \boldsymbol{\theta}_i(t) \tag{3.99}$$

where the state vector is also defined by,

$$\boldsymbol{\theta}_i(t) = \begin{bmatrix} \psi_i(t) & l'\frac{\partial\psi_i(t)}{\partial x} & \psi_{i+1}(t) & l'\frac{\partial\psi_{i+1}(t)}{\partial x} \end{bmatrix}^\top \tag{3.100}$$

and the coordinate weight vector,

$$\boldsymbol{s}_i = \begin{bmatrix} 1-3\bar{x}_i^2+2\bar{x}_i^3 \\ \bar{x}_i-2\bar{x}_i^2+\bar{x}_i^3 \\ 3\bar{x}_i^2-2\bar{x}_i^3 \\ -\bar{x}_i^2+\bar{x}_i^3 \end{bmatrix} \tag{3.101}$$

Conversely, Equation (3.98) is rewritten in vector notation as,

$$\theta_i^*(\bar{x}_i, t) = \boldsymbol{v}_i^\top \boldsymbol{\theta}_i^*(t) \tag{3.102}$$

where the new state vector is defined by,

$$\boldsymbol{\theta}_i^*(t) = \begin{bmatrix} \psi_i(t) & \psi_{i+1}(t) \end{bmatrix}^\top \tag{3.103}$$

and the new coordinate weight vector is defined by,

$$\boldsymbol{v}_i = \begin{bmatrix} 1 - \bar{x}_i \\ \bar{x}_i \end{bmatrix} \tag{3.104}$$

The expression in (3.101) is rewritten as,

$$\boldsymbol{s}_i = \begin{bmatrix} \mathrm{s}_1^i & \mathrm{s}_2^i & \mathrm{s}_3^i & \mathrm{s}_4^i \end{bmatrix}^\top \tag{3.105}$$

This implies that if a pseudostate pair is defined,

$$\boldsymbol{\psi}^i(t) = \begin{bmatrix} \psi_i(t) & l' \frac{\partial \psi_i(t)}{\partial x} \end{bmatrix}^\top \tag{3.106}$$

the element notation of Equation (3.99), can be rewritten as,

$$\theta_i(\bar{x}_i, t) = \begin{bmatrix} \mathrm{s}_1^i & \mathrm{s}_2^i \end{bmatrix} \boldsymbol{\psi}^i(t) + \begin{bmatrix} \mathrm{s}_3^i & \mathrm{s}_4^i \end{bmatrix} \boldsymbol{\psi}^{i+1}(t) \tag{3.107}$$

The use of these pseudostate pairs in the reconstruction of the actual spatiotemporal variable $\theta(x, t)$ is previously illustrated in Figure 3-5. Conversely, the linear basis function described in Equation (3.104), can be expressed as,

$$\boldsymbol{v}_i = \begin{bmatrix} \mathrm{v}_1^i & \mathrm{v}_2^i \end{bmatrix}^\top \tag{3.108}$$

no longer requiring a pseudostate pair, but instead, a state per node, such that

Equation (3.102) is rewritten as,

$$\theta_i^*(\bar{x}_i, t) = \mathrm{v}_1^i \psi^i(t) + \mathrm{v}_2^i \psi^{i+1}(t) \tag{3.109}$$

With the pseudostate pair in Equation (3.106), a complete state vector can be written, with respect to the variable $\theta(x, t)$ as,

$$\boldsymbol{\theta}(t) = \begin{bmatrix} \boldsymbol{\psi}^1(t) & \boldsymbol{\psi}^2(t) & \boldsymbol{\psi}^3(t) & \cdots & \boldsymbol{\psi}^{N-1}(t) & \boldsymbol{\psi}^N(t) \end{bmatrix}^\top \tag{3.110}$$

This, in turn, allows the underlying approximation in Equation (3.93) to be rewritten as,

$$\theta(x, t) \approx \begin{bmatrix} \mathrm{s}_1^1 \\ \mathrm{s}_2^1 \\ (\mathrm{s}_3^1 + \mathrm{s}_1^2) \\ (\mathrm{s}_4^1 + \mathrm{s}_2^2) \\ \vdots \\ (\mathrm{s}_3^{N-1} + \mathrm{s}_1^N) \\ (\mathrm{s}_4^{N-1} + \mathrm{s}_2^N) \\ \mathrm{s}_3^N \\ \mathrm{s}_4^N \end{bmatrix}^\top \boldsymbol{\theta}(t) \tag{3.111}$$

In addition, a full state vector is defined for the linear approximation shown in Equation (3.109), such that,

$$\boldsymbol{\theta}^*(t) = \begin{bmatrix} \psi^1(t) & \psi^2(t) & \psi^3(t) & \cdots & \psi^{N-1}(t) & \psi^N(t) \end{bmatrix}^\top \tag{3.112}$$

and subsequently Equation (3.94) becomes,

$$\theta^*(x,t) \approx \begin{bmatrix} \mathrm{v}_1^1 \\ (\mathrm{v}_2^1 + \mathrm{v}_1^2) \\ (\mathrm{v}_2^2 + \mathrm{v}_1^3) \\ \vdots \\ \left(\mathrm{v}_2^{N-1} + \mathrm{v}_1^N\right) \\ \mathrm{v}_2^N \end{bmatrix}^\top \boldsymbol{\theta}^*(t) \tag{3.113}$$

Both Equation (3.111) and (3.113) are available for use within the model, and the method of their mixing will become more clear in Sections 3.5.2 – 3.5.4. First and foremost, however, a determination must be made regarding their appropriate use within the model. For the purposes of the observers described in Chapter 4, it will be useful to reduce the overall number of constraints for a-priori estimation, while maintaining parallel plants in the solid regime. Additionally, it is clear from Equations (3.61) and (3.62) that matching the basis function representing the solid concentrations and molar flux is convenient, to eliminate additional system matrices. However, the advantage of the ANCF model is apparent from its incorporation of highly variable electrolyte dynamics, allowing for high fidelity during large current inputs. Therefore, the third-order polynomial basis function of Equation (3.111) is chosen to represent the electrolyte dynamics, $\boldsymbol{c}_e(t)$, while the linear basis function of Equation (3.113) is chosen to represent the solid dynamics, $\bar{\boldsymbol{c}}_s^*(t)$, $\boldsymbol{q}^*(t)$, and molar flux, $\boldsymbol{j}^*(t)$, using the * superscript to denote the linear basis function. The following sections describe how this change affects the ANCF model previously presented in Section 3.4.

3.5.2 Update to Solid Dynamics

As mentioned in Section 3.5.1, there is an advantage to using the same basis function for both the solid dynamics and the molar flux. The solid dynamics of the DFN are defined as,

$$\frac{\partial c_s^\pm(x,r,t)}{\partial t} = \frac{1}{r^2}\frac{\partial}{\partial r}\left(D_s^\pm r^2 \frac{\partial c_s^\pm(x,r,t)}{\partial r}\right) \tag{3.114}$$

$$\left.\frac{\partial c_s^{\pm}(x,r,t)}{\partial r}\right|_{r=0} = 0$$
$$\left.\frac{\partial c_s^{\pm}(x,r,t)}{\partial r}\right|_{r=R_p^{\pm}} = -\frac{j(x,t)}{D_s^{\pm}} \tag{3.115}$$

and the same approximation is maintained as presented in Equations (3.52) – (3.60). This results in a representation as repeated below,

$$\frac{\partial \bar{c}_s(x,t)}{\partial t} = -\frac{3}{R_p^{\pm}} j(x,t) \tag{3.116}$$

$$\frac{\partial q(x,t)}{\partial t} = -\frac{30D_s^{\pm}}{\left(R_p^{\pm}\right)^2} q(x,t) - \frac{45}{2\left(R_p^{\pm}\right)^2} j(x,t) \tag{3.117}$$

Now, using the linear basis function as described in Equation (3.113), these equations are transformed to,

$$\frac{d\bar{\boldsymbol{c}}_s^*(t)}{dt} = -\frac{3}{R_p^{\pm}} \boldsymbol{j}^*(t) \tag{3.118}$$

$$\frac{d\boldsymbol{q}^*(t)}{dt} = -\frac{30D_s^{\pm}}{\left(R_p^{\pm}\right)^2} \boldsymbol{q}^*(t) - \frac{45}{2\left(R_p^{\pm}\right)^2} \boldsymbol{j}^*(t) \tag{3.119}$$

$$\boldsymbol{c}_{ss}^* = \bar{\boldsymbol{c}}_s^*(t) + \frac{8R_p^{\pm}}{35} \boldsymbol{q}^* - \frac{R_p^{\pm}}{35D_s^{\pm}} \boldsymbol{j}^* \tag{3.120}$$

for $\bar{\boldsymbol{c}}_s^*(t) \in \mathbb{R}^N$, $\boldsymbol{q}^*(t) \in \mathbb{R}^N$, $\boldsymbol{j}^*(t) \in \mathbb{R}^N$, and $\boldsymbol{c}_{ss}^*(t) \in \mathbb{R}^N$. It should be noted that while the representation shown in Equations (3.118) – (3.120) use full system vectors, the pairs of states defining the solid concentration for each node, i, $\bar{c}_{s,i}^*(t)$ and $q_i^*(t)$, are independent of each other, allowing for the establishment of parallel single-input, single-output (SISO) systems. This formulation is defined by,

$$\begin{aligned} \dot{x}_i &= Ax_i(t) + Bj_i^*(t) \\ c_{ss,i}^*(t) &= C^{\top} x_i + Dj_i^*(t) \end{aligned} \tag{3.121}$$

with system matrices defined by,

$$A = \begin{bmatrix} 0 & 0 \\ 0 & -\frac{30D_s^{\pm}}{\left(R_p^{\pm}\right)^2} \end{bmatrix} \tag{3.122}$$

$$B = \begin{bmatrix} -\frac{3}{R_p^{\pm}} \\ -\frac{45}{2\left(R_p^{\pm}\right)^2} \end{bmatrix} \tag{3.123}$$

$$C = \begin{bmatrix} 1 \\ \frac{8R_p^{\pm}}{35} \end{bmatrix} \tag{3.124}$$

$$D = -\frac{R_p^{\pm}}{35D_s^{\pm}} \tag{3.125}$$

and a state vector, $x_i(t)$, defined as,

$$x_i(t) = \begin{bmatrix} \bar{c}_{s,i}^*(t) \\ q_i^*(t) \end{bmatrix} \tag{3.126}$$

Therefore, a full multiple-input, multiple-output (MIMO) system can be defined as,

$$\begin{aligned} \dot{\boldsymbol{x}} &= \bar{A}\boldsymbol{x}(t) + \bar{B}\boldsymbol{j}^*(t) \\ \boldsymbol{c}_{ss}^*(t) &= \bar{C}^\top \boldsymbol{x}(t) + \bar{D}\boldsymbol{j}^*(t) \end{aligned} \tag{3.127}$$

where the system matrices, with volume specific parameters denoted by the $(-)$ and $(+)$ subscripts, are defined as,

$$\bar{A} = \begin{bmatrix} A_- & 0 & \cdots & 0 & 0 \\ 0 & A_- & \cdots & 0 & 0 \\ \vdots & \vdots & \ddots & \vdots & \vdots \\ 0 & 0 & \cdots & A_+ & 0 \\ 0 & 0 & \cdots & 0 & A_+ \end{bmatrix} \tag{3.128}$$

$$\bar{B} = \begin{bmatrix} B_- & 0 & \cdots & 0 & 0 \\ 0 & B_- & \cdots & 0 & 0 \\ \vdots & \vdots & \ddots & \vdots & \vdots \\ 0 & 0 & \cdots & B_+ & 0 \\ 0 & 0 & \cdots & 0 & B_+ \end{bmatrix} \tag{3.129}$$

$$\bar{C} = \begin{bmatrix} C_- & 0 & \cdots & 0 & 0 \\ 0 & C_- & \cdots & 0 & 0 \\ \vdots & \vdots & \ddots & \vdots & \vdots \\ 0 & 0 & \cdots & C_+ & 0 \\ 0 & 0 & \cdots & 0 & C_+ \end{bmatrix} \tag{3.130}$$

$$\bar{D} = \begin{bmatrix} D_- & 0 & \cdots & 0 & 0 \\ 0 & D_- & \cdots & 0 & 0 \\ \vdots & \vdots & \ddots & \vdots & \vdots \\ 0 & 0 & \cdots & D_+ & 0 \\ 0 & 0 & \cdots & 0 & D_+ \end{bmatrix} \tag{3.131}$$

with $\bar{A} \in \mathbb{R}^{2N \times 2N}$, $\bar{B} \in \mathbb{R}^{2N \times N}$, $\bar{C} \in \mathbb{R}^{2N \times N}$, and $\bar{D} \in \mathbb{R}^{N \times N}$. The full state vector, $\boldsymbol{x}(t)$ is defined by,

$$\boldsymbol{x}(t) = \begin{bmatrix} x_1(t) \\ x_2(t) \\ \vdots \\ x_{N-1}(t) \\ x_N(t) \end{bmatrix} \tag{3.132}$$

for $\boldsymbol{x}(t) \in \mathbb{R}^{2N}$. The full system solid dynamics can be succinctly defined by Equation (3.127), but Equations (3.128) – (3.131) reveal that the states of the nodes are still independent of one another while sharing the same parameters for each volume, a trait to be leveraged in Chapter 4.

3.5.3 Update to Electrolyte Dynamics

The electrolyte dynamics as prescribed by the DFN model are,

$$\frac{\partial c_e(x,t)}{\partial t} = \frac{\partial}{\partial x}\left(D_e \frac{\partial c_e(x,t)}{\partial x}\right) + \frac{1}{F\epsilon_e}\frac{\partial (t_a^0 i_e(x,t))}{\partial x} \tag{3.133}$$

which matches the definition of Section 3.3.1. The boundary conditions are defined as,

$$\begin{aligned} \left.\frac{\partial c_e(x,t)}{\partial x}\right|_{x=0^-} &= 0 \\ \left.\frac{\partial c_e(x,t)}{\partial x}\right|_{x=0^+} &= 0 \end{aligned} \tag{3.134}$$

$$\begin{aligned} \epsilon_e^- \left.\left(D_e \frac{\partial c_e}{\partial x}\right)\right|_{x=L^-} &= \epsilon_e^{sep} \left.\left(D_e \frac{\partial c_e}{\partial x}\right)\right|_{x=0^{sep}} \\ \epsilon_e^{sep} \left.\left(D_e \frac{\partial c_e}{\partial x}\right)\right|_{x=L^{sep}} &= \epsilon_e^+ \left.\left(D_e \frac{\partial c_e}{\partial x}\right)\right|_{x=L^+} \end{aligned} \tag{3.135}$$

$$\begin{aligned} c_e(L^-,t) &= c_e(0^{sep},t) \\ c_e(L^{sep},t) &= c_e(L^+,t) \end{aligned} \tag{3.136}$$

Using a residual replaced with the vector representations of Equations (3.111) and (3.113) replacing the full-form spatiotemporal terms to turn the PDE into an ODE,

$$R_{1,i}(\bar{x}_i,t) = \boldsymbol{s}_i^\top \frac{d\boldsymbol{c}_{e,i}(t)}{dt} - \frac{D_i(t)}{(l')^2}\frac{d^2\boldsymbol{s}_i^\top}{d\bar{x}_i^2}\boldsymbol{c}_{e,i}(t) - \frac{t_a^0 a}{\epsilon_e}\boldsymbol{v}_i^\top \boldsymbol{j}_i^*(t) \tag{3.137}$$

Subsequently, this residual, $R_{1,i}(\bar{x}_i,t)$, is weighted with the polynomial weight vector, $\boldsymbol{s}_i$, to develop a solution for the time dynamics,

$$\int_0^1 \boldsymbol{s}_i R_{1,i}(\bar{x}_i,t)d\bar{x}_i = 0 \tag{3.138}$$

It should be noted that the same weight polynomial is chosen corresponding to the time-derivative term, such that an invertible matrix is developed. The explicit integration of Equation (3.138) is defined as,

$$\begin{aligned} 0 &= \int_0^1 \boldsymbol{s}_i\boldsymbol{s}_i^\top d\bar{x}_i \frac{d\boldsymbol{c}_{e,i}(t)}{dt} - \frac{D_i(t)}{(l')^2}\int_0^1 \boldsymbol{s}_i \frac{d^2\boldsymbol{s}_i^\top}{d\bar{x}_i^2} d\bar{x}_i \boldsymbol{c}_{e,i}(t) - \frac{t_a^0 a}{\epsilon_e}\int_0^1 \boldsymbol{s}_i\boldsymbol{v}_i^\top d\bar{x}_i \boldsymbol{j}_i^*(t) \\ &= \mathrm{M}\frac{d\boldsymbol{c}_{e,i}(t)}{dt} - \frac{D_i(t)}{(l')^2}\mathrm{K}\boldsymbol{c}_{e,i}(t) - \frac{t_a^0 a}{\epsilon_e}\mathrm{L}\boldsymbol{j}_i^*(t) \end{aligned} \tag{3.139}$$

where $\mathrm{M} \in \mathbb{R}^{4\times 4}$ is defined as,

$$\mathrm{M} = \int_0^1 \boldsymbol{s}_i \boldsymbol{s}_i^\top d\bar{x}_i \tag{3.140}$$

$\mathrm{K} \in \mathbb{R}^{4\times 4}$ is defined as,

$$\mathrm{K} = \int_0^1 \boldsymbol{s}_i \frac{d^2 \boldsymbol{s}_i^\top}{d\bar{x}_i^2} d\bar{x}_i \tag{3.141}$$

and $\mathrm{L} \in \mathbb{R}^{4\times 2}$ is defined as,

$$\mathrm{L} = \int_0^1 \boldsymbol{s}_i \boldsymbol{v}_i^\top d\bar{x}_i \tag{3.142}$$

The effective diffusion coefficient, $D_i(t)$, is defined the same as Equation (3.143),

$$D_i = \bar{D}_{e,i}(t) \epsilon_e^b \tag{3.143}$$

with the element-averaged electrolyte diffusion coefficient, $\bar{D}_e$ evaluated as,

$$\bar{D}_{e,i}(t) = 2.582 \times 10^{-9} e^{\left(-2.856\times 10^{-3} \bar{\boldsymbol{c}}_{e,i}(t)\right)} \tag{3.144}$$

and the average electrolyte concentration for an element, $\bar{\boldsymbol{c}}_{e,i}(t)$, given by,

$$\bar{\boldsymbol{c}}_{e,i}(t) = \int_0^1 \boldsymbol{s}_i^\top \boldsymbol{c}_{e,i}(t) d\bar{x}_i \tag{3.145}$$

To again construct the full system matrices, the individual weight matrices must be decomposed as in Section 3.4, such that,

$$\mathrm{M}^i = \int_0^1 \begin{bmatrix} \mathrm{M}_{11}^i & \mathrm{M}_{12}^i \\ \mathrm{M}_{21}^i & \mathrm{M}_{22}^i \end{bmatrix} d\bar{x}_i \tag{3.146}$$

where the submatrices of M^i are defined as,

$$\mathrm{M}^i_{jk} = \int_0^1 \begin{bmatrix} \mathrm{s}^i_{2j-1}\mathrm{s}^i_{2k-1} & \mathrm{s}^i_{2j-1}\mathrm{s}^i_{2k} \\ \mathrm{s}^i_{2j}\mathrm{s}^i_{2k-1} & \mathrm{s}^i_{2j}\mathrm{s}^i_{2k} \end{bmatrix} d\bar{x}_i, \tag{3.147}$$

$$j, k = 1, 2$$

and s^i_j denotes the jth element of the vector $\boldsymbol{s}_i$, as shown in Equation (3.105). Similarly, Equation (3.141) can be written as,

$$\mathrm{K}^i = \int_0^1 \begin{bmatrix} \mathrm{K}^i_{11} & \mathrm{K}^i_{12} \\ \mathrm{K}^i_{21} & \mathrm{K}^i_{22} \end{bmatrix} d\bar{x}_i \tag{3.148}$$

where the submatrices of K^i, are defined as,

$$\mathrm{K}^i_{jk} = \int_0^1 \begin{bmatrix} \mathrm{s}^i_{2j-1}\frac{d^2\mathrm{s}^i_{2k-1}}{ds_i^2} & \mathrm{s}^i_{2j-1}\frac{d^2\mathrm{s}^i_{2k}}{ds_i^2} \\ \mathrm{s}^i_{2j}\frac{d^2\mathrm{s}^i_{2k-1}}{ds_i^2} & \mathrm{s}^i_{2j}\frac{d^2\mathrm{s}^i_{2k}}{ds_i^2} \end{bmatrix} d\bar{x}_i, \tag{3.149}$$

$$j, k = 1, 2$$

Finally, the new addition to the dynamics because of the mixed basis functions is the L matrix, as defined in Equation (3.142).

$$\mathrm{L}^i = \int_0^1 \begin{bmatrix} \mathrm{L}^i_{11} & \mathrm{L}^i_{12} \\ \mathrm{L}^i_{21} & \mathrm{L}^i_{22} \end{bmatrix} d\bar{x}_i \tag{3.150}$$

where the submatrices of L^i are defined as,

$$\mathrm{L}^i_{jk} = \int_0^1 \begin{bmatrix} \mathrm{s}^i_{2j-1}\mathrm{v}^i_k \\ \mathrm{s}^i_{2j}\mathrm{v}^i_k \end{bmatrix} d\bar{x}_i, \qquad j,k = 1,2 \tag{3.151}$$

Using Equations (3.139), (3.146), (3.148), and (3.150) a set of ODEs that describes the electrolyte dynamics can be written as,

$$\begin{aligned} 0 = &\left(\mathrm{M}^{i-1}_{21}\frac{d\boldsymbol{c}^{i-1}_e}{dt} + \left(\mathrm{M}^i_{11} + \mathrm{M}^i_{22}\right)\frac{d\boldsymbol{c}^i_e}{dt} + \mathrm{M}^{i+1}_{12}\frac{d\boldsymbol{c}^{i+1}_e}{dt}\right) \\ &- \frac{1}{(l')^2}\left(D_{i-1}\mathrm{K}^{i-1}_{21}\boldsymbol{c}^{i-1}_e + \left(D_i\mathrm{K}^i_{11} + D_{i-1}\mathrm{K}^i_{22}\right)\boldsymbol{c}^i_e + D_i\mathrm{K}^{i+1}_{12}\boldsymbol{c}^{i+1}_e\right) \\ &+ \left(\frac{t^0_a a}{\epsilon_e}\right)\left(\mathrm{L}^{i-1}_{21} j^{i-1} + \left(\mathrm{L}^i_{11} + \mathrm{L}^i_{22}\right) j^i + \mathrm{L}^{i+1}_{12} j^{i+1}\right) \end{aligned} \tag{3.152}$$

where $\boldsymbol{c}^i_e$ and j^i denote the states corresponding to $\boldsymbol{c}_e(t)$ and $\boldsymbol{j}^*(t)$, respectively, defined as in Equations (3.106) and (3.108). The equation for the electrolyte dynamics, Equation (3.139), can be combined in vector form as,

$$0 = \mathbf{M}\frac{d\boldsymbol{c}_e(t)}{dt} - \frac{1}{(l')^2}\mathbf{K}\boldsymbol{c}_e(t) - \frac{t^0_a a}{\epsilon_e}\mathbf{L}\boldsymbol{j}^*(t) \tag{3.153}$$

where the full system integration matrix, $\mathbf{M} \in \mathbb{R}^{2N\times 2N}$, is defined by,

$$\mathbf{M} = \begin{bmatrix} \mathrm{M}^1_{11} & \mathrm{M}^1_{12} & 0 & 0 \\ \mathrm{M}^1_{21} & \mathrm{M}^1_{22} + \mathrm{M}^2_{11} & \mathrm{M}^2_{12} & 0 \\ 0 & \mathrm{M}^2_{21} & \ddots & \mathrm{M}^N_{12} \\ 0 & 0 & \mathrm{M}^{N-1}_{21} & \mathrm{M}^N_{22} \end{bmatrix} \tag{3.154}$$

while the matrix, $\mathbf{K} \in \mathbb{R}^{2N \times 2N}$, is defined by,

$$\mathbf{K} = \begin{bmatrix} D_1\mathrm{K}_{11}^1 & D_1\mathrm{K}_{12}^1 & 0 & 0 \\ D_1\mathrm{K}_{21}^1 & (D_1\mathrm{K}_{22}^1 + D_2\mathrm{K}_{11}^2) & D_2\mathrm{K}_{12}^2 & 0 \\ 0 & D_2\mathrm{K}_{21}^2 & \ddots & D_N\mathrm{K}_{12}^N \\ 0 & 0 & D_{N-1}\mathrm{K}_{21}^{N-1} & D_N\mathrm{K}_{22}^N \end{bmatrix} \tag{3.155}$$

and finally, the input matrix, $L \in \mathbb{R}^{2N \times N}$, is defined by,

$$\mathbf{L} = \begin{bmatrix} \mathrm{L}_{11}^1 & \mathrm{L}_{12}^1 & 0 & 0 \\ \mathrm{L}_{21}^1 & (\mathrm{L}_{22}^1 + \mathrm{L}_{11}^2) & \mathrm{L}_{12}^2 & 0 \\ 0 & \mathrm{L}_{21}^2 & \ddots & \mathrm{L}_{12}^N \\ 0 & 0 & \mathrm{L}_{21}^{N-1} & \mathrm{L}_{22}^N \end{bmatrix} \tag{3.156}$$

In summary, Equation (3.139), which describes the ODE counterpart of the electrolyte dynamics, can be rewritten as,

$$\frac{d\boldsymbol{c}_e(t)}{dt} = \frac{1}{(l')^2}\mathbf{M}^{-1}\mathbf{K}\boldsymbol{c}_e(t) + \frac{t_a^0 a}{\epsilon_e}\mathbf{M}^{-1}\mathbf{L}\boldsymbol{j}^*(t) \tag{3.157}$$

Note that the **K** matrix must contain the boundary conditions listed in Equations (3.134) – (3.136). The final result is a MIMO system, for estimation as defined in Chapter 4.

3.5.4 Update to Butler-Volmer Kinetics

The final piece of the model that needs to be addressed is the algebraic constraint of the Butler-Volmer kinetics. A weight vector is defined using the principles of Gaussian quadrature [1], which allows the definite integral of a function to be approximated as a sum of values defined at specific points, such that,

$$\int_{-1}^{1} f(x) \approx \sum_{i=1}^{n} \omega_i f(x_i) \tag{3.158}$$

choosing weights, $\omega_i = 1$, the points within the function, x_i, can be chosen as roots to the to Legendre polynomial,

$$0 = \frac{d}{dx}\left[(1-x^2)\frac{d}{dx}P_n(x)\right] + n(n+1)P_n(x) \tag{3.159}$$

For $n = 4$, which is the number of points for an element using the polynomial basis function of Equation (3.91), the Legendre polynomial is defined as,

$$P_n(x) = \frac{35x^4 - 30x^2 + 3}{8} \tag{3.160}$$

This is not entirely suitable, however, as the interval is calculated over $[-1, 1]$, and the desired interval for any element is $[0, 1]$. Therefore, the roots of Equation (3.160), defined as $\tilde{w}$, can be shifted to the desired roots, w, using,

$$w = \frac{1 + \tilde{w}}{2} \tag{3.161}$$

The desired roots, w, on the interval [0,1] are calculated as,

$$w = \begin{bmatrix} 0.0694 \\ 0.3300 \\ 0.6700 \\ 0.9306 \end{bmatrix} \tag{3.162}$$

Using this weight vector, w, a subsequent weight matrix is defined, for the purposes of approximating the integral of a pseudostate by way of the Legendre-Gaussian quadrature weight vector established in Equation (3.162),

$$\int \theta_i(\bar{x}_i, t)d\bar{x}_i \approx \boldsymbol{s}_i^\top\big|_{\bar{x}_i = w}\boldsymbol{\theta}_i(t) \tag{3.163}$$

Where, for convenience, the weight matrix is defined as,

$$\mathrm{W}_1 = \boldsymbol{s}_i^\top\big|_{\bar{x}_i = w} \tag{3.164}$$

Additionally, another weight matrix must be established to approximate the double integral of a pseudostate, such that,

$$\int\int \theta_i(\bar{x}_i,t)d\bar{x}_i d\bar{x}_i \approx \left[\int_0^{\bar{x}_i} \boldsymbol{s}_i^\top d\bar{x}_i\right]\Bigg|_{\bar{x}_i=w} \boldsymbol{\theta}_i(t) \tag{3.165}$$

The resulting integration weight matrix, W_2, is defined as,

$$\mathrm{W}_2 = \left[\int_0^{\bar{x}_i} \boldsymbol{s}_i^\top d\bar{x}_i\right]\Bigg|_{\bar{x}_i=w} \tag{3.166}$$

These matrices will aid in the definition of the terms necessary for constraining the Butler-Volmer kinetics. In the interest of integrating the solid potential, another matrix is defined using the definite integral of $\boldsymbol{s}_i$,

$$\begin{aligned}\int_0^1\int_0^{\bar{x}_i} \boldsymbol{s}_i^\top d\bar{x}_i d\bar{x}_i &= \begin{bmatrix} q_{11} & q_{12} & q_{13} & q_{14}\end{bmatrix}\\ \int_0^1 \boldsymbol{s}_i^\top d\bar{x}_i &= \begin{bmatrix} q_{21} & q_{22} & q_{23} & q_{24}\end{bmatrix}\end{aligned} \tag{3.167}$$

$$\mathbf{Q}_\pm = \begin{bmatrix} q_{11} & q_{12} & q_{13} & q_{14} & 0 & 0 & \cdots & 0 & 0 & 0 & 0 \\ q_{21} & q_{22} & q_{23} & q_{24} & 0 & 0 & \cdots & 0 & 0 & 0 & 0 \\ 0 & 0 & q_{11} & q_{12} & q_{13} & q_{14} & \cdots & 0 & 0 & 0 & 0 \\ 0 & 0 & q_{21} & q_{22} & q_{23} & q_{24} & \cdots & 0 & 0 & 0 & 0 \\ 0 & 0 & 0 & 0 & q_{11} & q_{12} & \cdots & 0 & 0 & 0 & 0 \\ 0 & 0 & 0 & 0 & q_{21} & q_{22} & \cdots & 0 & 0 & 0 & 0 \\ \vdots & \vdots & \vdots & \vdots & \vdots & \vdots & \ddots & \vdots & \vdots & \vdots & \vdots \\ 0 & 0 & 0 & 0 & 0 & 0 & \cdots & q_{13} & q_{14} & 0 & 0 \\ 0 & 0 & 0 & 0 & 0 & 0 & \cdots & q_{23} & q_{24} & 0 & 0 \\ 0 & 0 & 0 & 0 & 0 & 0 & \cdots & q_{11} & q_{12} & q_{13} & q_{14} \\ 0 & 0 & 0 & 0 & 0 & 0 & \cdots & q_{21} & q_{22} & q_{23} & q_{24} \end{bmatrix} \tag{3.168}$$

$\mathbf{Q}_\pm$ is used to integrate the solid potential for either volume, and because values for one of the nodes are known due to boundary conditions $\mathrm{Q}_\pm \in \mathbb{R}^{2(N_\pm-1)\times 2N_\pm}$, where $N_\pm$ is the number of nodes in either volume. Conversely, another weight matrix is defined of the form,

$$\mathbf{P}_{\pm} = \begin{bmatrix} 1 & 0 & 0 & 0 & 0 & 0 & \\ 0 & 1 & 0 & 0 & 0 & 0 & \\ -1 & -1 & 1 & 0 & 0 & 0 & \\ 0 & -1 & 0 & 1 & 0 & 0 & \\ 0 & 0 & -1 & -1 & 1 & 0 & \\ 0 & 0 & 0 & -1 & 0 & 1 & \\ & & & & & & \ddots \end{bmatrix} \tag{3.169}$$

for $\mathbf{P}_{\pm} \in \mathbb{R}^{2(N_{\pm}-1)\times 2N_{\pm}}$, representing the inverse of a second derivative weighting matrix.

It is possible to transition between the linear and polynomial bases using Galerkin collocation, and for the purposes of calculating the constraint to a higher accuracy, the linear bases are translated into the polynomial base using the expression,

$$\begin{aligned} \boldsymbol{s}_i^{\top}\boldsymbol{\theta}_i(t) &= \boldsymbol{v}_i^{\top}\boldsymbol{\theta}_i^*(t) \\ \int \boldsymbol{s}_i\boldsymbol{s}_i^{\top} d\bar{x}_i\boldsymbol{\theta}_i(t) &= \int \boldsymbol{s}_i\boldsymbol{v}_i^{\top} d\bar{x}_i\boldsymbol{\theta}_i^*(t) \\ \mathrm{M}\boldsymbol{\theta}_i(t) &= \mathrm{L}\boldsymbol{\theta}_i^*(t) \\ \boldsymbol{\theta}_i(t) &= \mathrm{M}^{-1}\mathrm{L}\boldsymbol{\theta}_i^*(t) \end{aligned} \tag{3.170}$$

Given that the molar flux, $\boldsymbol{j}^*(t)$, and the solid electrode states, $\bar{\boldsymbol{c}}_s^*(t)$ and $\boldsymbol{q}^*(t)$, only pertain to the space outside of the separator, polynomial approximations can be constructed for any appropriate pseudostate relative to the anode or cathode using full volume transition matrices, such that,

$$\boldsymbol{\theta}^{\pm}(t) = \mathbf{M}_{\pm}^{-1}\mathbf{L}_{\pm}\boldsymbol{\theta}_{\pm}^*(t) \tag{3.171}$$

where $\mathbf{M}_{\pm}$ and $\mathbf{L}_{\pm}$ are constructed in a similar fashion to that shown in Equations (3.154) and (3.156), respectively.

The next step is to establish the solid potential, $\boldsymbol{\phi}_s^{\pm} \in \mathbb{R}^{2N_{\pm}}$, for both volumes.

Using an initial guess from a solver, the vector can be constructed as,

$$\begin{aligned}
\boldsymbol{\phi}_{s,1}^{\pm} &= \phi_{s,0}^{\pm} \\
\boldsymbol{\phi}_{s,2}^{\pm} &= -\frac{Il'}{\sigma^{\pm}} \\
\boldsymbol{\phi}_{s,j}^{\pm} &= \mathbf{P}_{\pm}^{-1}\left[\frac{a^{\pm}F\left(l'\right)^{2}}{\sigma^{\pm}}\mathbf{Q}_{\pm}\mathbf{M}_{\pm}^{-1}\mathbf{L}_{\pm}\boldsymbol{j}_{\pm}^{*} + C_{\pm}\right]
\end{aligned} \tag{3.172}$$

for $j \in \begin{bmatrix} 3 & \cdots & 2N_{\pm} \end{bmatrix}$, and where the integration constant, $C_{\pm}$, is defined as,

$$C_{\pm} = \begin{bmatrix} \phi_{s,0}^{\pm} \\ 0 \\ \vdots \\ 0 \end{bmatrix} \tag{3.173}$$

for $C_{\pm} \in \mathbb{R}^{2(N_{\pm}-1)}$. Subsequently, this vector is expanded to four collocation points per element for $i \in \begin{bmatrix} 1 & \cdots & N_{\pm}-1 \end{bmatrix}$, shown in Equation (3.174).

$$\boldsymbol{\phi}_{s\delta,j}^{\pm} = \frac{a^{\pm}F\left(l'\right)^{2}}{\sigma^{\pm}}\mathrm{W}_{2}\boldsymbol{j}_{k}^{\pm} + \boldsymbol{\phi}_{s,2(i-1)+2}^{\pm}w + \boldsymbol{\phi}_{s,2(i-1)+1}^{\pm}\begin{bmatrix} 1 \; 1 \; 1 \; 1 \end{bmatrix}^{\top} \tag{3.174}$$

where the subscripts denote a subset of vector elements as $j \in \begin{bmatrix} 4(i-1)+1 & \cdots & 4i \end{bmatrix}$, $k \in \begin{bmatrix} 2(i-1)+1 & \cdots & 2(i+1) \end{bmatrix}$, and $\boldsymbol{\phi}_{s\delta}^{\pm} \in \mathbb{R}^{4(N_{\pm}-1)}$ are the collocation points of the solid potential. The polynomial approximation of the molar flux for a volume, $\boldsymbol{j}^{\pm} \in \mathbb{R}^{2N_{\pm}}$, is defined as,

$$\boldsymbol{j}^{\pm} = \mathbf{M}_{\pm}^{-1}\mathbf{L}_{\pm}\boldsymbol{j}_{\pm}^{*} \tag{3.175}$$

The surface concentration for each volume, $\boldsymbol{c}_{ss}^{\pm} \in \mathbb{R}^{2N_{\pm}}$ can likewise be defined in the polynomial space as,

$$\boldsymbol{c}_{ss}^{\pm} = \mathbf{M}_{\pm}^{-1}\mathbf{L}_{\pm}\boldsymbol{c}_{ss,\pm}^{*} \tag{3.176}$$

The calculations are continued with an expression for the electrolyte potential of either volume, $\boldsymbol{\phi}_{e\delta}^{\pm}$ using the same iterative process as Equation (3.174) for $i \in \begin{bmatrix} 1 & \cdots & N_{\pm}-1 \end{bmatrix}$, at four collocation points per element, shown in Equation

(3.178). An integration vector is also calculated, as shown in Equation (3.177).

$$x_{\delta,j} = l'\left((i-1)\begin{bmatrix} 1 & 1 & 1 & 1 \end{bmatrix}^{\top} + w\right) \tag{3.177}$$

$$\begin{aligned}\boldsymbol{\phi}^{\pm}_{e\delta,j} &= \\ -\frac{I}{\sigma^{\pm}}x_{\delta,j} - \frac{\sigma^{\pm}}{\kappa^{\pm}}\left(\boldsymbol{\phi}^{\pm}_{s\delta,j} - \phi^{\pm}_{s,0}\right) &- \frac{2RT}{F}\left(1 - t^{\pm}_{0}\right)\left(\ln(\boldsymbol{c}^{\pm}_{e\delta,j}) - \ln(\boldsymbol{c}^{\pm}_{e,1})\right) + \phi^{\pm}_{e,0}\end{aligned} \tag{3.178}$$

where $\phi^{-}_{e,0} = 0$ and $\phi^{+}_{e,0}$ is defined in Equation (3.179).

$$\phi^{+}_{e,0} = -\frac{IL^{-}}{\kappa^{-}} - \frac{\sigma^{-}}{\kappa^{-}}\left(\boldsymbol{\phi}^{-}_{s,2(N_{-}-1)+1} - \phi^{-}_{s,0}\right) \tag{3.179}$$

The collocation points of the electrolyte, $\boldsymbol{c}_{e\delta,j} \in \mathbb{R}^4$, as shown in Equation (3.178), is defined by Equation (3.180).

$$\boldsymbol{c}^{\pm}_{e\delta,j} = \mathrm{W}_1\boldsymbol{c}^{\pm}_{e,k} \tag{3.180}$$

Both the molar flux and surface concentration are calculated at the collocation points, shown in Equations (3.181) and (3.182), respectively.

$$\boldsymbol{j}^{\pm}_{\delta,j} = \mathrm{W}_1\boldsymbol{j}^{\pm}_{k} \tag{3.181}$$

$$\boldsymbol{c}^{\pm}_{ss\delta,j} = \mathrm{W}_1\boldsymbol{c}^{\pm}_{ss,k} \tag{3.182}$$

The open-circuit potential is calculated using the collocated surface concentration values such that,

$$\boldsymbol{\mathcal{U}}^{\pm}_{\delta,j} = \mathcal{U}^{\pm}\left(\boldsymbol{c}^{\pm}_{ss\delta,j}\right) \tag{3.183}$$

The overpotential is calculated at each of these collocation points as shown in Equation (3.184).

$$\boldsymbol{\eta}^{\pm}_{\delta,j} = \boldsymbol{\phi}^{\pm}_{s\delta,j} - \boldsymbol{\phi}^{\pm}_{e\delta,j} - \boldsymbol{\mathcal{U}}^{\pm}_{\delta,j} \tag{3.184}$$

Subsequently, an exchange current density is calculated as,

$$\boldsymbol{i}^{\pm}_{0\delta,j} = k^{\pm}f\left(\boldsymbol{c}^{\pm}_{e\delta,j}, \alpha^{-}\right) \odot f\left(c^{\pm}_{ss,max} - \boldsymbol{c}^{\pm}_{ss\delta,j}, \alpha^{-}\right) \odot f\left(\boldsymbol{c}^{\pm}_{ss\delta,j}, \alpha^{+}\right) \tag{3.185}$$

Where the operator $\odot$ denotes element-wise multiplication, and the function $f\left(\boldsymbol{\theta}_{\delta}^{\pm}, \alpha^{\pm}\right)$ is a function that takes a vector and a scalar as arguments, and produces a vector with each element, r, defined as,

$$f_r\left(\boldsymbol{\theta}_{\delta}^{\pm}, \alpha^{\pm}\right) = \left(\boldsymbol{\theta}_{\delta,r}^{\pm}\right)^{\alpha^{\pm}} \tag{3.186}$$

Using the overpotential and exchange current density, a resulting molar flux for each volume is calculated at collocation points,

$$\hat{\boldsymbol{j}}_{\delta,j}^{\pm} = 2\boldsymbol{i}_{0\delta,j}^{\pm} \sinh\left(\frac{F}{2RT}\boldsymbol{\eta}_{\delta,j}\right) \tag{3.187}$$

Finally, a residual for each volume is calculated such that,

$$\boldsymbol{R}_{\delta,j}^{\pm} = \hat{\boldsymbol{j}}_{\delta,j}^{\pm} - \boldsymbol{j}_{\delta,j}^{\pm} \tag{3.188}$$

Two additional residual terms are used to ensure convergence, as shown in Equation (3.189).

$$R_1^{\pm} = \left(\sum_{i=1}^{N_{\pm}-1} \int_0^1 \boldsymbol{s}_i^{\top} d\bar{x}_i j_k^{\pm}\right) \pm I(t) \tag{3.189}$$

which represents the difference of the integral of the molar flux and the current. For Equations (3.174) – (3.189), the subscripts j and k denote subsets of vectors as defined by a top level index i, such that,

$$\begin{aligned} j &\in \begin{bmatrix} 4(i-1)+1 & \cdots & 4i \end{bmatrix} \\ k &\in \begin{bmatrix} 2(i-1)+1 & \cdots & 2(i+1) \end{bmatrix} \\ i &\in \begin{bmatrix} 1 & \cdots & N_{\pm}-1 \end{bmatrix} \end{aligned} \tag{3.190}$$

This allows for a looped approach rather than a full-system matrix, to individually address the nonlinearities. To solve this system, a full residual is created as shown in

Equation (3.191).

$$\boldsymbol{R} = \begin{bmatrix} \boldsymbol{R}_\delta^- \\ \boldsymbol{R}_\delta^+ \\ R_1^- \\ R_1^+ \end{bmatrix} \tag{3.191}$$

An input vector to the nonlinear solution, z, is defined as,

$$\boldsymbol{z} = \begin{bmatrix} \boldsymbol{j}^* \\ \phi_{s,0}^+ \\ \phi_{s,0}^- \end{bmatrix} \tag{3.192}$$

The solution $\boldsymbol{z}$ is varied using the update law,

$$\boldsymbol{z}^{k+1} = \boldsymbol{z}^k + \Delta\boldsymbol{z} \tag{3.193}$$

where $\Delta\boldsymbol{z}$ for each iteration k is calculated as the solution to,

$$\frac{\partial\boldsymbol{R}}{\partial\boldsymbol{z}^k}\Delta\boldsymbol{z} = -\boldsymbol{R} \tag{3.194}$$

while the norm of the residual, $\boldsymbol{R}$, is greater than an error tolerance, $\epsilon_{\boldsymbol{R}}$,

$$\|\boldsymbol{R}\| \geq \epsilon_{\boldsymbol{R}} \tag{3.195}$$

The resulting molar flux, $\boldsymbol{j}^*$, is used to drive the dynamics as outlined in Sections 3.5.2 and 3.5.3.

3.5.5 Overall ANCF II Model

The complete ANCF II model is defined by ordinary differential equations in Equations (3.118), (3.119) and (3.157), with a molar flux approximation, $\boldsymbol{j}^*(t)$, defined by the minimization of a residual, $\boldsymbol{R}$, shown in Equation (3.191), and achieved through Equation (3.194). Finally, the output voltage is calculated as the resulting difference between the solid potential at the current collectors, such that,

$$V(t) = \phi_{s,0}^{+}(t) - \phi_{s,0}^{-}(t) \tag{3.196}$$

These equations define the full ANCF II model, and are implemented with a similar algorithm to that shown in Algorithm 1. The model validation shown in Section 3.6 was achieved with simulations using the parameters of Table 3.1.

3.6 Model Validation

Table 3.1: Physical parameter definitions and values used for simulation, based on a $LiCoO_2/LiC_6$ cell.

Symbol	**Description**	**Values**			
		Anode	*Separator*	*Cathode*	*Units*
a	Specific interfacial area	$7.236e5$	—	$8.850e5$	m^{-1}
α	Ionic transfer coefficient	0.5	—	0.5	—
b	Bruggeman coefficient	0.5	—	0.5	—
c_e^0	Initial electrolyte concentration	1000	—	1000	$mol - m^{-3}$
$c_{s,max}$	Maximum ionic concentration capacity in the electrode	30555	—	51554	$mol - m^{-3}$
D_s	Effective solid electrode diffusion coefficient	$1.0e - 14$	—	$3.9e - 14$	m^2s^{-1}
ϵ_e	Electrolyte volume fraction	0.485	0.724	0.385	—
ϵ_f	Binding material volume fraction	0.0326	—	0.0250	—
k	Reaction constant	$5.0307e - 11$	—	$2.3340e - 11$	—
κ	Electrolyte ionic conductivity coefficient	0.3	—	0.3	$\Omega^{-1}m^{-1}$
κ_{eff}	Effective electrolyte ionic conductivity	$\kappa_{eff} = \kappa\epsilon_e^{brugg}$			$\Omega^{-1}m^{-1}$
L	Compartment length	$88e - 6$	$25e - 6$	$80e - 6$	m
R_p	Solid electrode pseudo-sphere radius	$2e - 6$	—	$2e - 6$	m
R_{SEI}	Electrode-electrolyte interphase resistivity	0	—	0	Ωm^2
σ	Electrode conductivity	100	—	100	$\Omega^{-1}m^{-1}$
σ_{eff}	Effective electrode conductivity	$\sigma_{eff} = \sigma(1 - \epsilon_e - \epsilon_f)$			$\Omega^{-1}m^{-1}$
T	Isothermal temperature	297.15	297.15	297.15	K
t^0	Ionic transference number	0.637	—	0.363	—

In this section, the ANCF and ANCF II model were numerically validated, and their outputs were compared with that from the *DualFoil* model [38], developed from the DFN model [15], for a range of charge and discharge rates. The parameters used for these simulations are shown in Table 3.1, derived from the physical parameters of a Lithium Cobalt Oxide cell, $LiCoO_2/LiC_6$. The ANCF and ANCF II results are also compared with the SPM model mentioned in Section 3.3.3 [54]. For the sake of completeness, the simulation setup of the SPM is described below.

The implemented SPM model equations are similar to Equations (3.29) - (3.36), except that a specific solution is defined using volume projection. This manifests in the solid concentration as,

$$\frac{d\bar{c}_s^{\pm}(t)}{dt} = \mp \frac{3}{Fa^{\pm}L^{\pm}R_p^{\pm}} I(t) \tag{3.197}$$

defines the bulk solid concentration in each respective volume, and,

$$\frac{dq^{\pm}(t)}{dt} = -\frac{30D_s^{\pm}}{\left(R_p^{\pm}\right)^2} q^{\pm}(t) \mp \frac{45}{2Fa^{\pm}L^{\pm}\left(R_p^{\pm}\right)^2} I(t) \tag{3.198}$$

defines the concentration differential for each solid. The surface concentration is defined similarly to Eq. (3.56),

$$c_{ss}^{\pm}(t) = \bar{c}_s^{\pm}(t) + \frac{8R_p^{\pm}}{35} q(t) \mp \frac{R_p^{\pm}}{35Fa^{\pm}L^{\pm}D_s^{\pm}} I(t) \tag{3.199}$$

The Butler-Volmer kinetics of Eq. (3.17) are still valid for each volume, with the molar flux, $j(x,t)$, explicitly defined as

$$j^{\pm}(t) = \mp \frac{I(t)}{Fa^{\pm}L^{\pm}}. \tag{3.200}$$

For the same parameters as shown in Table 3.1, the ANCF model, from Section 3.6.1; the ANCF II model, from Section 3.6.2; the DFN model, and SPM model as described above were simulated. Four simulations, at different discharge rates of 0.1C, 1C, 2C, and 3C, are shown, in addition to a subset of the Urban Dynamometer Driving Schedule (UDDS). In order to compare their performances quantitatively, an

RMS metric of the tracking error was chosen as,

$$E_{RMS} = \sqrt{\frac{1}{N}\sum_{i=0}^{N}\left(\frac{V_{s,i} - V_{d,i}}{V_{d,i}}\right)^2} \tag{3.201}$$

where $V_{d,i}$ is data obtained from the DualFoil simulation, and $V_{s,i}$ denotes the response from the ANCF, the ANCF II, or the SPM model. Another error metric, ΔE, was defined as,

$$\Delta E = E_{RMS,ANCF} - E_{RMS,SPM}. \tag{3.202}$$

with the subscripts ANCF and SPM denoting E_{RMS} corresponding to the modeling errors of the ANCF/II, and SPM, respectively.

3.6.1 ANCF Results

Low and Constant Discharge of 0.1C

As can be seen from Figure 3-6, the responses of the ANCF model coincide well with that of the DFN model. It is also noted that the SPM response agrees quite well with the DFN model, confirming prior observations [11] [16] that for low discharge rates, the SPM response is quite accurate. The overall tracking error is quantified in Table 3.2, which shows that the SPM results in a slightly better RMS value compared to that of the ANCF.

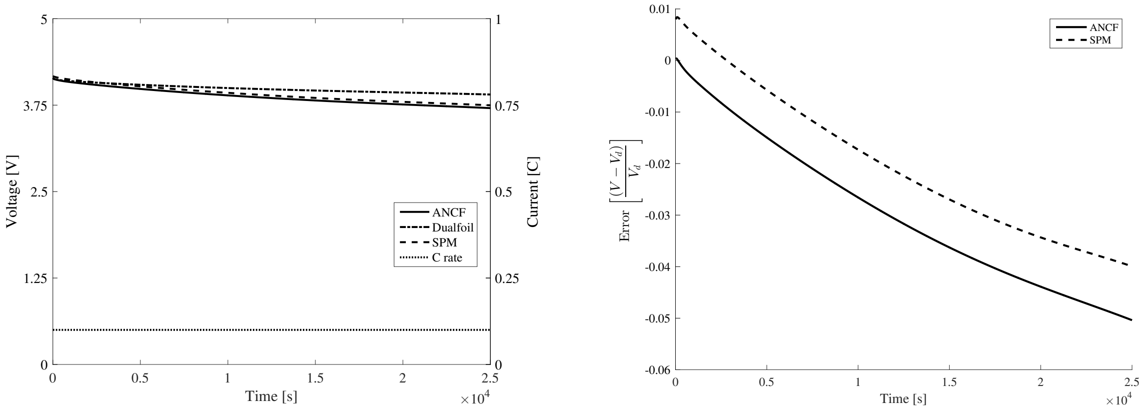

Figure 3-6: Simulation results on the left for the ANCF model, SPM model, and DualFoil, at 0.1C for 2.5×10^4 seconds. Error results are shown to the right, normalized against the Dualfoil results.

Medium Discharge Rate of 1C Pulses

From Figure 3-7, it is easy to see that the ANCF responses match that of the Dualfoil quite closely, except at the discharging and charging limits. In contrast, the SPM model falls behind in capturing the steady-state values. Table 3.2, once again, provides a quantitative summary of the RMS errors and peak errors. It can be argued that at the limits, where the ANCF performs poorly, the reliability of the DualFoil is also questionable.

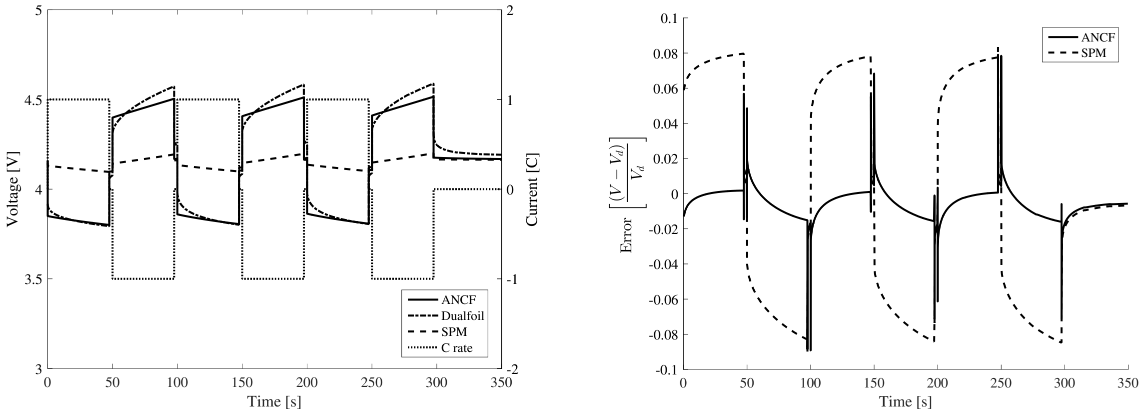

Figure 3-7: Simulation results on the left for the ANCF model, SPM model, and DualFoil, at 1C for 350 seconds. Error results are shown to the right, normalized against the Dualfoil results.

High Discharge Rates of 2C and 3C Pulses

Figures 3-8 and 3-9 show the responses of the ANCF, DualFoil, and SPM models. It is noted that in both cases, the ANCF maintains the same dramatic improvement over the SPM, and underscores the main advantage of the ANCF in relation to the retension of spatiotemporal electrolyte dynamics. All RMS errors are summarized in Table 3.2.

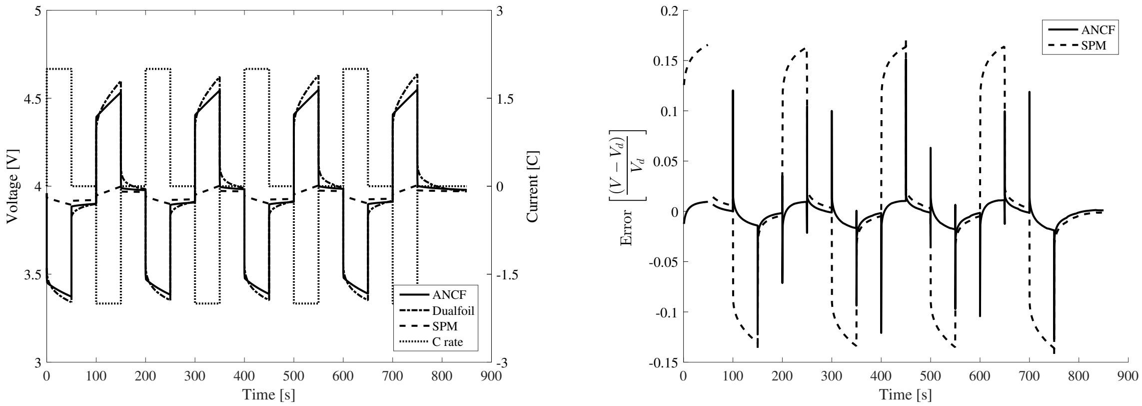

Figure 3-8: Simulation results on the left for the ANCF model, SPM model, and DualFoil, at 2C for 850 seconds. Error results are shown to the right, normalized against the Dualfoil results.

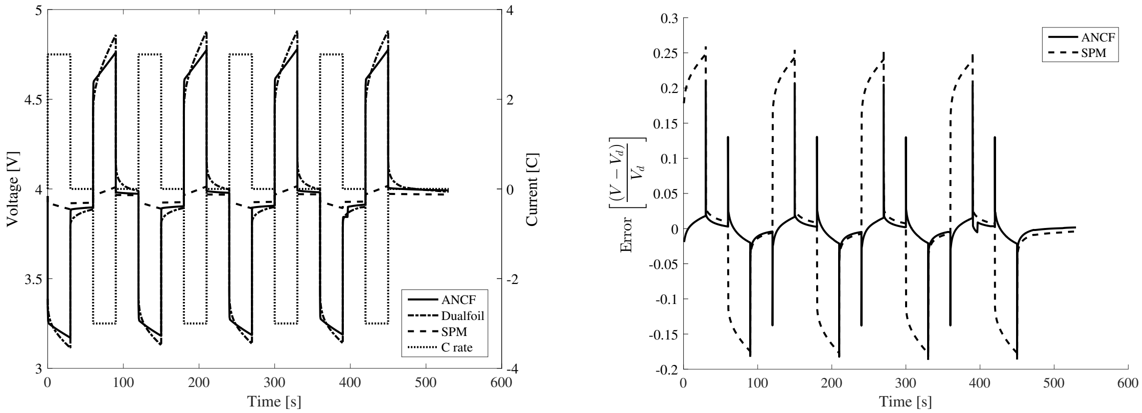

Figure 3-9: Simulation results on the left for the ANCF model, SPM model, and DualFoil, at 3C for 530 seconds. Error results are shown to the right, normalized against the Dualfoil results.

UDDS Discharge Profile

Figure 3-10 shows the results of the UDDS profile, as standardized by the EPA. This UDDS profile is given in terms of vehicle speed, so an approximate model of a car was derived with respect to the specific current profile necessary to generate such speeds, under the energy consumption of a given electric motor and drag coefficient.

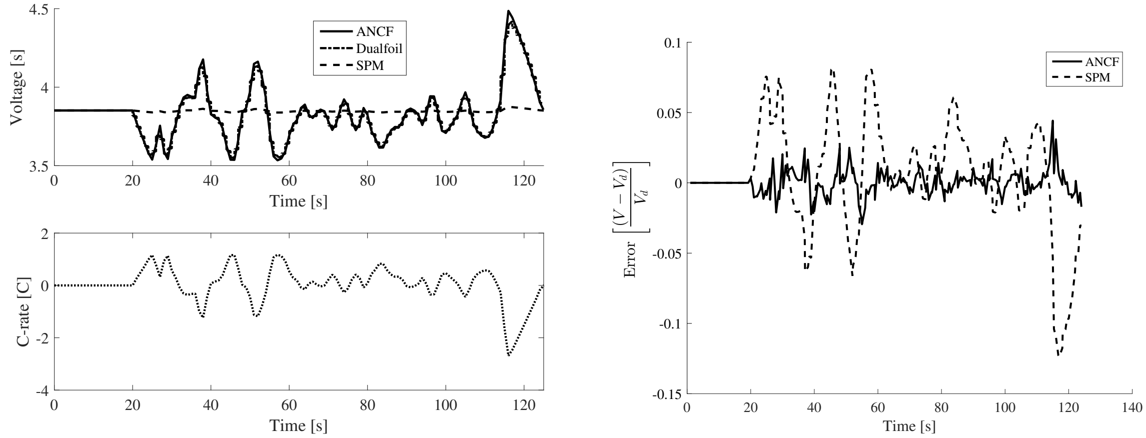

Figure 3-10: Simulation results on the left for the ANCF model, SPM model, and DualFoil, for a subset of the UDDS profile. Error results are shown to the right, normalized against the Dualfoil results.

3.6.2 ANCF II Results

Low and Constant Discharge of 0.1C

Figure 3-11 shows the results of a low, constant discharge of the ANCF II model cell at 0.1C, similar to Figure 3-6. It is notable that the simulation maintains a high accuracy until the nonlinear regime at the end of the time duration, where the SPM also fails. The errors are shown in Table 3.3.

Medium Discharge Rate of 1C Pulses

Figure 3-12 shows the simulation results of the ANCF II model for 1C pulsing. Simulation results show excellent matching to the DFN model, while the SPM shows a lack of sensitivity to higher discharge rates. The ANCF II is more than six times more accurate than the SPM, as shown in Table 3.3.

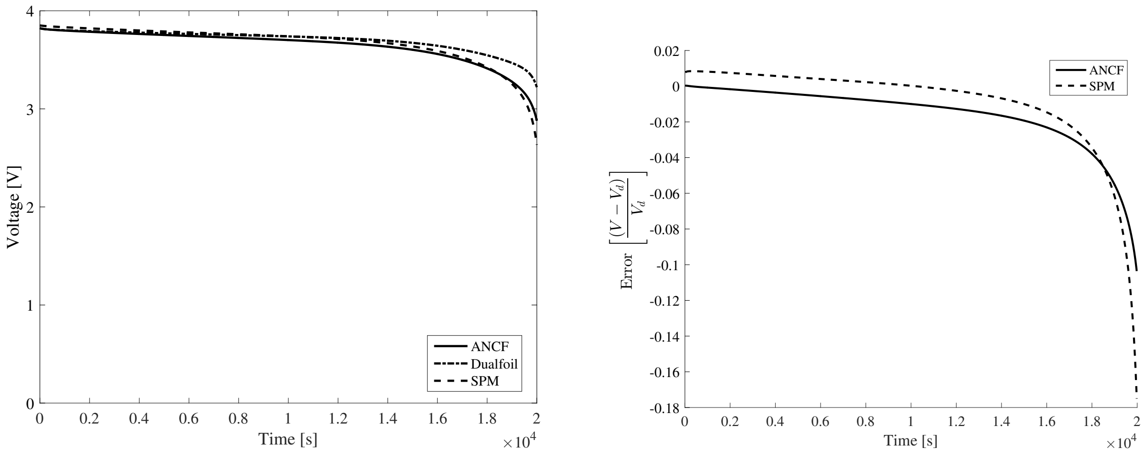

Figure 3-11: Simulation results on the left for the ANCF model, SPM model, and DualFoil, at 1C for 350 seconds. Error results are shown to the right, normalized against the Dualfoil results.

High Discharge Rates of 2C and 3C Pulses

Figures 3-13 and 3-14 show a 2C and 3C discharge profile, representing more severe dynamics to match. It should be noted that the ANCF II performs well for these simulations as well, but performance accuracy drops similarly to the ANCF model, while maintaining superior performance to the SPM results. RMS errors are shown in Table 3.3.

UDDS Discharge Profile

Finally, Figure 3-15 shows the simulation results of the same UDDS subset used for the ANCF model. Again, this is a standard vehicle simulation profile, that was made to replicate a vehicle in particular driving conditions, with an electric vehicle motor consuming power as a function of the amount of force required to overcome drag effects. RMS error values are shown in Table 3.3.

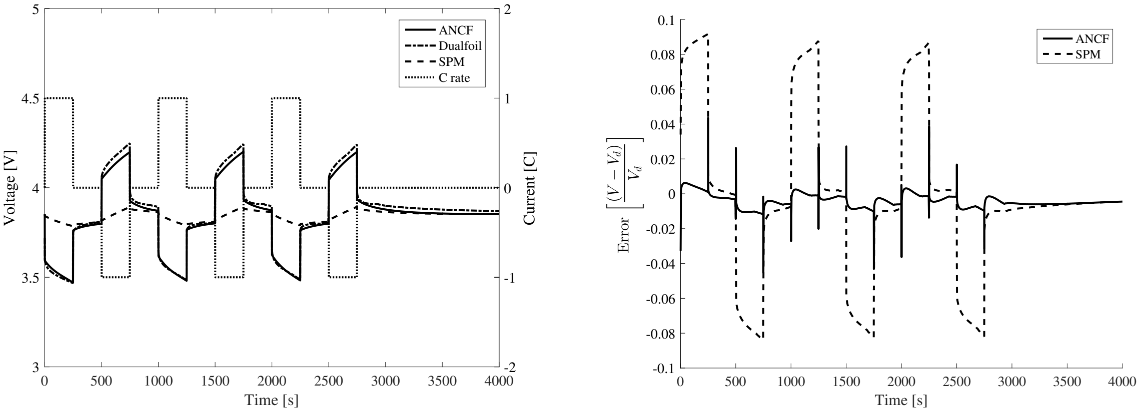

Figure 3-12: Simulation results on the left for the ANCF II model, SPM model, and DualFoil, at 1C for 4000 seconds. Error results are shown to the right, normalized against the Dualfoil results.

.

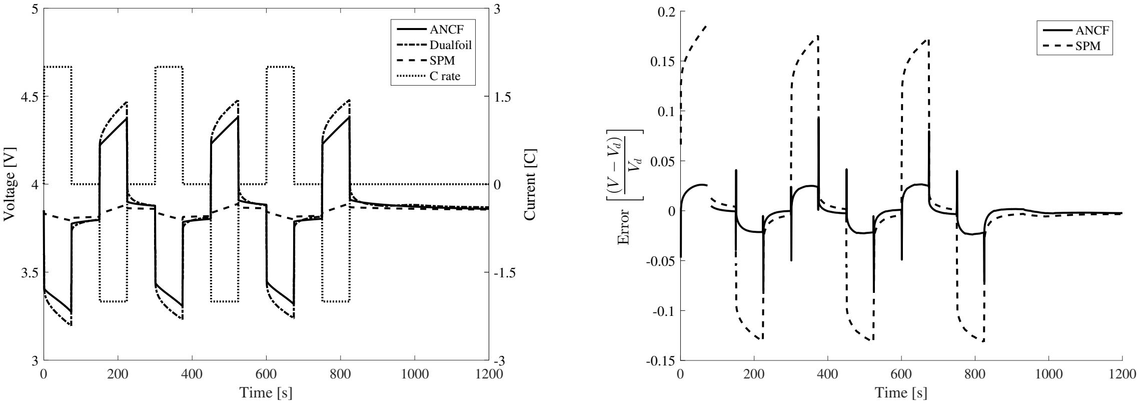

Figure 3-13: Simulation results on the left for the ANCF II model, SPM model, and DualFoil, at 2C for 1200 seconds. Error results are shown to the right, normalized against the Dualfoil results.

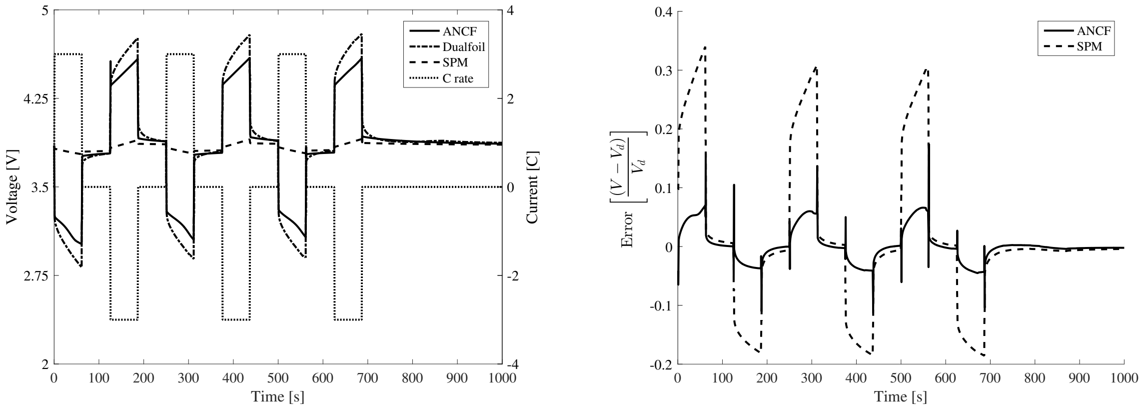

Figure 3-14: Simulation results on the left for the ANCF II model, SPM model, and DualFoil, at 3C for 1000 seconds. Error results are shown to the right, normalized against the Dualfoil results.

.

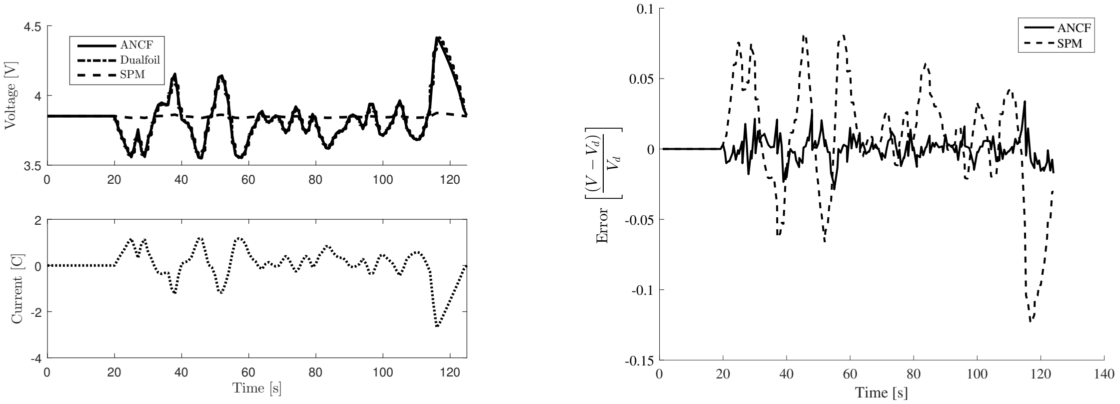

Figure 3-15: Simulation results on the left for the ANCF II model, SPM model, and DualFoil, for a subset of the UDDS profile. Error results are shown to the right, normalized against the Dualfoil results.

3.6.3 Model Comparison

Table 3.2: Comparative summary of normalized error for simulation results of the ANCF model.

C - Rate	**ANCF Error** ($\times 10^2$)		**SPM Error** ($\times 10^2$)		$\boldsymbol{\Delta E}(\times 10^2)$	
	RMS	Max	RMS	Max	RMS	Max
0.1	3.2842	5.0386	2.4548	3.9937	0.8294	1.0449
1.0	1.1574	8.9171	6.4868	9.0207	-5.3294	-0.1036
2.0	1.5781	15.1420	9.4397	17.0540	-7.8616	-1.9120
3.0	2.3768	21.0590	12.9130	25.9120	-10.5362	-4.8530

Table 3.3: Comparative summary of normalized error for simulation results of the ANCF II model.

C - Rate	**ANCF II Error** ($\times 10^2$)		**SPM Error** ($\times 10^2$)		$\boldsymbol{\Delta E}(\times 10^2)$	
	RMS	Max	RMS	Max	RMS	Max
0.1	2.3638	10.3581	2.7109	17.5064	-0.34714	-7.1483
1.0	0.6709	4.3581	4.8207	9.1706	-4.1498	-4.8125
2.0	1.5262	9.2496	8.6985	18.6971	-7.1723	-9.4475
3.0	2.9854	17.3983	13.4142	33.9896	-10.4287	-16.5913

It was anticipated that because of the fewer degrees of freedom of the ANCF II, its performance relative to the ANCF model would be hindered at more severe discharge rates. It is apparent from a comparison of Tables 3.2 and 3.3 that the ANCF and ANCF II models outperform the SPM in nearly all cases. At low discharge, namely 0.1C, the ANCF II is better than the ANCF model, seen in Figures 3-6 and 3-11, with a difference in RMS error of 9.2 mV. The ANCF II actually continues to outperform the ANCF model at moderate to high discharge rates, specifically at 1C, as seen in Figures 3-7 and 3-12, with a difference in RMS error of 4.9 mV; and 2C, as seen in Figures 3-8 and 3-13, with a difference in RMS error of 0.52 mV. The anticipated performance degradation is witnessed at the highest discharge rate simulated, 3C, shown in Figures 3-9 and 3-14, but the ANCF model only performs marginally better than the ANCF II model, with an RMS error 6.1 mV better, but a higher maximum error, which is consistent throughout the simulations, with the exception of the results of the 0.1C discharge profile.

The ANCF II performs with consistent, and frequently better results, than the ANCF, but reduces the total number of states significantly. More importantly, the algebraic constraint is reduced, which allows for a more tractable problem in Section 4.3.2. This is critically important, as the error injected through the unknown inputs of the model will distort the results of the full-scale observer. This will be discussed more in Chapter 4. The benefit of fewer states and constraints, while maintaining model performance, allows for the adaptive observers discussed in Chapter 4 to be built around the ANCF II model.

Chapter 4

Adaptive Observers

The adaptive observer is a well established concept in literature, developed over decades of research [10] [29] [37], with a wide variety of system identification applications. The purpose is to be able to identify both the states and parameters of a system, using a non-minimal representation. There are several instances of this technique, but the focus will be limited to a handful of techniques and novel utilizations relevant to this field.

Section 4.1 describes the vector-regressor adaptive observer, as presented in literature [37]. This is the basic form of the adaptive observer, and the results of its application will be built on in further sections. By establishing the concepts of the vector-regressor form, the techniques can be adjusted and applied to more advanced and stable iterations of the adaptive observer. Section 4.2 discusses one such attempt at making a more stable, reliable adaptive observer, using a matrix regressor instead of the aforementioned vector. Conventionally, this is achieved by filtering the input and output of the system, and relying on the the linear nature of the observed system to create a faster, more stable converging observer to the real parameters.

Finally, Section 4.3 discusses the process of applying these observers, in various novel forms, to the ANCF II model presented in Chapter 3. This includes a spatio-temporal version of the matrix regressor adaptive observer, for purposes of observing the solid electrode systems; a matrix regressor adaptive observer using multiple filters with cascading poles, for purposes of estimating the molar flux; and a novel nonlinear update law for the purposes of estimating the electrolyte system. These observers create the initial foundation for a full-scale observer using the ANCF II, and the process and limitations of full-scale implementation will be discussed in Section 4.4.

4.1 Vector-Regressor Adaptive Observers

This section will discuss the establishment of a vector-regressor adaptive observer, as presented in literature [37]. Its purpose is to estimate both the states and parameters that define a system, using measurable inputs and outputs. This is achieved by creating an equivalent, non-minimal system, and using an update law that ensures stability, in a Lyapunov sense. Then with sufficient persistent excitation, the system will converge to the real states and parameters. The convergence of these parameters is non-trivial, however, as the observer may take the form of an equivalent system that is able to generally replicate the frequency response of the system for a certain bandwidth, but may not be an accurate result.

Additionally, there are several forms of the adaptive observer, but this section will focus exclusively on the non-minimal representation which fully defines the poles and zeros of the transfer function. It is not possible to distinguish between the input coefficients and the output coefficients, but only their manifestation in the transfer function as transmission zeros. Subsequently, the parameters of the system matrix manifest in both the zeros and poles, but the poles of the system are exclusively a function of those system parameters. This knowledge is leveraged in several ways in subsequent sections.

4.1.1 Equivalent System

To begin, a generalized single input, single output (SISO) state-space system is defined,

$$\begin{aligned} \dot{x} &= Ax(t) + Bu(t) \\ y(t) &= C^\top x(t) \end{aligned} \tag{4.1}$$

for which a transfer function can also be defined,

$$\begin{aligned} G_p(s) = \frac{Y(s)}{U(s)} &= C^\top (s\mathrm{I} - A)^{-1} B \\ &= \frac{b_1 s^{k-1} + \ldots + b_k}{s^k + a_1 s^{k-1} + \ldots + a_k} \end{aligned} \tag{4.2}$$

The purpose then is to take an arbitrary observer system, and match the frequency response to the results of the system in question. The equivalent system is defined as,

$$\begin{aligned} \dot{\omega}_u &= F\omega_u + gu(t) \\ \dot{\omega}_y &= F\omega_y + gy(t) \end{aligned} \tag{4.3}$$

where the output of the equivalent system is defined as,

$$y(t) = \theta_u^\top \omega_u + \theta_y^\top \omega_y \tag{4.4}$$

Equation (4.4) can be succinctly defined as,

$$y(t) = \theta^\top \omega \tag{4.5}$$

where,

$$\theta = \begin{bmatrix} \theta_u \\ \theta_y \end{bmatrix} \tag{4.6}$$

and,

$$\omega = \begin{bmatrix} \omega_u \\ \omega_y \end{bmatrix} \tag{4.7}$$

The full equivalent system can be defined in the frequency domain as,

$$\begin{aligned} Y(s) &= \theta_u^\top \Omega_u(s) + \theta_y^\top \Omega_y(s) \\ Y(s) &= G_u(s)U(s) + G_y(s) + Y(s) \\ \frac{Y(s)}{U(s)} &= \frac{G_u(s)}{1 - G_y(s)} \end{aligned} \tag{4.8}$$

If the regressor filter is defined in observer-canonical representation, where,

$$F = \begin{bmatrix} 0 & 1 & \dots & 0 \\ \vdots & \vdots & \ddots & \vdots \\ 0 & 0 & \dots & 1 \\ -a_{f,k} & -a_{f,k-1} & \dots & -a_{f,1} \end{bmatrix} \tag{4.9}$$

$$g = \begin{bmatrix} 0 & \cdots & 0 & 1 \end{bmatrix}^\top \tag{4.10}$$

it can be shown that the full equivalent system transfer function is defined as,

$$\frac{Y(s)}{U(s)} = \frac{b_{u,1}s^{k-1} + \ldots + b_{u,k}}{s^k + (a_{f,1} - b_{y,1})s^{k-1} + \ldots + (a_{f,k} - b_{y,k})} \tag{4.11}$$

where,

$$\begin{aligned} \theta_u &= \begin{bmatrix} b_{u,k} & \dots & b_{u,1} \end{bmatrix}^\top \\ \theta_y &= \begin{bmatrix} b_{y,k} & \dots & b_{y,1} \end{bmatrix}^\top \end{aligned} \tag{4.12}$$

Subsequently, an estimated system is defined as,

$$\begin{aligned} \dot{\hat{\omega}}_u &= F\hat{\omega}_u + gu(t) \\ \dot{\hat{\omega}}_y &= F\hat{\omega}_y + gy(t) \end{aligned} \tag{4.13}$$

and an output,

$$\hat{y}(t) = \hat{\theta}^\top \hat{\omega} \tag{4.14}$$

The error in the regressor, or sensitivity error, is defined as,

$$\tilde{\omega} = \hat{\omega} - \omega \tag{4.15}$$

The time derivative of the sensitivity error can be evaluated by subtracting Equation

(4.13) from Equation (4.3), yielding,

$$\dot{\tilde{w}} = \bar{F}\tilde{\omega} \tag{4.16}$$

where,

$$\bar{F} = \begin{bmatrix} F & 0 \\ 0 & F \end{bmatrix} \tag{4.17}$$

Therefore, if F is any negative definite matrix, then $\tilde{w} \to 0$ and $\hat{\omega} \to \omega$, as $t \to \infty$. Once the sensitivity error goes to zero, the system need only to replicate the parameters, θ, to match the original system, such that $\hat{\theta} \to \theta$ and $\hat{y}(t) \to y(t)$. This motivates the update laws described in Section 4.1.2. Figure 4-1 shows the observer in parallel with the original system, $G_p(s)$, with estimated equivalent systems, $G_u(s)$ and $G_y(s)$.

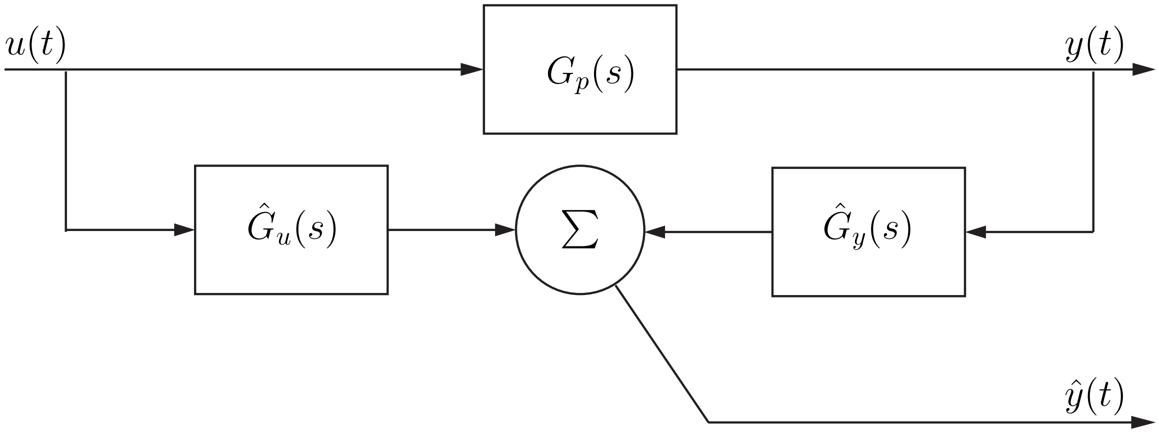

Figure 4-1: Block diagram of the adaptive observer. By updating the parameters of $\hat{G}_u(s)$ and $\hat{G}_y(s)$, the frequency response of the original system can be replicated.

4.1.2 Update Laws

An update law must be defined to ensure stability of the observer, in a Lyapunov sense. A candidate Lyapunov function can be defined as,

$$V = \frac{1}{2}\tilde{\theta}^{\top}\tilde{\theta} \tag{4.18}$$

where,

$$\tilde{\theta} = \hat{\theta} - \theta \tag{4.19}$$

Equation (4.18) is positive semi-definite, as it resembles the description of the kinetic energy of a mechanical system. The goal, then, is to ensure its time derivate is negative semi-definite, and stability will be ensured. The time derivative of Equation (4.18) is defined as,

$$\begin{aligned} \dot{V} &= \frac{1}{2}\left(\dot{\tilde{\theta}}^{\top}\tilde{\theta} + \tilde{\theta}^{\top}\dot{\tilde{\theta}}\right) \\ &= \tilde{\theta}^{\top}\dot{\tilde{\theta}} \\ &= \tilde{\theta}^{\top}\left(\dot{\hat{\theta}} - \dot{\theta}\right) \\ &= \tilde{\theta}^{\top}\dot{\hat{\theta}} \end{aligned} \tag{4.20}$$

where θ is the statically defined parameters of the equivalent system, and as such, $\dot{\theta} = 0$. As it is not explicitly possible to define the error in the parameters, $\tilde{\theta}$, an adaptive law for parameter learning, $\dot{\hat{\theta}}$, must be devised to ensure sign definiteness in Equation (4.20). One proposed solution [37] is to use the update law as shown in Equation (4.21).

$$\begin{aligned} &\dot{\hat{\theta}} = -\Gamma\hat{\omega}e \\ &\Gamma > 0 \end{aligned} \tag{4.21}$$

where the error, e, is defined as,

$$e = \hat{y}(t) - y(t) \tag{4.22}$$

If it is assumed, as shown in Equation (4.16), that $\tilde{\omega} \to 0$, then the Lyapunov candidate in Equation (4.20) reduces to,

$$\dot{V} = -\left(\tilde{\theta}^{\top}\hat{\omega}\right)^{2} \tag{4.23}$$

It should be noted that Equation (4.23) is negative semi-definite, which ensures stability. However, this does not guarantee that $\hat{\theta} \to \theta$. Only under persistent excitation is this goal achieved.

4.2 Matrix-Regressor Adaptive Observers

It has been shown that the vector-regressor adaptive observer is successful in parameter identification under persistent excitation as $t \to \infty$. However, these are difficult conditions to ensure, and an observer with faster convergence in a more diverse input regime is desired. To this end, the matrix-regressor adaptive observer has been proposed in literature [27] [26] [24]. The concept, generally speaking, is to increase the density of the regressor information by constructing a full-rank regressor matrix, called a regressor bank, that uses the same linear parameters to produce an output as the vector-regressor adaptive observer.

By ensuring the regressors are full-rank, but maintain the same relationship to the parameter set, faster convergence can be observed [24]. As will be shown in Section 4.3.1, there are novel options for ways to create a full rank matrix, while also reducing the need for additional filtration elements.

4.2.1 Regressor Bank

Again, an equivalent system, similar to Equation (4.3) is constructed such that,

$$\begin{aligned} \dot{\omega}_{u,0} &= F\omega_{u,0} + gu_0(t) \\ \dot{\omega}_{y,0} &= F\omega_{y,0} + gy_0(t) \\ y_0(t) &= \theta^\top \omega_0 \end{aligned} \tag{4.24}$$

where,

$$\omega_0 = \begin{bmatrix} \omega_{u,0} \\ \omega_{y,0} \end{bmatrix} \tag{4.25}$$

The construction of the matrix-regressor adaptive observer is fundamentally based on identifying linearly independent regressors that can define a measurable output. A convenient way is to use a first order filter, but the designer is not limited on this basis. Under this conventional premise, a filtered input can be defined, such that,

$$u_1(t) = G(s)u_0(t) \tag{4.26}$$

and a filtered output,

$$y_1(t) = G(s)y_0(t) \tag{4.27}$$

The applied filter $G(s)$ is any arbitrary stable filter, but for simplicity, is defined as a first order filter,

$$G(s) = \frac{\beta}{s+\beta} \tag{4.28}$$

Using Equations (4.26) and (4.27), a filtered equivalent system is defined as,

$$\begin{aligned} \dot{\omega}_{u,1} &= F\omega_{u,1} + gu_1(t) \\ \dot{\omega}_{y,1} &= F\omega_{y,1} + gy_1(t) \\ y_1(t) &= \theta^\top \omega_1 \end{aligned} \tag{4.29}$$

By superposition, a filtered regressor can be defined as,

$$\omega_1 = G(s)\omega_0 \tag{4.30}$$

Subsequently, by iterating on multiple inputs and outputs, any arbitrary number of filtered regressors can be defined with a focus on specific frequency content, such that,

$$\omega_i = G^i(s)\omega_{i-1} \tag{4.31}$$

for $\omega_i \in \mathbb{R}^n$. These filters are linearly independent, and therefore each of the resulting regressors, ω_i, are linearly independent, as well. Figure 4-2 shows the frequency response of these filters, and it should be noted that the crossover frequency remains the same for each, but the attenuation grows as the order of the filter increases.

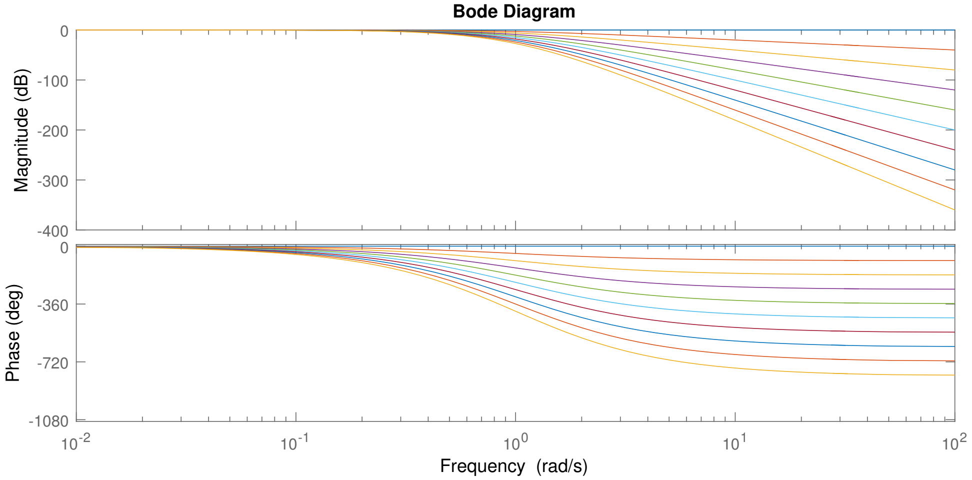

Figure 4-2: Frequency response of the iterative filters for $\beta = 1$, $n = 10$.

Then by using the filtered regressors in Equation (4.31), a full-rank matrix can be defined as a regressor bank, Ω, such that,

$$\Omega = \begin{bmatrix} \omega_0 & \cdots & \omega_{n-1} \end{bmatrix} \tag{4.32}$$

where a matrix-regressor output would take the form,

$$\begin{aligned} Y &= \Omega^\top \theta \\ Y &= \begin{bmatrix} y_0(t) & \cdots & y_{n-1}(t) \end{bmatrix}^\top \end{aligned} \tag{4.33}$$

Generally, any set of linearly independent regressors that satisfy the relationship of Equation (4.33) can be chosen to construct the regressor bank, Ω, as shown in Equation (4.32), and need not be restricted by Equation (4.31). Subsequently, the estimated system is defined similarly to Equation (4.32), such that,

$$\widehat{\Omega} = \begin{bmatrix} \hat{\omega}_0 & \cdots & \hat{\omega}_{n-1} \end{bmatrix} \tag{4.34}$$

where an equivalent output vector can be defined as,

$$\widehat{Y} = \widehat{\Omega}^{\top} \hat{\theta} \tag{4.35}$$

Using a formation similar to Equation (4.21), an update law is devised, such that,

$$\dot{\hat{\theta}} = -\Gamma \widehat{\Omega} E \tag{4.36}$$

where the error, E, is defined as,

$$E = \widehat{Y} - Y \tag{4.37}$$

It has been shown that this implementation of an adaptive observer exhibits rapid convergence [24], faster than the vector-regressor form described in Section 4.1.

4.2.2 Filter Transformations

One of the nebulous elements of designing adaptive observers is the specific form that the filter, F, and input vector, g, take in the regressor dynamics of Equation (4.24). Work in establishing design laws has been a focus of literature [23] [24], and will be established in the section for clarity in the design of observers found later. Notionally, an observer designer will have some a-priori knowledge of the system, namely in the order of magnitude of the poles and zeros. Additionally, it has been noted that the convergence of parameters to their true values is improved when the parameters are all of the same order, such that the error in one is not offset in the output of the estimated system by the minimal error of a larger parameter. It is observed that the parameter of larger magnitude will oscillate about its true value, in an effort to correct the error in the output, while the parameter of smaller value will essentially be neglected because of its reduced role in the output dynamics. Frankly speaking, this does not matter if the purpose of the observer is to produce the same results as a measured system, but in the interest of accurately measuring parameters, this effect matters greatly. Therefore, in the interest of alleviating this effect, a strategy for designing the filter system will be established.

Again, an equivalent system is defined as in Equation (4.24), such that,

$$\begin{aligned}\dot{\omega}_{u,0} &= F_0\omega_{u,0} + g_0u_0(t)\\ \dot{\omega}_{y,0} &= F_0\omega_{y,0} + g_0y_0(t)\\ y_0(t) &= \theta_0^\top\omega_0\end{aligned} \tag{4.38}$$

where the filter, F_0, is a stable, negative definite matrix, and Equation (4.38) is equivalent to the full system,

$$\begin{aligned}\dot{x} &= Ax + Bu(t)\\ y(t) &= C^\top x\end{aligned} \tag{4.39}$$

Additionally, in Equation (4.38), the untransformed parameters, θ_0, are defined as,

$$\theta_0 = \begin{bmatrix} \theta_{u,0} \\ \theta_{y,0} \end{bmatrix} \tag{4.40}$$

In the interest of simplicity, the system shown in Equation (4.39) is defined in observable canonical form [17], such that,

$$A = \begin{bmatrix} -a_1 & 1 & 0 & \dots & 0 \\ -a_2 & 0 & 1 & \dots & 0 \\ \vdots & \vdots & \vdots & \ddots & \vdots \\ -a_{k-1} & 0 & 0 & \dots & 1 \\ -a_k & 0 & 0 & \dots & 0 \end{bmatrix} \tag{4.41}$$

$$B = \begin{bmatrix} b_1 & \cdots & b_k \end{bmatrix}^\top \tag{4.42}$$

$$C = \begin{bmatrix} 1 & \cdots & 0 \end{bmatrix}^\top \tag{4.43}$$

The notional plant, as mentioned above, is defined similarly in observable canonical form, such that,

$$\widehat{A} = \begin{bmatrix} -\hat{a}_1 & 1 & \dots & 0 \\ \vdots & \vdots & \ddots & \vdots \\ -\hat{a}_{k-1} & 0 & \dots & 1 \\ -\hat{a}_k & 0 & \dots & 0 \end{bmatrix} \tag{4.44}$$

$$\widehat{B} = \begin{bmatrix} \hat{b}_1 & \cdots & \hat{b}_k \end{bmatrix}^\top \tag{4.45}$$

$$C = \begin{bmatrix} 1 & \cdots & 0 \end{bmatrix}^\top \tag{4.46}$$

Therefore, the designer can remove the arbitrary task of picking the poles of the regressor filter, F_0, by locating the poles initially at the notional poles of the system, such that,

$$F_0 = \begin{bmatrix} 0 & 1 & \dots & 0 \\ \vdots & \vdots & \ddots & \vdots \\ 0 & 0 & \dots & 1 \\ -a_{f,k} & -a_{f,k-1} & \dots & -a_{f,1} \end{bmatrix} \tag{4.47}$$

$$g_0 = \begin{bmatrix} 0 & \cdots & 1 \end{bmatrix}^\top \tag{4.48}$$

and the poles of the filter, F_0, are defined as,

$$a_{f,i} = \hat{a}_i \tag{4.49}$$

It is important to note that the filter, F_0, must be a negative definite matrix, so any unstable or marginally stable pole, $\hat{a}_i \leq 0$, must be replaced with a small value, such as $a_{f,i} = \epsilon$, where $\epsilon = 1e - 3$, for example.

Using this initial step of the formulation, a Kalman filter gain is designed to reject the erroneous frequency content of the regressors. The process follows the basic Kalman filter design [17], and will be outlined bellow. The Kalman filter design proceeds as a general system,

$$\begin{aligned}\dot{x} &= Ax + Bu + Gw \\ y &= Cx + Du + Hw + v\end{aligned} \tag{4.50}$$

where w and v are noise introduced into the system from input and output measurements. These values are defined such that,

$$\begin{aligned}E[w] = E[v] &= 0 \\ E[ww^\top] &= Q \\ E[vv^\top] &= R \\ E[wv^\top] &= N\end{aligned} \tag{4.51}$$

where $E[\cdot]$ is the expected value function, and Q, R and N are the arbitrary values of that function. For the purposes of the design of the filter, F_0, a ratio of these values is defined as,

$$\sigma = \frac{Q}{R} \tag{4.52}$$

where the designer has a choice of this ratio, with a higher σ rejecting more error. Then, a covariance matrix of the error, P, is defined such that,

$$P = \lim_{t\to\infty} E\left[\{x - \hat{x}\}\{x - \hat{x}\}^\top\right] \tag{4.53}$$

and a Kalman gain, L, is defined as the solution to an algebraic Riccati equation at steady-state,

$$L = (PC^\top + \bar{N})\bar{R}^{-1} \tag{4.54}$$

where,

$$\bar{R} = R + HN + N^\top H^\top + HQH^\top \tag{4.55}$$

$$\bar{N} = G\left(QH^\top + N\right) \tag{4.56}$$

for $H = 0$ and $G = 0$. Using the gain vector, L, the filter, F_0, can be altered by,

$$F_0 = \left(\widehat{A} - LC^\top\right)^\top \tag{4.57}$$

where the input vector, g_0, remains unaltered,

$$g_0 = \begin{bmatrix} 1 & \cdots & 0 \end{bmatrix}^\top \tag{4.58}$$

The next step is to normalize the filters to scale the signals, using a steady-state Riccati equation to define a scaling matrix, P_0, such that,

$$F_0 P_0 + P_0 F_0^\top + g_0 g_0^\top = 0 \tag{4.59}$$

where F_0 is as defined in Equation (4.57) and g_0 is as defined in Equation (4.58). P_0 is a full-rank matrix that can be decomposed into its eigenvalues, D, and eigenvectors, V, such that,

$$P_0 = VDV^\top \tag{4.60}$$

An input transformation matrix, T_u, is then defined as,

$$T_u = D^{-\frac{1}{2}} V \tag{4.61}$$

Subsequently, an additional scaling matrix, P_p, is defined using the steady-state Riccati equation,

$$0 = \widehat{A} P_p + P_p \widehat{A}^\top + \widehat{B}\widehat{B}^\top \tag{4.62}$$

Using P_p, a scalar scaling factor, p, is defined as,

$$p = \frac{1}{\sqrt{C^\top P_p C}} \tag{4.63}$$

This scaling factor is then applied to the input transformation matrix, T_u, to create an output transformation matrix, T_y, such that,

$$T_y = pT_u \tag{4.64}$$

Finally, these transformations are applied to the filters and input vectors for the purposes of normalization,

$$F_u = F_y = T_u F_0 T_u^{-1} \tag{4.65}$$

$$g_u = T_u g_0 \tag{4.66}$$

$$g_y = T_y g_0 \tag{4.67}$$

The filters, F_u and F_y maintain negative definiteness, while also retaining the same poles, which eases the final calculation of the system parameters. However, the input vectors, g_u and g_y, are normalized such that the zeros are of the same scale. The final adaptive observer system is defined as,

$$\begin{aligned} \dot{\omega}_{u,i} &= F_u \omega_{u,i} + g_u u_i(t) \\ \dot{\omega}_{y,i} &= F_y \omega_{y,i} + g_y y_i(t) \\ y_i(t) &= \theta^\top \omega_i \end{aligned} \tag{4.68}$$

The transformed parameters, θ, are defined as,

$$\theta = \begin{bmatrix} T_u^{-\top} \theta_{u,0} \\ T_y^{-\top} \theta_{y,0} \end{bmatrix} \tag{4.69}$$

where $\theta_{u,0}$ and $\theta_{y,0}$ are defined as shown in Equation (4.40), for use in Equation (4.38). The same matrix regressor form, shown in Equations (4.32) and (4.33), is still applicable, with an update law as defined by Equation (4.36) in the estimated system.

4.3 Adaptive Observers for the ANCF II

The adaptive observers established in Sections 4.1 and 4.2 are now applied to the ANCF II model as discussed in Chapter 3. It will be important to consider how the adaptive observers can be altered to leverage the a-priori knowledge of the numerical structure, but not the specific values of model parameters, to boost their speed of learning. Figure 4-3 shows the model depicted in a novel block diagram formation. The majority of parameters, relating to the SoH, and states, relating to the SoC, are located in the concentration dynamics, $G_p(s)$, which also lends itself to the linear structure of the observers described above. Therefore, to construct observers for these dynamics is the key foundational beginning of an ABMS. The challenge is to make these observers stable and rapidly converging, such that minimal error propagates into the nonlinear portions of the model. To this end, the observers in this thesis will make assumptions about the measurable inputs and outputs, as described in Sections 4.3.1 – 4.3.3. Specifically, the observers will be designed around the solid dynamics, $\bar{\boldsymbol{c}}_s^*(t)$ and $\boldsymbol{q}^*(t)$; the electrolyte dynamics, $\boldsymbol{c}_e(t)$; and make a prediction for the molar flux, $\boldsymbol{j}^*(t)$, using novel contributions to the adaptive observers utilizing spatial consistency among parameters. Figure 4-4 shows the reduced block diagram that will constitute the focus of this exploration.

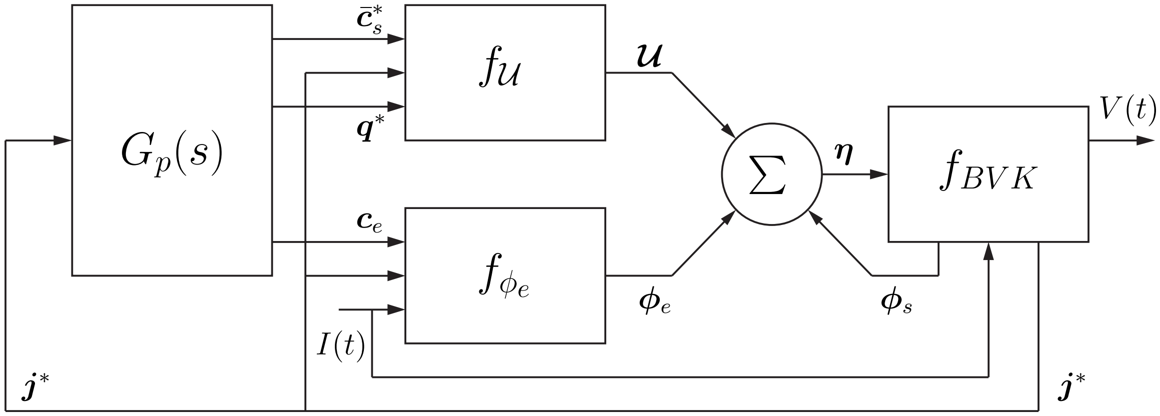

Figure 4-3: Block diagram of the ANCF II model, showing areas for practical application of the adaptive observers with respect to the concentration dynamics, $G_p(s)$.

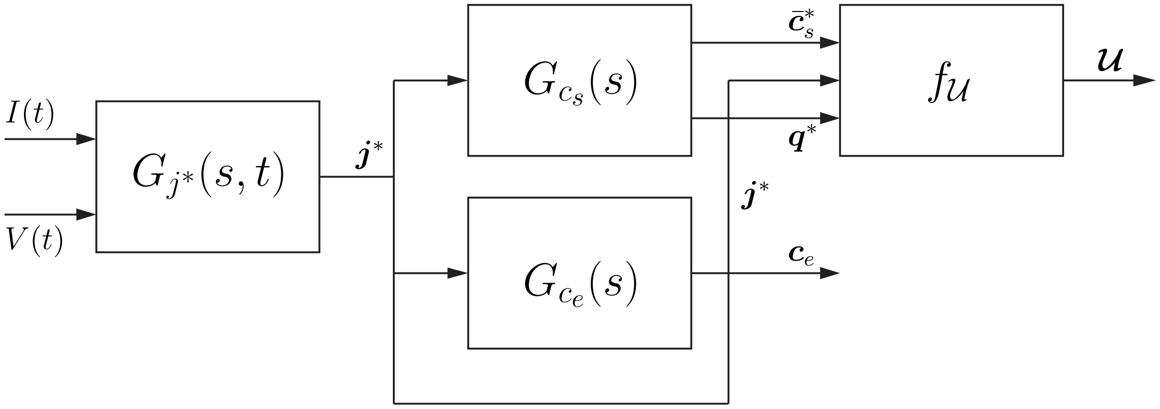

Figure 4-4: Block diagram of the ANCF II subsystem, expanding $G_p(s)$ to two separate linear systems, and a predictive element to the molar flux, $\boldsymbol{j}^*$, using measurable inputs and outputs, $I(t)$ and $V(t)$.

4.3.1 Solid Observer

The first observer to be constructed is for the solid dynamics, as shown in Equations (3.118) – (3.120), and manifested in the system shown in Equation (3.121). To construct this observer, it is assumed that the open-circuit potential is fully measurable and invertible to the surface concentration, $c^*_{ss,i}$ for all nodes. Therefore, the notional plant is a SISO plant with direct feed-through, such that,

$$\begin{aligned} \dot{x}_i &= A_p x_i + B j_i^* \\ c^*_{ss,i} &= C^\top x_i + D j_i^* \end{aligned} \tag{4.70}$$

where the states are defined as,

$$x_i = \begin{bmatrix} \bar{c}^*_{s,i} \\ q_i^* \end{bmatrix} \tag{4.71}$$

This plant can then be put into observable canonical form, from its original form in Equations (3.122) – (3.125), such that,

$$A_p = \begin{bmatrix} -a_1 & 1 \\ -a_2 & 0 \end{bmatrix} \tag{4.72}$$

$$B = \begin{bmatrix} -b_1 - a_1 b_0 \\ -b_2 - a_2 b_0 \end{bmatrix} \tag{4.73}$$

$$C = \begin{bmatrix} 1 & 0 \end{bmatrix}^\top \tag{4.74}$$

$$D = b_0 \tag{4.75}$$

The transfer function for this system, $G_p(s)$, is defined as,

$$G_p(s) = C^\top \left(s\mathrm{I} - A\right)^{-1} B + D \tag{4.76}$$

expressed in the frequency domain as,

$$\begin{aligned} G_p(s) &= \frac{b_0 s^2 + b_1 s + b_2}{s^2 + a_1 s + a_2} \\ G_p(s) &= \frac{\left(\frac{-R_{p,i}}{35 D_{s,i}}\right) s^2 + \left(\frac{-315}{35 R_{p,i}}\right) s + \left(\frac{-3150 D_{s,i}}{35 (R_{p,i})^3}\right)}{s^2 + \left(\frac{1050 D_{s,i}}{35 (R_{p,i})^2}\right) s + 0} \end{aligned} \tag{4.77}$$

As is evident, the second pole is marginally stable, $a_2 = 0$. Therefore, to construct the filters, as described in Section 4.2.2, this pole is replaced with a stable pole for the filter design, $a_2 = 0.001$. As such, an equivalent system can be made as,

$$\begin{aligned} \dot{\omega}_{0,u,i} &= F_u \omega_{0,u,i} + g_u K j_i^* \\ \dot{\omega}_{0,y,i} &= F_y \omega_{0,y,i} + g_y c_{ss,i}^* \end{aligned} \tag{4.78}$$

where the input, j_i^*, is multiplied by a gain, K, to reduce the magnitude of numerator coefficients in the transfer function. Additionally, the subscript, i, denotes the plant for a node, i. It is noted that each filter in a volume, $(\pm)$, is the same, and, as such, the plants for each node are the same, with varying states. Therefore, the regressor bank, as described in Equation (4.32), will be constructed to leverage this by incorporating both temporal filters, as presented in the base construction, and a novel use of spatial filters, using the known model structure to its advantage.

A full equivalent system is constructed, such that the dynamics of the filtered signals are then defined as,

$$\begin{aligned}\dot{\omega}^{\pm}_{0,u,i} &= F^{\pm}_{u}\omega^{\pm}_{0,u,i} + g_u K j^*_i \\ \dot{\omega}^{\pm}_{0,y,i} &= F^{\pm}_{y}\omega^{\pm}_{0,y,i} + g_y \frac{c^{*\pm}_{ss,i}}{c^{*\pm}_{s,max}}\end{aligned} \tag{4.79}$$

where the known gain, K, is applied to the input, and the output is normalized against the maximum concentration value, $c^{*\pm}_{s,max}$. These values do not change the system dynamics, but only alter the gain of the transfer function. The full system regressor vector is concatenated as,

$$\omega^{\pm}_{0,i} = \left[\begin{array}{ccc} \omega^{\pm}_{0,u,i} & \omega^{\pm}_{0,y,i} & K j^*_i \end{array}\right]^{\top} \tag{4.80}$$

This vectors contains the input regressor, $\omega^{\pm}_{0,u,i}$; the output regressor, $\omega^{\pm}_{0,y,i}$; and the gain adjusted input, $K j^*_i$, for each node, i. The filters are then applied to the full regressor, $\omega^{\pm}_{0,i}$, such that,

$$\omega^{\pm}_{1,i} = G_f(s)\omega^{\pm}_{0,i} \tag{4.81}$$

where the filter, $G_f(s)$, is defined as,

$$G_f(s) = \frac{\beta}{s+\beta} \tag{4.82}$$

Next, a full matrix of regressors is constructed, similarly to Equation (4.32), but instead of a completely temporal filter application, this matrix is generated by inputing the full number of nodal regressors. For each node, i, the nodal regressor, $\omega^{\pm}_{0,i}$, is inserted, and supplemented with temporal filters to create a full-rank matrix, such that,

$$\Omega_{\pm} = \left[\begin{array}{cccccc} \omega^{\pm}_{0,1} & \dots & \omega^{\pm}_{0,N^{\pm}} & \omega^{\pm}_{1,1} & \dots & \omega^{\pm}_{1,N^{\pm}} \end{array}\right] \tag{4.83}$$

The spatial regressor, $\omega^{\pm}_{0,i}$, for each volume, ($\pm$), is filtered as shown in Equation (4.81). For $N_{\pm} = 3$, only one filtration is necessary per node to ensure the regressor bank, $\Omega_\pm$, is full-rank. The output of the system is then defined as,

$$Y_\pm = \Omega_\pm^\top \theta_\pm \tag{4.84}$$

where $\theta_\pm$ are the non-minimal parameters of the transfer function, and the output, $Y_\pm$, is defined as,

$$Y_\pm = \frac{1}{c_{s,max}^\pm} \begin{bmatrix} c_{ss,1}^* & \cdots & c_{ss,N_\pm}^* & G_f(s)c_{ss,1}^* & \cdots & G_f(s)c_{ss,N_\pm}^* \end{bmatrix}^\top \tag{4.85}$$

Figure 4-5 shows the subsystem that is the focus of Section 4.3.1, and assuming an invertible open-circuit potential function, $f_{\mathcal{U}}^{-1}$, enabling a calculation of the surface concentration, $\frac{\boldsymbol{c}_{ss}^*}{c_{s,max}^\pm}$.

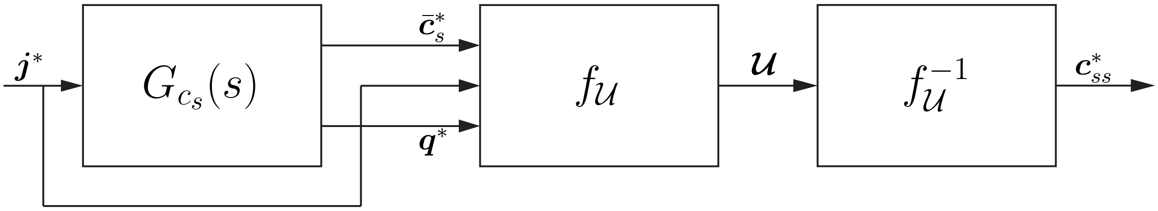

Figure 4-5: Block diagram of the solid electrode subsystem, assuming measurable inputs and outputs.

To generate the observer, an estimated system is then defined, with a regressor bank as shown in Equation (4.83), such that,

$$\widehat{Y}_\pm = \widehat{\Omega}_\pm^\top \hat{\theta}_\pm \tag{4.86}$$

The error of the estimated output, E, is then defined as

$$E_\pm = \widehat{Y}_\pm - Y_\pm \tag{4.87}$$

where it is assumed that the true output, Y, is directly measurable and capable of being filtered. An update law for the parameters, $\hat{\theta}^\pm$, is defined as,

$$\dot{\hat{\theta}}_\pm = -\Gamma \widehat{\Omega}_\pm E_\pm \tag{4.88}$$

where the gain matrix, Γ, is defined as,

$$\Gamma = \begin{bmatrix} \gamma_1 & 0 & \cdots & 0 \\ 0 & \gamma_2 & \cdots & 0 \\ \vdots & \vdots & \ddots & \vdots \\ 0 & 0 & \cdots & \gamma_{N_\pm} \end{bmatrix} \tag{4.89}$$

such that $\gamma_i > 0$. To calculate the true parameters, a similar approach is taken as shown in Section 4.2.2, such that a filter is defined as,

$$F_0 = \left(\widehat{A} - LC^\top\right)^\top = \begin{bmatrix} 0 & 1 \\ -a_{f,2} & -a_{f,1} \end{bmatrix} \tag{4.90}$$

where $\widehat{A}$ is the notional parameters of the plant. The real parameters, A, are defined as,

$$A = \begin{bmatrix} -a_2 & 1 \\ -a_1 & 0 \end{bmatrix} \tag{4.91}$$

The output, $c_{ss,i}(t)$, for each node, i, is defined as,

$$c_{ss,i}(t) = \theta_{u,0}^\top \omega_{i,u} + \theta_{y,0}^\top \omega_{i,y} + \delta j_i^*(t) \tag{4.92}$$

Subsequently, the true parameters of the output regressor, $\theta_{y,0}$, are defined as,

$$\theta_{y,0} = \begin{bmatrix} a_{f,2} - a_2 \\ a_{f,1} - a_1 \end{bmatrix} \tag{4.93}$$

Using the result of this evaluation, the true parameters of the input regressor, $\theta_{u,0}$, are defined as,

$$\theta_{u,0} = \begin{bmatrix} b_2 - b_0 a_2 \\ b_1 - b_0 a_1 \end{bmatrix} - b_0 \theta_{y,0} \tag{4.94}$$

Finally, the feed-through parameter, δ, is defined as,

$$\delta = \frac{b_0}{K} \tag{4.95}$$

where K is the normalization gain applied to the input. The parameters are transformed, as in Equation (4.69), such that,

$$\theta_{\pm} = \begin{bmatrix} T_u^{-\top}\theta_{u,0}^{\pm} \\ T_y^{-\top}\theta_{y,0}^{\pm} \\ \delta \end{bmatrix} \tag{4.96}$$

Using the definition of the observer in Equations (4.86) – (4.88), and a calculation of the parameters as shown in Equation (4.96), the observer was simulated. The parameter convergence is shown in Figure 4-6, normalized by the true values determined in Equation (4.96). Figure 4-8 shows the current profile used for the simulation, ensuring persistent excitation.

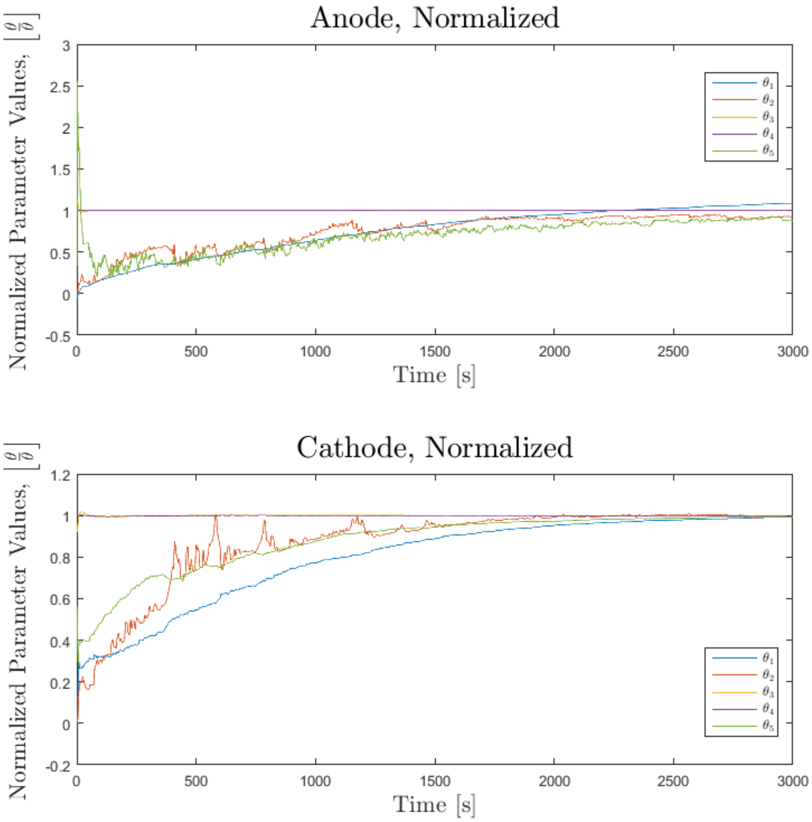

Figure 4-6: Normalized convergence of the parameters of an adaptive observer under the conditions presented in Section 4.3.1 for the solid electrode dynamics.

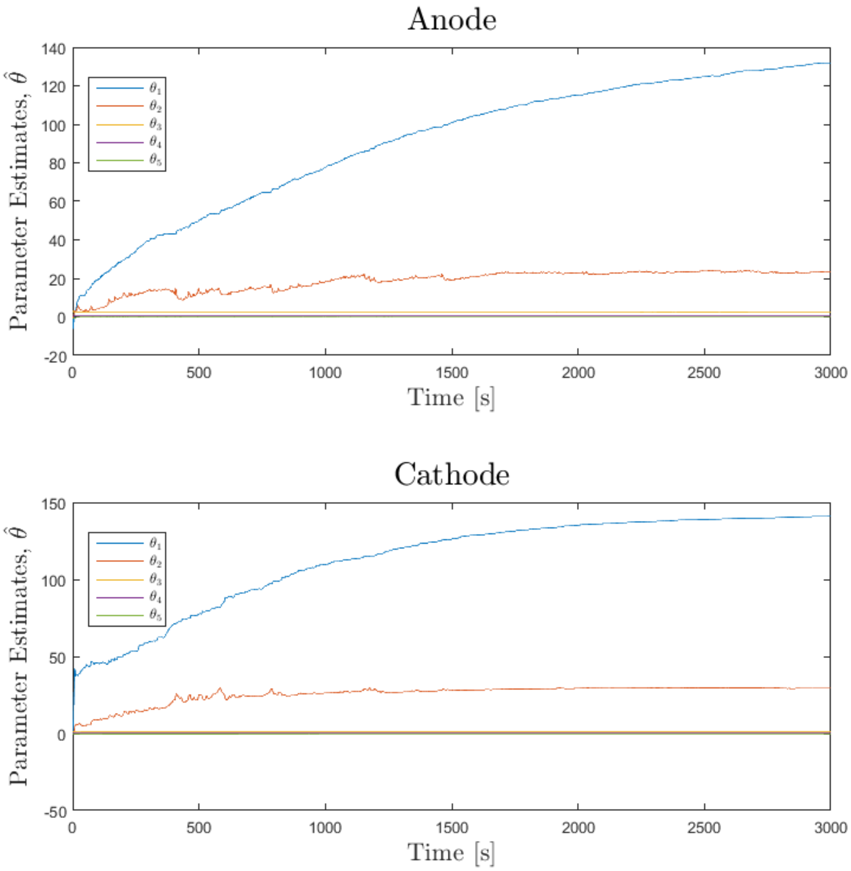
Anode

Cathode

Figure 4-7: Full magnitude parameter convergence of the adaptive observer for the solid electrode dynamics.

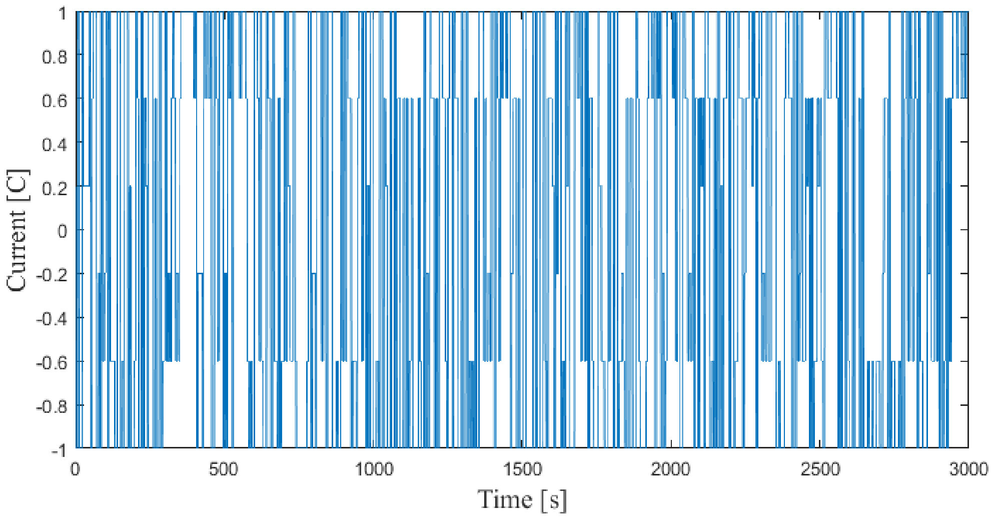

Figure 4-8: PRBS profile used for simulation as the current input.

4.3.2 Molar Flux Estimate

The next observer to construct is that of the molar flux prediction, $\boldsymbol{j}^*$, shown as $G_{j^*}(s)$ in Figure 4-4. It is hypothesized that a molar flux prediction can be made by using a linear combination of input measurements, $I(t)$; and output measurements, $V(t)$. This combination has time-varying gains, and may include a set of filters applied to the current. Molar flux is in many ways a filtered function of current, as the integration of molar flux is equal to the current through the cell, $\int_0^{L^\pm} j^\pm(x,t)dx = \mp I(t)$. Figure 4-9 shows the equivalent block diagram of this observer. In the interest of testing this hypothesis, two test cases were used to determine the best application of this theory to an a-priori estimate of the molar flux. The concept of the molar flux as a measurable output will be discussed in Section 4.4.

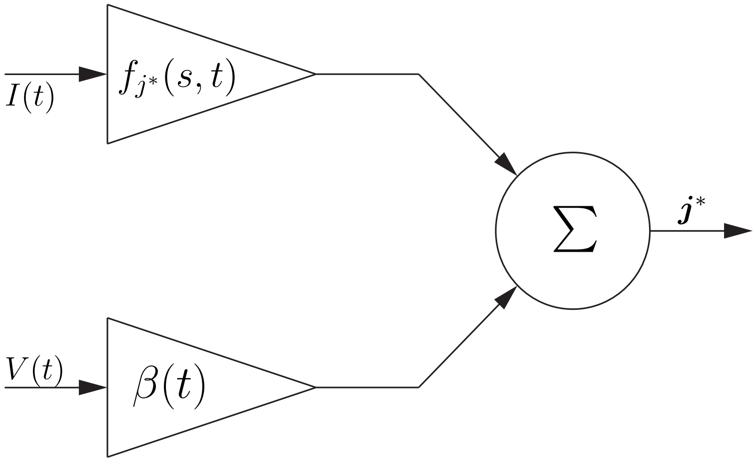

Figure 4-9: Block diagram of the molar flux function subsystem, assuming measurable inputs and outputs.

Test Case 1

The first test case is arguably the simplest, such that the molar flux at each node, i, is equal to a unique, time-varying coefficient multiplied by the current, and another multiplied by the voltage. This is shown in Equation (4.97), with a known gain applied to the molar flux to ease computational burden, as was the approach in Equation (4.79).

$$Kj_i^* = \alpha_i(t)I(t) + \beta_i(t)V(t) \tag{4.97}$$

This creates analogously two regressors, one for the current and one for the voltage, without any inertia or filtration. Subsequently, the parameters of this system are defined by,

$$\theta_j(t) = \left[\begin{array}{cccccc} \alpha_1(t) & \beta_1(t) & \cdots & \alpha_N(t) & \beta_N(t) \end{array} \right]^\top \tag{4.98}$$

The estimated system is defined as,

$$K\hat{j}_i^* = \widehat{\alpha}_i(t)I(t) + \widehat{\beta}_i(t)V(t) \tag{4.99}$$

with estimated parameters,

$$\hat{\theta}_j(t) = \left[\begin{array}{cccccc} \widehat{\alpha}_1(t) & \widehat{\beta}_1(t) & \cdots & \widehat{\alpha}_N(t) & \widehat{\beta}_N(t) \end{array} \right]^\top \tag{4.100}$$

The regressor matrix, which is directly measurable, is defined as,

$$\Omega_\pm = \begin{bmatrix} I & V & 0 & 0 & \cdots & 0 & 0 \\ 0 & 0 & I & V & \cdots & 0 & 0 \\ \vdots & \vdots & \vdots & \vdots & \ddots & \vdots & \vdots \\ 0 & 0 & 0 & 0 & \cdots & I & V \\ G(s)I & G(s)V & 0 & 0 & \cdots & 0 & 0 \\ 0 & 0 & G(s)I & G(s)V & \cdots & 0 & 0 \\ \vdots & \vdots & \vdots & \vdots & \ddots & \vdots & \vdots \\ 0 & 0 & 0 & 0 & \cdots & G(s)I & G(s)V \\ G^k(s)I & G^k(s)V & 0 & 0 & \cdots & 0 & 0 \\ 0 & 0 & G^k(s)I & G^k(s)V & \cdots & 0 & 0 \\ \vdots & \vdots & \vdots & \vdots & \ddots & \vdots & \vdots \\ 0 & 0 & 0 & 0 & \cdots & G^k(s)I & G^k(s)V \end{bmatrix} \tag{4.101}$$

where filtered iterations of the input and output are used to create a full-rank matrix, for N nodes, such that each filter is defined as,

$$G^i(s) = \left(\frac{\beta}{s+\beta}\right)^i \tag{4.102}$$

for $i \in [1 \ldots k]$, $k = N-1$. The error in the output, $\tilde{j}_i^*$ is defined as,

$$\tilde{j}_i^* = K\hat{j}_i^* - Kj_i^* \tag{4.103}$$

while the full error vector, E, of the regressor matrix equivalent system, $\Omega_\pm\hat{\theta}$ is defined as,

$$E = \begin{bmatrix} \tilde{j}_1^* & \cdots & \tilde{j}_N^* & G(s)\tilde{j}_1^* & \cdots & G(s)\tilde{j}_N^* & G^k(s)\tilde{j}_1^* & \cdots & G^k(s)\tilde{j}_N^* \end{bmatrix}^\top \tag{4.104}$$

An update law is created from (4.101) and (4.104) to update the parameters of Equation (4.100), such that,

$$\dot{\hat{\theta}}_j = -\Gamma\Omega_\pm^\top E \tag{4.105}$$

Figure 4-10 shows the error results of this application, using the simulation current profile of Figure 4-8. Figure 4-11 shows the resulting coefficient values for this simulation. It should be noted that there are no explicitly defined "true" parameters for this observer, only a desire to diminish the error as much as possible, while minimiz-

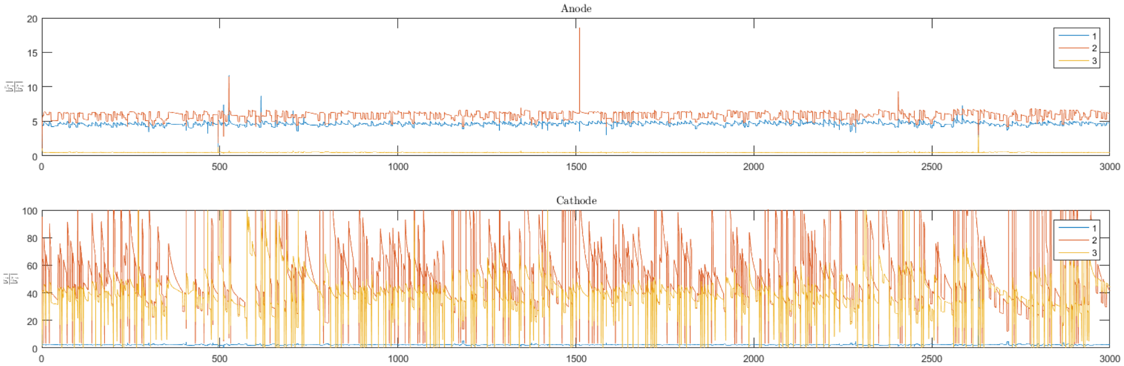

Figure 4-10: Error results while using a scalar coefficient for both input, $I(t)$; and output, $V(t)$.

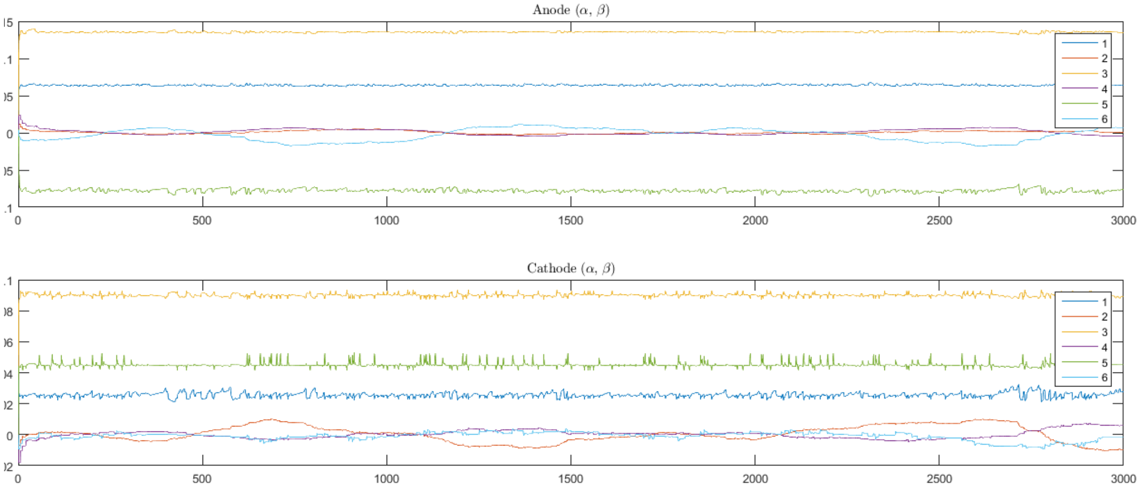

Figure 4-11: Resulting time-varying parameters of the molar flux observer system. The current has a fairly constant dependency, while the voltage dependency varies significantly.

ing the necessary gain to achieve this end. By examining Figure 4-10, it is seen that the normalized error in the anode is substantive, but there persists a steady-state error for one of the terms. Contrary to this reasonable performance in the anode, the cathode see wildly varying error terms. This is predictable because the cathode has faster diffusion rates, and therefore more variance in molar flux terms. In Figure 4-11, which depicts the converged value of the parameters, it can be seen that the strongest dependency is on the input current, $I(t)$, for each molar flux term. The relationship to the output, $V(t)$, is significantly time-varying, oscillating around zero. Therefore, to alleviate this performance insufficiency, a more complex regressor was created, with a higher built-in correlation to the frequency content of the input, $I(t)$, as described below.

Test Case 2

To reduce the error bias, additional filters are applied to the current, and unknown coefficients are added to the parameter set. This results in a hypothetical definition of the molar flux, $\hat{j}_i^*$, such that,

$$K\hat{j}_i^* = \alpha_i(t)I(t) + \beta_i(t)V(t) + \gamma_i(t)^\top f(s)I(t) \tag{4.106}$$

where the filter-adjacent parameter vector, γ_i, is defined as,

$$\gamma_i(t) = \left[\begin{array}{ccc} \gamma_{i,1}(t) & \cdots & \gamma_{i,q}(t) \end{array}\right]^\top \tag{4.107}$$

and a vector of filters, $f(s)$, defined by,

$$f(s) = \left[\begin{array}{ccc} \left(\frac{k_1}{s+k_1}\right) & \cdots & \left(\frac{k_q}{s+k_q}\right) \end{array}\right]^\top \tag{4.108}$$

for $q = n_f$. To ensure a wide spectrum of frequency content, multiple poles, k_i, are defined as,

$$k_i = 2^{(1-i)} \tag{4.109}$$

for use in the filter vector, $f(s)$, as shown in Equation (4.108). The full set of parameters for use with the regressors is defined by,

$$\begin{gathered} \theta_j(t) = \\ \left[\begin{array}{ccccccccccc} \alpha_1(t) & \beta_1(t) & \gamma_{1,1}(t) & \cdots & \gamma_{1,q}(t) & \alpha_2(t) & \cdots & \alpha_N(t) & \beta_N(t) & \gamma_{N,1}(t) & \cdots & \gamma_{N,q}(t) \end{array}\right]^\top \end{gathered} \tag{4.110}$$

An output error, $\tilde{j}_i^*$, for each node, i, is subsequently defined as,

$$K\tilde{j}_i^* = K\hat{j}_i^* - Kj_i^* \tag{4.111}$$

where it is again assumed that j_i^* is measurable. The regressor matrix, $\Omega_\pm$, is defined as shown in Equation (4.112). This matrix is both full column rank and full row rank.

$$\Omega_\pm = \\ \begin{bmatrix} I & V & f(s)I & 0 & 0 & 0 & \cdots & 0 & 0 & 0 \\ 0 & 0 & 0 & I & V & f(s)^\top I & \cdots & 0 & 0 & 0 \\ \vdots & \vdots & \vdots & \vdots & \vdots & \vdots & \ddots & \vdots & \vdots & \vdots \\ 0 & 0 & 0 & 0 & 0 & 0 & \cdots & I & V & f(s)^\top I \\ G(s)I & G(s)V & G(s)f(s)^\top I & 0 & 0 & 0 & \cdots & 0 & 0 & 0 \\ 0 & 0 & 0 & G(s)I & G(s)V & G(s)f(s)^\top I & \cdots & 0 & 0 & 0 \\ \vdots & \vdots & \vdots & \vdots & \vdots & \vdots & \ddots & \vdots & \vdots & \vdots \\ 0 & 0 & 0 & 0 & 0 & 0 & \cdots & G(s)I & G(s)V & G(s)f(s)^\top I \\ G^k(s)I & G^k(s)V & G^k(s)f(s)^\top I & 0 & 0 & 0 & \cdots & 0 & 0 & 0 \\ 0 & 0 & 0 & G^k(s)I & G^k(s)V & G^k(s)f(s)^\top I & \cdots & 0 & 0 & 0 \\ \vdots & \vdots & \vdots & \vdots & \vdots & \vdots & \ddots & \vdots & \vdots & \vdots \\ 0 & 0 & 0 & 0 & 0 & 0 & \cdots & G^k(s)I & G^k(s)V & G^k(s)f(s)^\top I \end{bmatrix} \tag{4.112}$$

where each regressor is filtered with $G(s)$, similarly defined as,

$$G(s) = \frac{\beta}{s+\beta} \tag{4.113}$$

A full error vector, E, is defined as,

$$\begin{aligned} E =& K \begin{bmatrix} \tilde{j}_1^* & \cdots & \tilde{j}_N^* & G(s)\tilde{j}_1^* & \cdots & G(s)\tilde{j}_N^* & G^k(s)\tilde{j}_1^* & \cdots & G^k(s)\tilde{j}_N^* \end{bmatrix}^\top \\ =& \Omega_\pm^\top \hat{\theta} - \\ & K \begin{bmatrix} j_1^* & \cdots & j_N^* & G(s)j_1^* & \cdots & G(s)j_N^* & G^k(s)j_1^* & \cdots & G^k(s)j_N^* \end{bmatrix}^\top \end{aligned} \tag{4.114}$$

Finally, an update law, combining Equations (4.112) and (4.114), defines the estimations of the parameters, such that,

$$\dot{\hat{\theta}}_j = -\Gamma \Omega_\pm^\top E \tag{4.115}$$

This observer system was simulated using the current profile shown in Figure 4-8. Figure 4-12 shows the resulting error using the update law of Equation (4.115), trying exclusively to minimize error. It can be seen that the RMS error for the anode molar

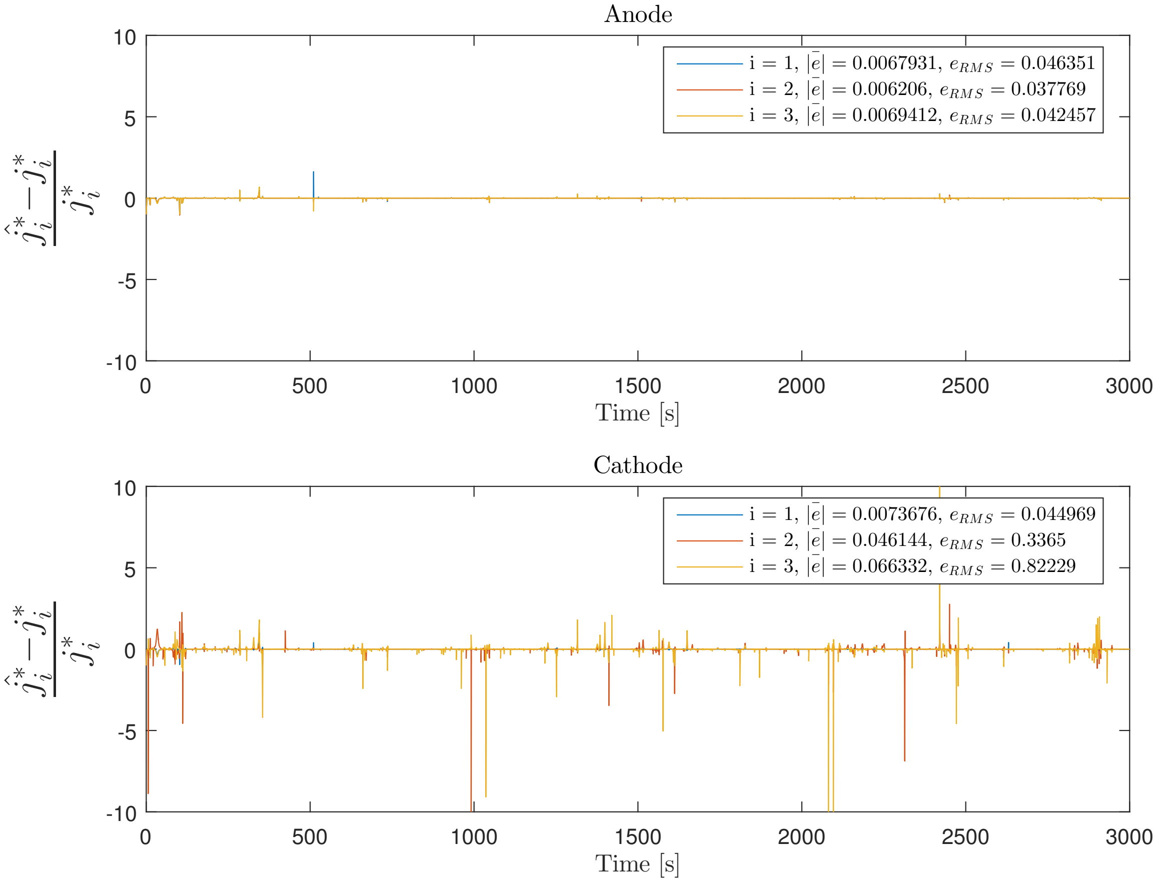

Figure 4-12: Resulting error of the anode and cathode a-priori calculation of the molar flux, j_i^*, for each node, i.

flux terms is driven to below 5%, with an average absolute error below 0.7%. In the cathode, the previous culprit, the error is more persistent, with an average absolute error less than 6.7%. Figure 4-13 shows the parameter values found within the anode, while Figure 4-14 shows the parameter values found in the cathode. It is interesting to note that the strongest correlating coefficient is of the slowest pole. This could be attributed to either a strong memory of the current, or a correction for the highest attenuation. Using this predictive method, an a-priori estimate of the molar flux vector, $\boldsymbol{j}^*$, is achieved.

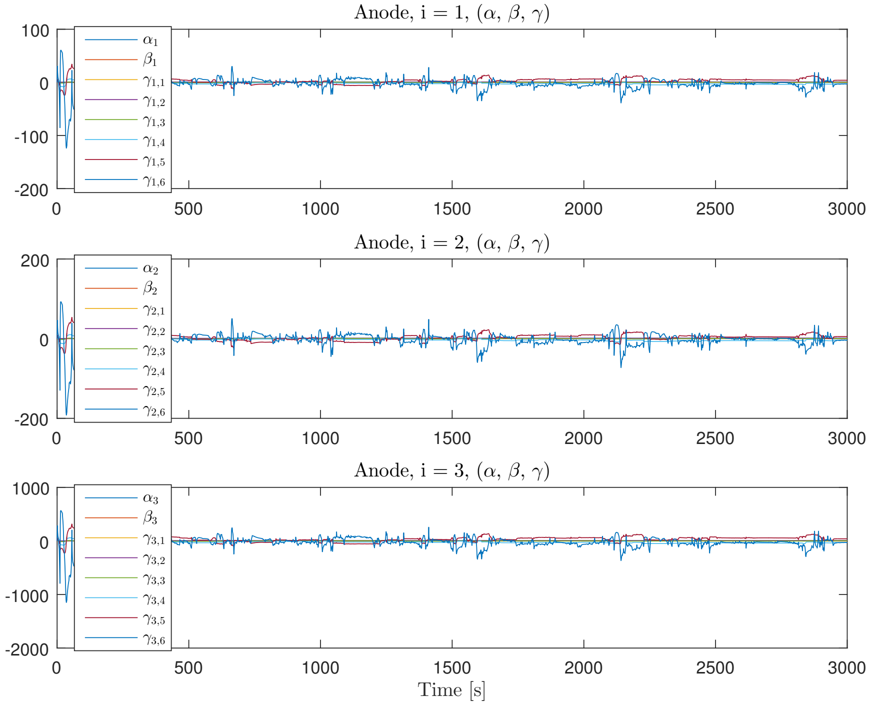

Figure 4-13: Time-varying parameter values of equivalent regressor system for the anode.

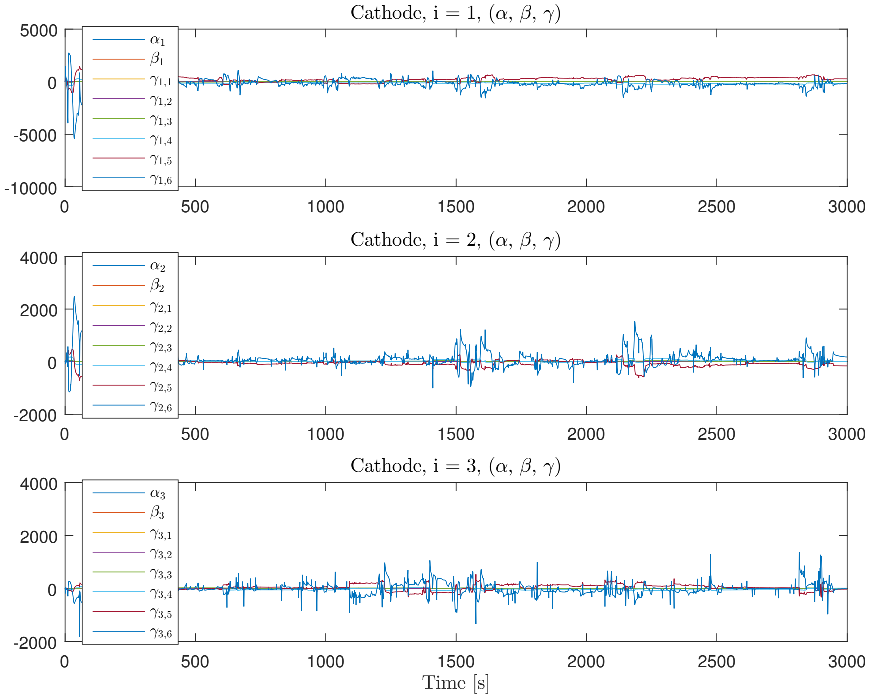

Figure 4-14: Time-varying parameter values of equivalent regressor system for the cathode.

4.3.3 Electrolyte Observer

The final observer that this thesis will focus on is that of the electrolyte concentration, based on Equation (3.157), and represented as $G_{c_e}(s)$ in Figure 4-4. First, a state-space representation of the system is defined, such that,

$$\begin{aligned} \dot{x} &= Ax + Bu \\ y &= Cx \end{aligned} \tag{4.116}$$

where $A \in \mathbb{R}^{q \times q}$ is defined as,

$$A = \frac{1}{(l')^2} \mathbf{M}^{-1} \mathbf{K} \tag{4.117}$$

$B \in \mathbb{R}^{q \times n}$ is defined as,

$$B = \frac{t_a^0 a^{\pm}}{\epsilon_e^{\pm}} \mathbf{M}^{-1} \mathbf{L} \tag{4.118}$$

and $C \in \mathbb{R}^{q \times m}$ defined as,

$$C = \begin{bmatrix} 1 & 0 & \cdots & 0 & 0 \\ 0 & 0 & \cdots & 0 & 0 \\ 0 & 1 & \cdots & 0 & 0 \\ 0 & 0 & \cdots & 0 & 0 \\ \vdots & \vdots & \ddots & \vdots & \vdots \\ 0 & 0 & \cdots & 1 & 0 \\ 0 & 0 & \cdots & 0 & 0 \end{bmatrix} \tag{4.119}$$

for $u \in \mathbb{R}^n$ and $y \in \mathbb{R}^m$. For multiple-input, multiple-output systems, the system has no pure canonical form, and instead a matrix of transfer functions is generated, such that,

$$\frac{Y(s)}{U(s)} = \begin{bmatrix} \frac{y_1(s)}{u_1(s)} & \cdots & \frac{y_1(s)}{u_n(s)} \\ \vdots & \ddots & \vdots \\ \frac{y_m(s)}{u_1(s)} & \cdots & \frac{y_m(s)}{u_n(s)} \end{bmatrix} \tag{4.120}$$

where each $\frac{y_j(s)}{u_i(s)}$ is the transfer function from input channel, i, to output channel, j. For this consideration, a naïve adaptive observer could be constructed in much the same way as delineated in Sections 4.1 and 4.2, such that a vector of parameters is defined for every output channel, $j \in [1 \cdots m]$,

$$
\begin{aligned}
\theta_1 &= \begin{bmatrix} \theta_{y_1} & \theta_{u_1,y_1} & \cdots & \theta_{u_n,y_1} \end{bmatrix}^\top \\
\theta_2 &= \begin{bmatrix} \theta_{y_2} & \theta_{u_2,y_2} & \cdots & \theta_{u_n,y_2} \end{bmatrix}^\top \\
&\vdots \\
\theta_m &= \begin{bmatrix} \theta_{y_m} & \theta_{u_2,y_m} & \cdots & \theta_{u_n,y_m} \end{bmatrix}^\top
\end{aligned}
\tag{4.121}
$$

An associated set of regressors for each output channel can be constructed as,

$$
\begin{aligned}
\omega_1 &= \begin{bmatrix} \omega_{y_1} & \omega_{u_1} & \cdots & \omega_{u_n} \end{bmatrix}^\top \\
\omega_2 &= \begin{bmatrix} \omega_{y_2} & \omega_{u_1} & \cdots & \omega_{u_n} \end{bmatrix}^\top \\
&\vdots \\
\omega_m &= \begin{bmatrix} \omega_{y_m} & \omega_{u_1} & \cdots & \omega_{u_n} \end{bmatrix}^\top
\end{aligned}
\tag{4.122}
$$

and the output of the equivalent system, Y, is defined as,

$$
Y = \begin{bmatrix} y_1 & y_2 & \cdots & y_m \end{bmatrix}^\top \tag{4.123}
$$

Each output channel of the equivalent system is defined as,

$$
y_j = \theta_j^\top \omega_j \tag{4.124}
$$

In the ANCF II model, $n = 6$, $m = 6$ and $q = 12$. This results in the total number of equivalent system parameters, $N_{\theta_e} = mq(n+1)$, or $N_{\theta_e} = 504$. This is a high number of parameters to estimate accurately, since there are so many degrees of freedom of the equivalent system. It is also noted that, from a BMS standpoint, the original model only has 7 unknowns. These are the element diffusion coefficient and normalized length quotients, $\frac{D_i(t)}{(l_i')^2}$, of which there are five; and the volume input gains, $\frac{t_a^0 a^\pm}{\epsilon_e^\pm}$, of which there are two. Therefore, an exploration of a novel adaptive observer to determine lumped parameters of a system with a known structure is considered, motivated by a desire to constrain learning to values that are truly unknown.

Exploration of Lumped Parameters

To begin, an observer will be developed to determine the lumped parameters of a second order MIMO system, which can then be scaled to the transfer function matrix shown in Equation (4.120). An exploration of the resulting transfer functions of known system matrices follows, such that,

$$A = \begin{bmatrix} a & b \\ c & d \end{bmatrix} \quad B = \begin{bmatrix} e & f \\ g & h \end{bmatrix} \quad C = \begin{bmatrix} 1 & 0 \\ 0 & 1 \end{bmatrix} \tag{4.125}$$

where the resulting poles of the transfer function are the determinant, $|s\mathrm{I} - A|$, or,

$$\begin{aligned} (s\mathrm{I} - A)^{-1} &= \frac{1}{(s-a)(s-d) - cb} \begin{bmatrix} s-d & b \\ c & s-a \end{bmatrix} \\ &= \frac{1}{s^2 - (a+d)s + (ad - cb)} \begin{bmatrix} s-d & b \\ c & s-a \end{bmatrix} \end{aligned} \tag{4.126}$$

The first transfer function, as defined from the first input channel to the first output channel is,

$$\begin{aligned} &\frac{Y_1(s)}{U_1(s)} = \\ &\qquad \begin{bmatrix} 1 & 0 \end{bmatrix} \left(\frac{1}{s^2 - (a+d)s + (ad - cb)} \begin{bmatrix} s-d & b \\ c & s-a \end{bmatrix} \begin{bmatrix} e \\ g \end{bmatrix} \right) \end{aligned} \tag{4.127}$$

where the simplified transfer function is defined as,

$$\frac{Y_1(s)}{U_1(s)} = \frac{es + (gb - ed)}{s^2 - (a+d)s + (ad - cb)} \tag{4.128}$$

Each additional transfer function can be similarly defined as,

$$\begin{aligned}\frac{Y_2(s)}{U_1(s)} &= \frac{gs + (ec - ga)}{s^2 - (a+d)s + (ad - cb)} \\ \frac{Y_1(s)}{U_2(s)} &= \frac{fs + (hb - fd)}{s^2 - (a+d)s + (ad - cb)} \\ \frac{Y_2(s)}{U_2(s)} &= \frac{hs + (fc - ha)}{s^2 - (a+d)s + (ad - cb)}\end{aligned} \tag{4.129}$$

Subsequently, an additional system is created with a lumped system parameter, α; and a lumped input parameter, β, which results in the following description,

$$A_p = \alpha A = \begin{bmatrix} \alpha a & \alpha b \\ \alpha c & \alpha d \end{bmatrix} \quad B_p = \beta B = \begin{bmatrix} \beta e & \beta f \\ \beta g & \beta h \end{bmatrix} \quad C = \begin{bmatrix} 1 & 0 \\ 0 & 1 \end{bmatrix} \tag{4.130}$$

Again, the poles are calculated using the determinant, such that,

$$\begin{aligned}(s\mathrm{I} - A_p)^{-1} &= \frac{1}{(s - \alpha a)(s - \alpha d) - \alpha^2 cb} \begin{bmatrix} s - \alpha d & \alpha b \\ \alpha c & s - \alpha a \end{bmatrix} \\ &= \frac{1}{s^2 - \alpha(a+d)s + \alpha^2(ad - cb)} \begin{bmatrix} s - \alpha d & \alpha b \\ \alpha c & s - \alpha a \end{bmatrix}\end{aligned} \tag{4.131}$$

The first transfer function, for clarity, is explicitly defined as,

$$\begin{aligned}&\frac{Y_1(s)}{U_1(s)} = \\ &\begin{bmatrix} 1 & 0 \end{bmatrix} \left(\frac{1}{s^2 - \alpha(a+d)s + \alpha^2(ad - cb)} \begin{bmatrix} s - \alpha d & \alpha b \\ \alpha c & s - \alpha a \end{bmatrix} \begin{bmatrix} \beta e \\ \beta g \end{bmatrix} \right)\end{aligned} \tag{4.132}$$

with a simplified form,

$$\frac{Y_1(s)}{U_1(s)} = \frac{\beta(es + \alpha(gb - ed))}{s^2 - \alpha(a+d)s + \alpha^2(ad - cb)} \tag{4.133}$$

Each subsequent transfer function is defined as,

$$\begin{aligned}\frac{Y_2(s)}{U_1(s)} &= \frac{\beta(gs+\alpha(ec-ga))}{s^2-\alpha(a+d)s+\alpha^2(ad-cb)}\\ \frac{Y_1(s)}{U_2(s)} &= \frac{\beta(fs+\alpha(hb-fd))}{s^2-\alpha(a+d)s+\alpha^2(ad-cb)}\\ \frac{Y_2(s)}{U_2(s)} &= \frac{\beta(hs+\alpha(fc-ha))}{s^2-\alpha(a+d)s+\alpha^2(ad-cb)}\end{aligned} \tag{4.134}$$

Looking at Equations (4.129) and (4.134), a pattern begins to emerge regarding the influence of the lumped parameters on the resulting transfer functions. Namely, it can be shown that for any order system organized in the form above, the following relationship holds true,

$$G(s) = \frac{\beta b_{p,1}s^{q-1} + \beta\alpha b_{p,2}s^{q-2} + \ldots + \beta\alpha^{q-1}b_{p,q}}{s^k + \alpha a_{p,1}s^{q-1} + \ldots + \alpha^q a_{p,q}} \tag{4.135}$$

where $b_{p,k}$ and $a_{p,k}$ are known coefficients of the transfer function, for $k \in [1 \cdots q]$, while α and β are unknown lumped parameters. While this is an interesting observation, it does not directly lead to the construction of an adaptive observer. Instead, a function for the equivalent parameters, θ, needs to be determined, and not a function to determine the transfer function coefficient. As an example for examining this procedure, a second order transfer function takes the form,

$$G_p(s) = \frac{\beta b_{p,1}s + \beta\alpha b_{p,2}}{s^2 + \alpha a_{p,1}s + \alpha^2 a_{p,2}} \tag{4.136}$$

An arbitrary, negative definite filter, F, is defined in observer canonical form,

$$F = \begin{bmatrix} 0 & 1 \\ -a_{f,2} & -a_{f,1} \end{bmatrix} \tag{4.137}$$

and an input vector, g,

$$g = \begin{bmatrix} 0 & 1 \end{bmatrix}^\top \tag{4.138}$$

For a single-input, single-output system, the regressor equivalent system can be defined as,

$$\begin{aligned}\dot{\omega}_u &= F\omega_u + gu \\ \dot{\omega}_y &= F\omega_y + gy\end{aligned} \tag{4.139}$$

where the output, y, is simultaneously defined as,

$$\begin{aligned}y &= \theta^\top \begin{bmatrix} \omega_u \\ \omega_y \end{bmatrix} \\ &= \theta^\top \omega\end{aligned} \tag{4.140}$$

The parameters, θ, are explicitly defined as the numerator coefficients of the two equivalent system outputs, notationally expressed as,

$$\theta = \begin{bmatrix} b_{u,2} & b_{u,1} & b_{y,2} & b_{y,1} \end{bmatrix}^\top \tag{4.141}$$

where the transfer function of the single-input, single-output adaptive observer is,

$$G_o(s) = \frac{b_{u,1}s + b_{u,2}}{s^2 + (a_{f,1} - b_{y,1})\, s + (a_{f,2} - b_{y,2})} \tag{4.142}$$

Now, using the transfer function of Equations (4.136) and (4.142), the parameters of the observer, θ, can be defined as a function of known parameters, $a_{p,i}$ and $b_{p,i}$; and unknown parameters, α and β, such that,

$$\begin{aligned}b_{u,1} &= \beta b_{p,1} \\ \Rightarrow \beta &= \frac{b_{u,1}}{b_{p,1}}\end{aligned} \tag{4.143}$$

It is important that this coefficient, $b_{u,1}$ is a linear function of one unknown, β. It will be used in the subset of parameters to be observed. Subsequently, the other coefficients are defined,

$$b_{u,2} = \beta\alpha b_{p,2} \tag{4.144}$$

$$\begin{aligned} a_{f,1} - b_{y,1} &= \alpha a_{p,1} \\ \Rightarrow \alpha &= \frac{a_{f,1} - b_{y,1}}{a_{p,1}} \end{aligned} \tag{4.145}$$

where an output parameter, $b_{y,1}$, is again a linear function of the unknown parameter, α. The subsequent nonlinear parameter for a second order system is defined as,

$$b_{y,2} = a_{f,2} - \alpha^2 a_{p,2} \tag{4.146}$$

This definition of the observer parameters, θ, can be generalized to a q^{th} order system as,

$$\theta = \begin{bmatrix} \frac{\theta_\beta}{b_{p,1}} \left(\frac{a_{f,1} - \theta_\alpha}{a_{p,1}} \right)^{q-1} b_{p,q} \\ \vdots \\ \frac{\theta_\beta}{b_{p,1}} \left(\frac{a_{f,1} - \theta_\alpha}{a_{p,1}} \right) b_{p,2} \\ \theta_\beta \\ a_{f,q} - \left(\frac{a_{f,1} - \theta_\alpha}{a_{p,1}} \right)^{q} a_{p,q} \\ \vdots \\ a_{f,2} - \left(\frac{a_{f,1} - \theta_\alpha}{a_{p,1}} \right)^{2} a_{p,2} \\ \theta_\alpha \end{bmatrix} \tag{4.147}$$

where θ_β and θ_α are linear functions of β and α, respectively. Now that the full parameters, θ, are defined as a function of the lumped parameter subset, α and β, an update law can be devised. The subset of parameters, θ^*, is defined as,

$$\theta^* = \begin{bmatrix} \theta_\beta & \theta_\alpha \end{bmatrix}^\top \tag{4.148}$$

Using a definition similar to gradient descent [4], a differentiation is applied to the error equation,

$$e = \hat{y} - y \tag{4.149}$$

where,

$$\hat{y} = \hat{\theta}^\top \hat{\omega} \tag{4.150}$$

such that,

$$\frac{\partial e}{\partial \hat{\theta}^*} = \frac{\partial \hat{y}}{\partial \hat{\theta}^*} \tag{4.151}$$

Given that the output, y, is predetermined and not a function of the estimated system, the derivative of the error with respect to the subset of parameters is only a function of the derivate of the estimated output with respect to the subset of parameters. This expression can be further reduced as,

$$\frac{\partial \hat{y}}{\partial \hat{\theta}^*} = \frac{\partial \hat{\theta}^\top}{\partial \hat{\theta}^*}\hat{\omega} \tag{4.152}$$

as the regressors are independent of the parameters, θ, and their subset, θ^*, that define the system. Using the expression shown in Equation (4.152), an update law begins to take form. A Jacobian is first generally defined as,

$$J = \frac{\partial \theta}{\partial \theta^*} = \begin{bmatrix} \frac{b_{p,k}}{b_{p,1}}\left(\frac{a_{f,1}-\theta_\alpha}{a_{p,1}}\right)^{k-1} & -(k-1)\frac{\theta_\beta b_{p,k}}{b_{p,1}a_{p,1}}\left(\frac{a_{f,1}-\theta_\alpha}{a_{p,1}}\right)^{k-2} \\ \vdots & \vdots \\ \frac{b_{p,i}}{b_{p,1}}\left(\frac{a_{f,1}-\theta_\alpha}{a_{p,1}}\right)^{i-1} & -(i-1)\frac{\theta_\beta b_{p,i}}{b_{p,1}a_{p,1}}\left(\frac{a_{f,1}-\theta_\alpha}{a_{p,1}}\right)^{i-2} \\ \vdots & \vdots \\ \frac{b_{p,2}}{b_{p,1}}\left(\frac{a_{f,1}-\theta_\alpha}{a_{p,1}}\right) & -\frac{\theta_\beta b_{p,i}}{b_{p,1}a_{p,1}} \\ 1 & 0 \\ 0 & k\frac{a_{p,k}}{a_{p,1}}\left(\frac{a_{f,1}-\theta_\alpha}{a_{p,1}}\right)^{k-1} \\ \vdots & \vdots \\ 0 & i\frac{a_{p,i}}{a_{p,1}}\left(\frac{a_{f,1}-\theta_\alpha}{a_{p,1}}\right)^{i-1} \\ \vdots & \vdots \\ 0 & 2\frac{a_{p,2}}{a_{p,1}}\left(\frac{a_{f,1}-\theta_\alpha}{a_{p,1}}\right) \\ 0 & 1 \end{bmatrix} \tag{4.153}$$

Then, using this Jacobian, an update law for the subset of parameters is devised, such that,

$$\dot{\hat{\theta}}^* = -\gamma \mathrm{J}^\top \hat{\omega} e \tag{4.154}$$

where,

$$J = J|_{\theta^*=\hat{\theta}^*} \tag{4.155}$$

and the gains, $\gamma > 0$. The update law shown in Equation (4.154) will be applied to a test case to show its convergence, and subsequently extended to higher order cases, but its stability will first be considered. Figure 4-15 shows the simulation of a second-order SISO system. Note the rapid convergence of normalized parameters with minimal frequency content of the input. Figure 4-16 shows the same for a third-order sytem.

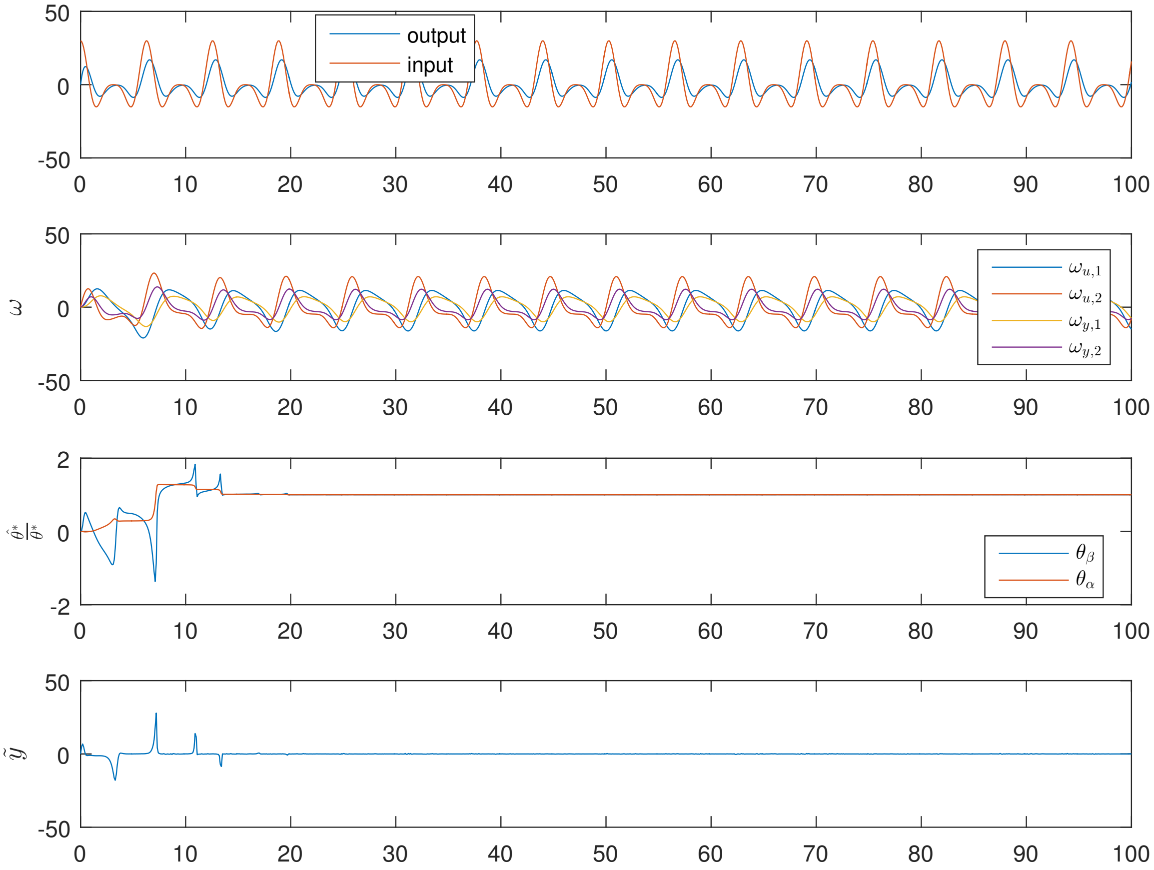

Figure 4-15: Test case for a second-order SISO plant showing inputs, $u(t)$; outputs, $y(t)$; regressors, ω; and the convergence of the parameter subset, $\hat{\theta}^*$, comprised of $\hat{\theta}_\beta$ and $\hat{\theta}_\alpha$.

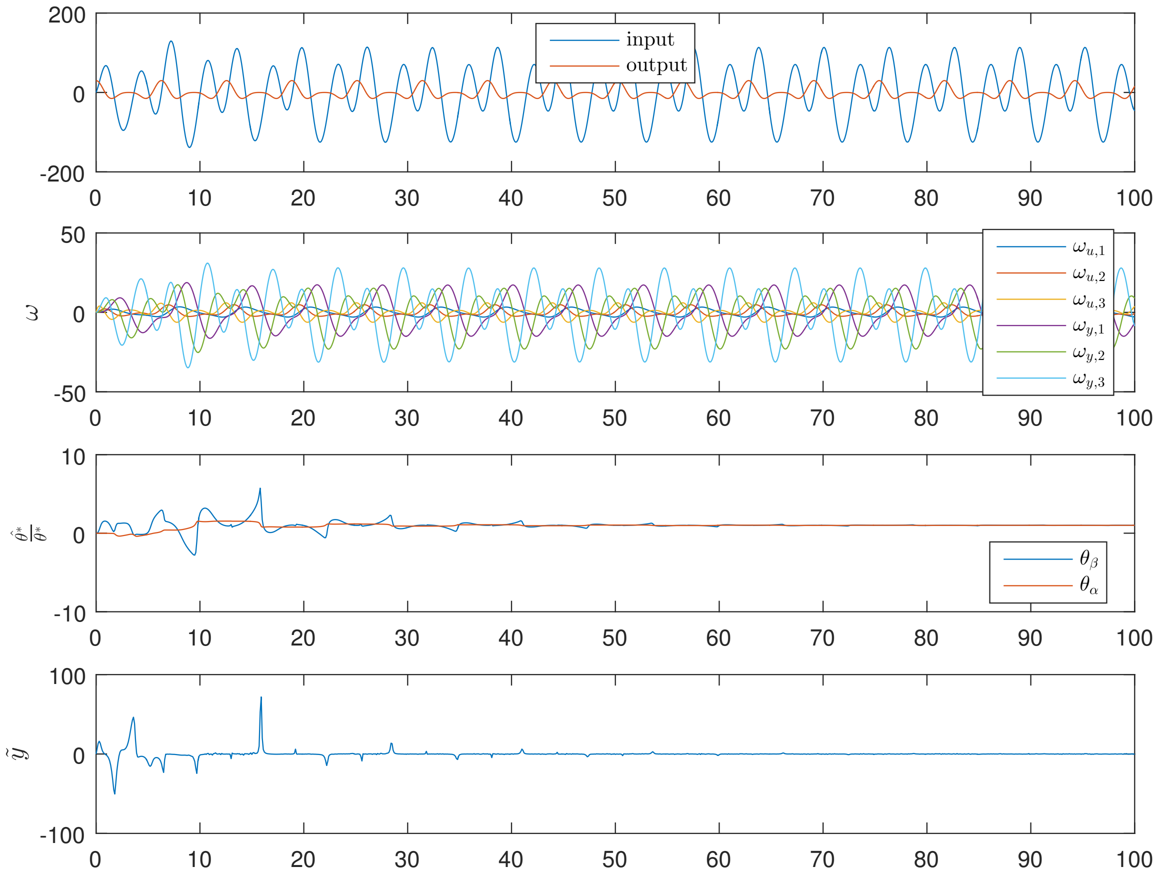

Figure 4-16: Test case for a third-order SISO plant showing inputs, $u(t)$; outputs, $y(t)$; regressors, ω; and the convergence of the parameter subset, $\hat{\theta}^*$, comprised of $\hat{\theta}_\beta$ and $\hat{\theta}_\alpha$.

Lyapunov Stability Analysis

To begin the stability analysis, several error terms need to be defined, first as the error in the observed parameters, $\tilde{\theta}$, such that,

$$\tilde{\theta} = \hat{\theta} - \theta \tag{4.156}$$

next as the error in the regressors, $\tilde{\omega}$, also called sensitivity error,

$$\tilde{\omega} = \hat{\omega} - \omega \tag{4.157}$$

and finally, the error in the output, e,

$$e = \hat{y} - y = \tilde{\theta}^\top \hat{\omega} + \theta^\top \tilde{\omega} \tag{4.158}$$

To study the stability of this update law, a positive semi-definite Lyapunov candidate function, $V(\tilde{\theta})$, is chosen, with the desire to define a negative semi-definite time derivative, such that,

$$\begin{aligned} V &\geq 0 \\ \dot{V} &\leq 0 \end{aligned} \tag{4.159}$$

Most conventionally [37], a Lyapunov candidate for adaptive observers is chosen as, $V = \tilde{\theta}^\top \tilde{\theta}$, but this leaves a term that is not sign-definite when calculating its time derivative using the Jacobian, J. Therefore, a Lyapunov candidate is proposed as,

$$V = \tilde{\theta}^\top \Phi^{-1} \tilde{\theta} \tag{4.160}$$

where the Jacobian correction term, Φ, is defined as,

$$\Phi = \mathrm{J}\mathrm{J}^\top \tag{4.161}$$

Subsequently, the time derivative of Equation (4.160) is defined as,

$$\dot{V} = 2\tilde{\theta}^\top \Phi^{-1} \dot{\tilde{\theta}} + \tilde{\theta}^\top \frac{\partial \Phi^{-1}}{\partial t} \tilde{\theta} \tag{4.162}$$

This expression will be considered in two separate terms, specifically the two additive terms. The first can be expanded using the definition of Equation (4.156), such that,

$$2\tilde{\theta}^\top \Phi^{-1} \dot{\tilde{\theta}} = 2\left(\hat{\theta} - \theta\right)^\top \Phi^{-1} \left(\dot{\hat{\theta}} - \dot{\theta}\right) \tag{4.163}$$

The true parameters, θ of the system are unchanging, $\dot{\theta} = 0$, so this expression can be simplified to,

$$2\tilde{\theta}^\top \Phi^{-1} \dot{\tilde{\theta}} = 2\tilde{\theta}^\top \Phi^{-1} \dot{\hat{\theta}} \tag{4.164}$$

The rate of change of the estimated parameters, $\dot{\hat{\theta}}$, is defined as,

$$\dot{\hat{\theta}} = \frac{\partial \hat{\theta}}{\partial \hat{\theta}^*} \frac{\partial \hat{\theta}^*}{\partial t} = \mathrm{J} \dot{\hat{\theta}}^* \tag{4.165}$$

Substituting the update law of Equation (4.154) and the error definition of Equation (4.158) into this expression yields,

$$\begin{aligned} \dot{\hat{\theta}} &= J \left(-\gamma J^\top \hat{\omega} e \right) \\ &= -\gamma \Phi \hat{\omega} \left(\tilde{\theta}^\top \hat{\omega} + \theta^\top \tilde{\omega} \right) \end{aligned} \tag{4.166}$$

From Equation (4.16), a definition of the filter which defines the regressors and the sensitivity error shows that,

$$\lim_{t \to \infty} \tilde{\omega} = 0 \tag{4.167}$$

Substituting this definition into Equation (4.166) generates a reduced definition of the parameter evolution,

$$\dot{\hat{\theta}} = -\gamma \Phi \hat{\omega} \tilde{\theta}^\top \hat{\omega} \tag{4.168}$$

The definition of Equation (4.168) can be substituted into Equation (4.164) to yield,

$$\begin{aligned} 2\tilde{\theta}^\top \Phi^{-1} \dot{\tilde{\theta}} &= -2\gamma \tilde{\theta}^\top \Phi^{-1} \Phi \hat{\omega} \tilde{\theta}^\top \hat{\omega} \\ &= -2\gamma \tilde{\theta}^\top \hat{\omega} \tilde{\theta}^\top \hat{\omega} \\ &= -2\gamma \left(\tilde{\theta}^\top \hat{\omega} \right)^2 \end{aligned} \tag{4.169}$$

Returning now to the expression shown in Equation (4.162), the time-derivative of the Lyapunov candidate is,

$$\dot{V} = -2\gamma \left(\tilde{\theta}^\top \hat{\omega} \right)^2 + \tilde{\theta}^\top \frac{\partial \Phi^{-1}}{\partial t} \tilde{\theta} \tag{4.170}$$

Given that the error term, $-2\gamma\left(\tilde{\theta}^{\top}\hat{\omega}\right)^2$ is sign definite, the onus of maintaining negativity falls on the definition of the rate of change of Φ^{-1}, such that,

$$\dot{V} \leq 0 \iff \tilde{\theta}^{\top}\frac{\partial\Phi^{-1}}{\partial t}\tilde{\theta} \leq 2\gamma\left(\tilde{\theta}^{\top}\hat{\omega}\right)^2 \tag{4.171}$$

It should be noted that Φ^{-1} is not well-defined, as Φ is not full rank, and therefore the time derivative of a pseudo-inverse Φ is considered sufficient. Figures 4-17 and 4-18 show the stability terms for the second and third order systems simulated in Figures 4-15 and 4-16, respectively. Note that the sign-definite terms are consistently larger in magnitude than the nebulous $\frac{\partial\Phi^{-1}}{\partial t}$ terms, in this case.

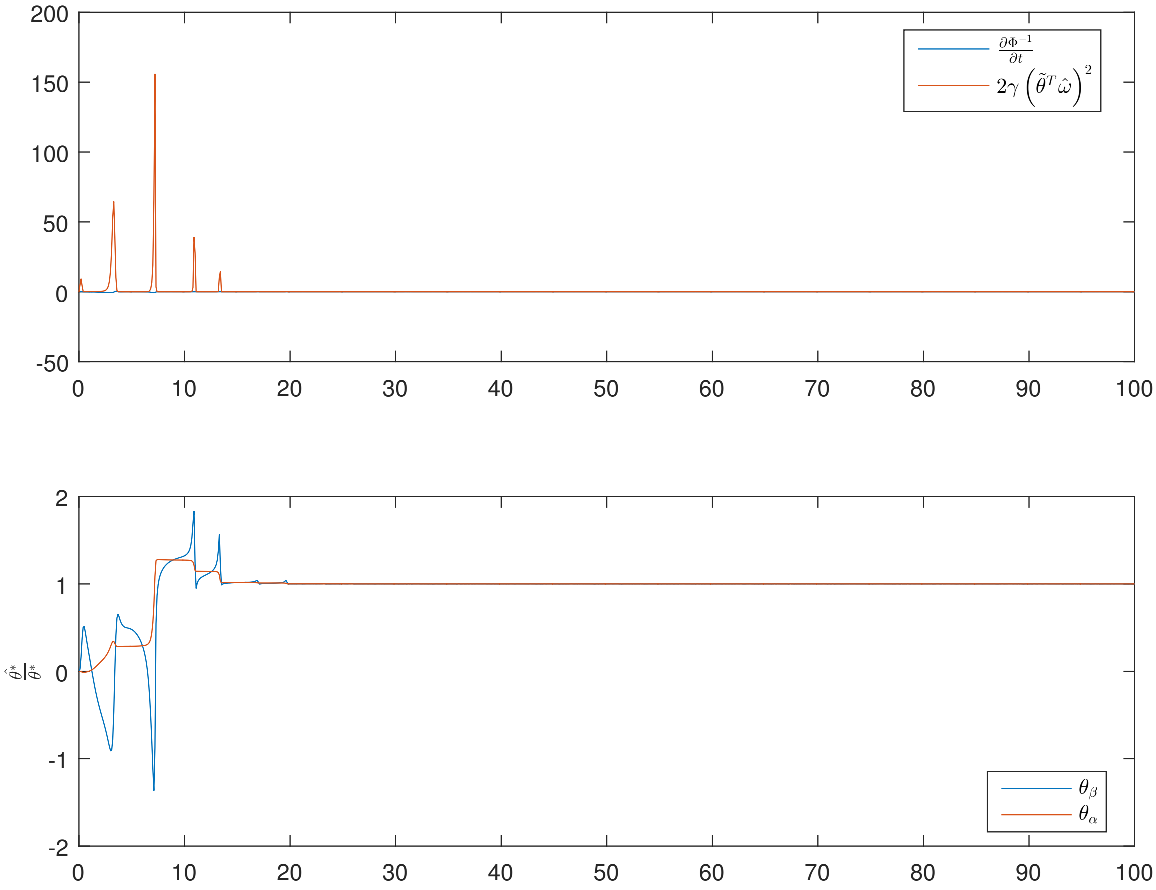

Figure 4-17: Lyapunov stability terms and parameter convergence for a second-order SISO system.

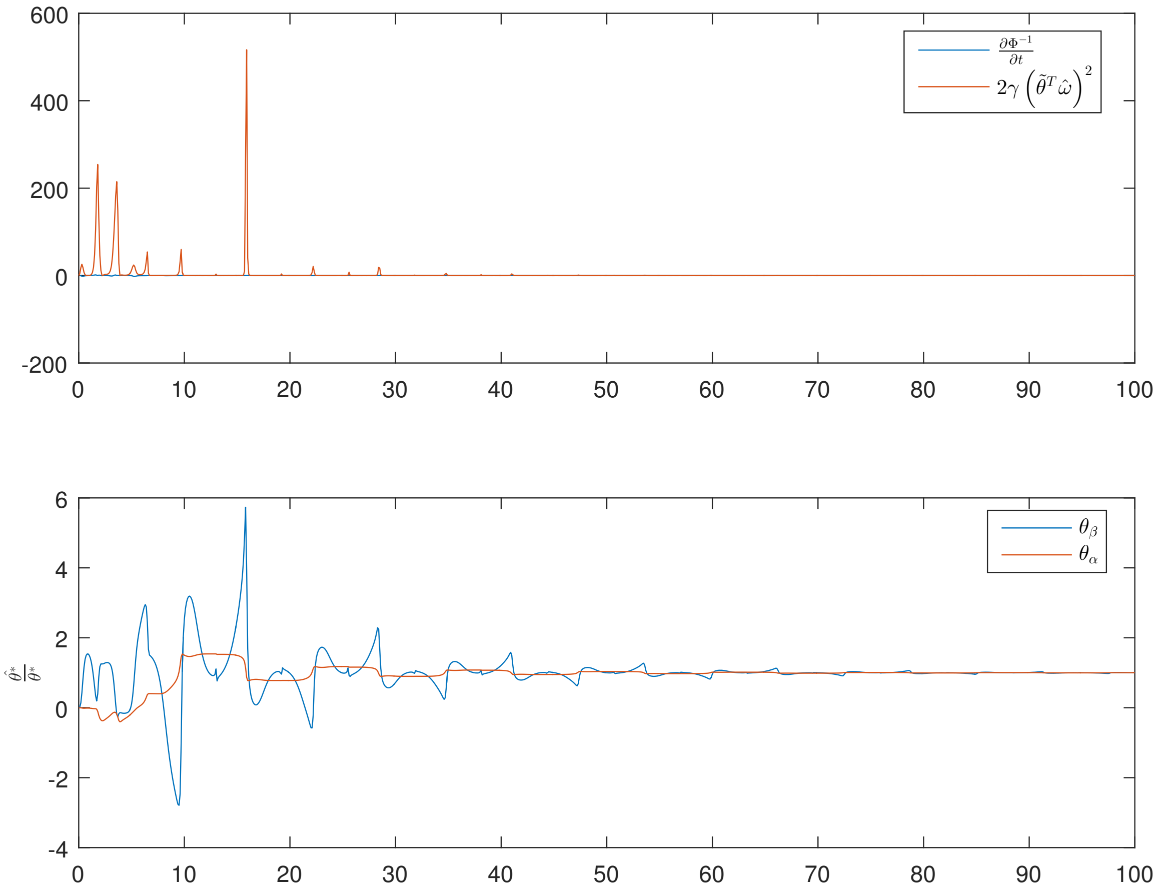

Figure 4-18: Lyapunov stability terms and parameter convergence for a third-order SISO system.

Alternative Lumped Parameter Learning Options

In addition to the novel Jacobian application to the adaptive observer form described in literature [37], other means of limited learning were considered for the purpose of estimating the subset of non-minimal parameters for the full system. One such way is that of projection [22], which defines a set, $\mathcal{S}$, containing the parameters, θ, constrained by a function, $g(\theta) = 0$, such that,

$$\mathcal{S} = \{\theta \in \mathbb{R}^n | g(\theta) = 0\} \tag{4.172}$$

The constraint function, $g(\theta) = 0$, must be differentiable, and the learning on the estimated parameters, $\hat{\theta}$, is then projected onto the subspace in which the parameters, θ, are constrained, by subtracting off the learning orthogonal to that space. This is shown in Equation (4.173).

$$\dot{\hat{\theta}} = -\Gamma\omega^\top e + \Gamma\frac{\nabla g \nabla g^\top}{\nabla g^\top \Gamma \nabla g}\Gamma\omega^\top e \tag{4.173}$$

This method was not chosen for implementation for two reasons. First, the function, $g(\theta) = 0$, is not readily defined for the problem outlined, and second, the learning that is orthogonal to the projected space is still valid, but should only operate on the gradient of steepest descent of the subset of parameters, θ^*. Instead, all parameters are updated, but only in such a way that is consistent with $g(\theta) = 0$.

Another approach is that of nonlinear parameterization [2] [9], which consists of defining a dynamic equation as a nonlinear function of parameters. Namely, the dynamics of the output estimate, $\dot{\hat{y}}$, are a function of a parameter set, $\alpha(y, u)$, and a nonlinear function, $f(\hat{\theta}, \omega)$ of the parameters, $\hat{\theta}$. The plant dynamics appear in the form,

$$\dot{y} = -\alpha(y, u)y + f\left(\theta_0, \omega(y, u)\right) \tag{4.174}$$

The algorithm employed to control this system is called Min-Max Parameter Estimation [9]. This is achieved by implementing a saturation of a ratio of the error, $\tilde{y}$, and an arbitrary positive number, ϵ; as well as the result of an optimization problem.

$$\begin{aligned} \dot{\hat{y}} &= -\alpha(y, u)\left(\hat{y} - \epsilon\text{sat}\left(\frac{\tilde{y}}{\epsilon}\right)\right) + f(\hat{\theta}, \omega) - a^*\text{sat}\left(\frac{\tilde{y}}{\epsilon}\right) \\ \dot{\hat{\theta}} &= -\tilde{y}_\epsilon \phi^* \end{aligned} \tag{4.175}$$

where the solutions to a^* and ϕ^* are derived from optimizing $g(\theta, \omega, \phi)$, such that,

$$\begin{aligned} a^* &= \min_{\phi \in \mathbb{R}^m} \max_{\theta \in \Omega^0} g(\theta, \omega, \phi) \\ \phi^* &= \arg \min_{\phi \in \mathbb{R}^m} \max_{\theta \in \Omega^0} g(\theta, \omega, \phi) \\ g(\theta, \omega, \phi) &= \text{sat}\left(\frac{\tilde{y}}{\epsilon}\right)\left(f(\hat{\theta}, \omega) - f(\theta, \omega) - \phi^{*\top}(\hat{\theta} - \theta)\right) \end{aligned} \tag{4.176}$$

The resulting parameters of this method rely on a convex function, $f(\theta_0, \omega)$, and there is no guarantee of convexity in the problem proposed, when generalized to any known construction of a matrix given a subset of parameters. It will be observed that the proposed method also suffers from convergence to a local minimum, but this can be overcome through heuristic choice of initial conditions.

Extension to Multiple Input, Single Output System

The results of the previous section will now be extended to a multiple input, single output system, with a dynamical system described by,

$$\begin{aligned} \dot{x} &= \alpha A x + \beta B u \\ y &= C^{\top} x \end{aligned} \tag{4.177}$$

where $A \in \mathbb{R}^{q \times q}$, $B \in \mathbb{R}^{q \times n}$, and $C \in \mathbb{R}^{q}$; for $u \in \mathbb{R}^{n}$ and $y \in \mathbb{R}$. The transfer function of this system can be shown to be,

$$\begin{aligned} Y(s) =& \frac{\beta b_{p,1,1} s^{q-1} + \beta\alpha b_{p,1,2} s^{q-2} + \ldots + \beta\alpha^{q-1} b_{p,1,q}}{s^{q} + \alpha a_{p,1,1} s^{q-1} + \ldots + \alpha^{q} a_{p,1,q}} U_1(s) \\ &+ \ldots + \frac{\beta b_{p,n,1} s^{q-1} + \beta\alpha b_{p,n,2} s^{q-2} + \ldots + \beta\alpha^{q-1} b_{p,n,q}}{s^{q} + \alpha a_{p,n,1} s^{q-1} + \ldots + \alpha^{q} a_{p,n,q}} U_n(s) \end{aligned} \tag{4.178}$$

where $a_{p,i,k}$ and $b_{p,i,k}$ are known coefficients of the transfer function for A, B, and C; and α and β are unknown parameters. The full system transfer function can be succinctly written as,

$$Y(s) = \sum_{i=1}^{n} G_i(s) U_i(s) \tag{4.179}$$

where $G_i(s)$ is the transfer function pertaining to the i^{th} input, $U_i(s)$. The observer construction begins by choosing an asymptotically stable filter, F, as,

$$F = \begin{bmatrix} 0 & 1 & \ldots & 0 \\ \vdots & \vdots & \ddots & \vdots \\ 0 & 0 & \ldots & 1 \\ -a_{f,k} & -a_{f,k-1} & \ldots & -a_{f,1} \end{bmatrix} \tag{4.180}$$

and an input vector, g,

$$g = \begin{bmatrix} 0 & \cdots & 0 & 1 \end{bmatrix}^\top \tag{4.181}$$

The dynamics of the regressors are then defined as,

$$\begin{aligned} \dot{\omega}_{u,1} &= F\omega_{u,1} + gu_1 \\ &\vdots \\ \dot{\omega}_{u,n} &= F\omega_{u,n} + gu_n \\ \dot{\omega}_y &= F\omega_y + gy \end{aligned} \tag{4.182}$$

and an output, y, is constructed as,

$$y = \theta^\top \begin{bmatrix} \omega_{u,1} \\ \vdots \\ \omega_{u,n} \\ \omega_y \end{bmatrix} \tag{4.183}$$

The parameters of the system are then defined as,

$$\theta = \\ \begin{bmatrix} b_{u,1,k} & \cdots & b_{u,1,1} & b_{u,2,k} & \cdots & b_{u,i,j} & \cdots & b_{u,n,1} & b_{y,k} & \cdots & b_{y,1} \end{bmatrix}^\top \tag{4.184}$$

The parameters, θ, of the q^{th} order system with n inputs can also be described in terms of the subset of parameters, $\theta^{*} = [\theta_\beta, \theta_\alpha]^\top$, such that,

$$\theta = \begin{bmatrix} \frac{\theta_\beta}{b_{p,1,1}} \left(\frac{a_{f,1} - \theta_\alpha}{a_{p,1}} \right)^{q-1} b_{p,1,q} \\ \vdots \\ \frac{\theta_\beta}{b_{p,1,1}} \left(\frac{a_{f,1} - \theta_\alpha}{a_{p,1}} \right) b_{p,1,2} \\ \theta_\beta \\ \frac{\theta_\beta}{b_{p,1,1}} \left(\frac{a_{f,1} - \theta_\alpha}{a_{p,1}} \right)^{q-1} b_{p,2,q} \\ \vdots \\ \frac{\theta_\beta}{b_{p,1,1}} \left(\frac{a_{f,1} - \theta_\alpha}{a_{p,1}} \right) b_{p,n,2} \\ \theta_\beta \frac{b_{p,n,1}}{b_{p,1,1}} \\ a_{f,q} - \left(\frac{a_{f,1} - \theta_\alpha}{a_{p,1}} \right)^{q} a_{p,q} \\ \vdots \\ a_{f,2} - \left(\frac{a_{f,1} - \theta_\alpha}{a_{p,1}} \right)^{2} a_{p,2} \\ \theta_\alpha \end{bmatrix} \tag{4.185}$$

The Jacobian, J, is then defined as,

$$J = \frac{\partial \theta}{\partial \theta^{*}} = \begin{bmatrix} \frac{b_{p,1,q}}{b_{p,1,1}} \left(\frac{a_{f,1} - \theta_\alpha}{a_{p,1}} \right)^{q-1} & -(q-1) \frac{b_{p,1,q}\theta_\beta}{b_{p,1,1}a_{p,1}} \left(\frac{a_{f,1} - \theta_\alpha}{a_{p,1}} \right)^{q-2} \\ \vdots & \vdots \\ \frac{b_{p,1,2}}{b_{p,1,1}} \left(\frac{a_{f,1} - \theta_\alpha}{a_{p,1}} \right) & -\frac{b_{p,1,2}}{b_{p,1,1}a_{p,1}} \theta_\beta \\ 1 & 0 \\ \frac{b_{p,2,q}}{b_{p,1,1}} \left(\frac{a_{f,1} - \theta_\alpha}{a_{p,1}} \right)^{q-1} & -(q-1) \frac{b_{p,2,q}\theta_\beta}{b_{p,1,1}a_{p,1}} \left(\frac{a_{f,1} - \theta_\alpha}{a_{p,1}} \right)^{q-2} \\ \vdots & \vdots \\ \frac{b_{p,q,2}}{b_{p,1,1}} \left(\frac{a_{f,1} - \theta_\alpha}{a_{p,1}} \right) & -\frac{b_{p,q,2}}{b_{p,1,1}a_{p,1}} \theta_\beta \\ \frac{b_{p,2,1}}{b_{p,1,1}} & 0 \\ 0 & q \frac{a_{p,q}}{a_{p,1}} \left(\frac{a_{f,1} - \theta_\alpha}{a_{p,1}} \right)^{q-1} \\ \vdots & \vdots \\ 0 & 2 \frac{a_{p,2}}{a_{p,1}} \left(\frac{a_{f,1} - \theta_\alpha}{a_{p,1}} \right) \\ 0 & 1 \end{bmatrix} \tag{4.186}$$

The update law is the same then as in Equation (4.154), such that,

$$\dot{\hat{\theta}}^{*} = -\gamma \mathrm{J}^{\top} \hat{\omega} e \tag{4.187}$$

This construction was tested with a third-order MISO system, as shown in Figure 4-19, showing rapid convergence of the parameters. Figure 4-20 shows the stability criteria of the system.

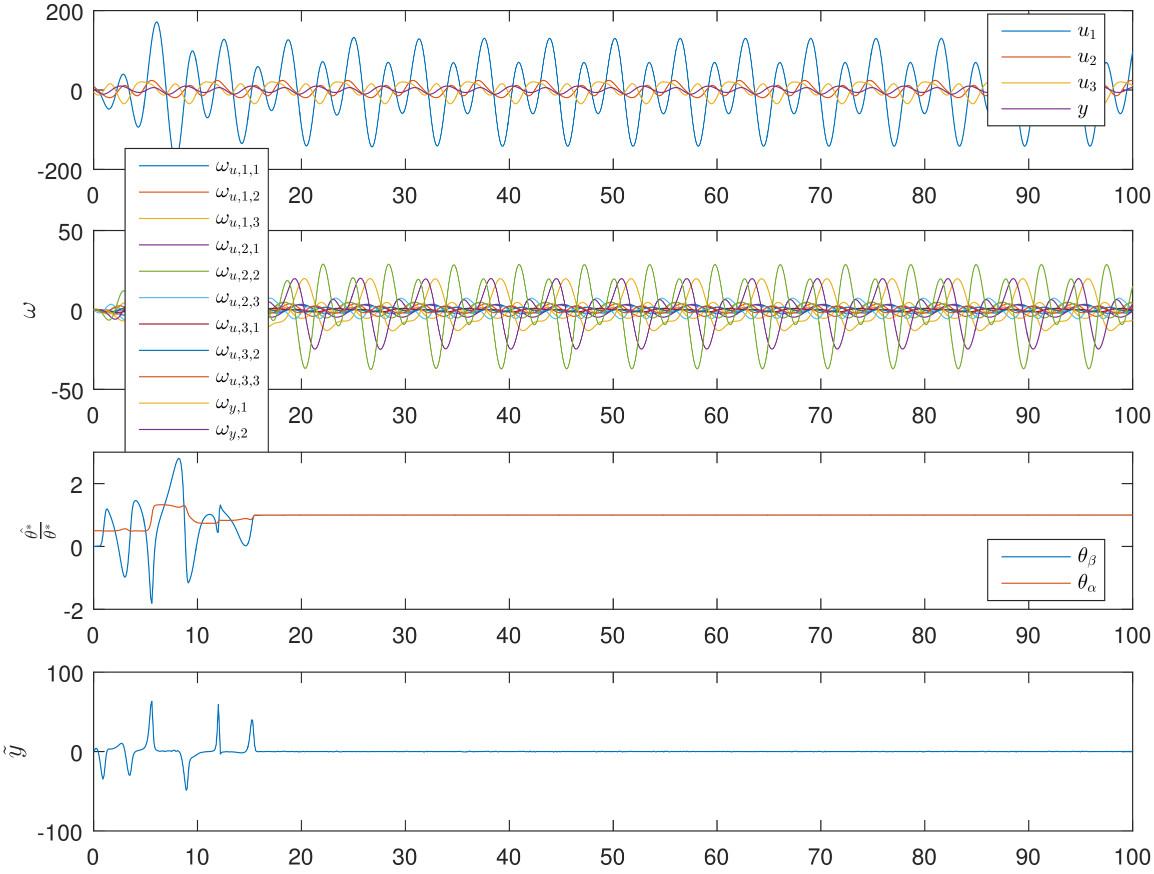

Figure 4-19: Test case for third-order MISO plant showing inputs, $u(t)$; outputs, $y(t)$; regressors, ω; and the convergence of the parameter subset, $\hat{\theta}^*$, comprised of $\hat{\theta}_\beta$ and $\hat{\theta}_\alpha$.

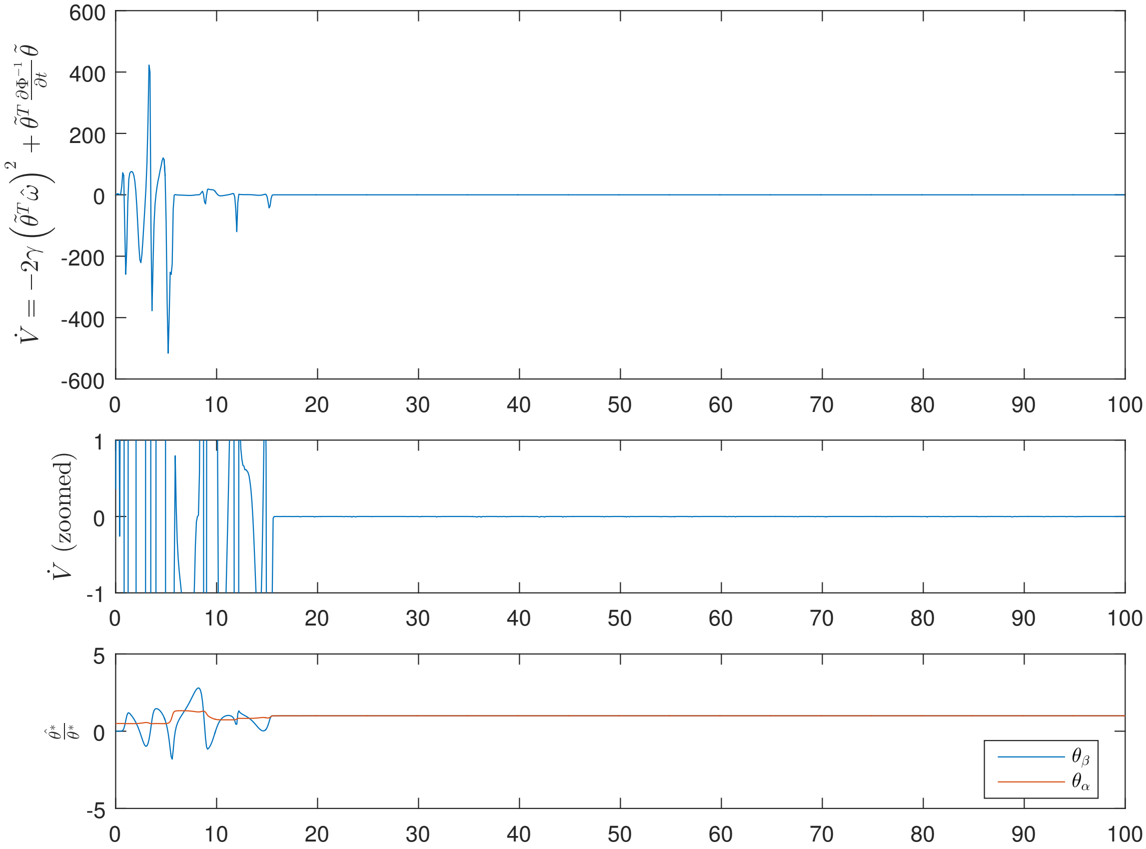

Figure 4-20: Lyapunov stability terms and parameter convergence for a third-order MISO system.

Extension to Multiple Input, Multiple Output System

The next iteration of the observer is to apply the system to a multiple input, multiple output system, such as,

$$\begin{aligned} \dot{x} &= \alpha A x + \beta B u \\ y &= C^\top x \end{aligned} \tag{4.188}$$

where $A \in \mathbb{R}^{q\times q}$, $B \in \mathbb{R}^{q\times n}$, and $C \in \mathbb{R}^{q\times m}$; for $u \in \mathbb{R}^n$ and $y \in \mathbb{R}^m$. Each output channel, $Y_j(s)$, has a transfer function defined as,

$$\begin{aligned} Y_j(s) =& \frac{\beta b_{p,1,j,1}s^{q-1} + \beta\alpha b_{p,1,j,2}s^{q-2} + \ldots + \beta\alpha^{q-1}b_{p,1,j,q}}{s^k + \alpha a_{p,1,j,1}s^{q-1} + \ldots + \alpha^q a_{p,1,j,q}}U_1(s) \\ &+ \ldots + \frac{\beta b_{p,n,j,1}s^{q-1} + \beta\alpha b_{p,n,j,2}s^{q-2} + \ldots + \beta\alpha^{q-1}b_{p,n,j,q}}{s^q + \alpha a_{p,n,j,1}s^{q-1} + \ldots + \alpha^q a_{p,n,j,q}}U_n(s) \end{aligned} \tag{4.189}$$

This expression can be succinctly written as,

$$Y_j(s) = \sum_{i=1}^{n} G_{i,j}(s)U_i(s) \tag{4.190}$$

for $j \in [1 \cdots m]$. The dynamics of the regressors are defined as,

$$\begin{aligned} \dot{\omega}_{u,1} &= F\omega_{u,1} + gu_1 \\ &\vdots \\ \dot{\omega}_{u,n} &= F\omega_{u,n} + gu_n \\ \dot{\omega}_{y,1} &= F\omega_{y,1} + gy_1 \\ &\vdots \\ \dot{\omega}_{y,m} &= F\omega_{y,m} + gy_m \end{aligned} \tag{4.191}$$

and an equivalent output, y_j, for each output, j, is defined as,

$$y_j = \theta_j^\top \begin{bmatrix} \omega_{u,1} \\ \vdots \\ \omega_{u,n} \\ \omega_{y,j} \end{bmatrix} \tag{4.192}$$

The parameters, θ_j, for the output channel, j, are defined as,

$$\theta_j = \begin{bmatrix} b_{u,1,j,k} & \cdots & b_{u,1,j,1} & b_{u,2,j,k} & \cdots & b_{u,n,j,1} & b_{y,j,k} & \cdots & b_{y,j,1} \end{bmatrix}^\top \tag{4.193}$$

An estimated system, $\widehat{Y} = \operatorname{diag}\left(\widehat{\Theta}^\top \widehat{\Omega}\right)$ generates an error vector, E, such that,

$$E = \operatorname{diag}\left(\widehat{\Theta}^\top \widehat{\Omega}\right) - Y \tag{4.194}$$

where the parameter matrix, $\widehat{\Theta}$, is defined as,

$$\widehat{\Theta} = \begin{bmatrix} \hat{\theta}_1 & \cdots & \hat{\theta}_m \end{bmatrix} \tag{4.195}$$

and the regressor matrix, $\widehat{\Omega}$, as,

$$\widehat{\Omega} = \left[\begin{array}{ccc} \hat{\omega}_1 & \cdots & \hat{\omega}_m \end{array} \right] \tag{4.196}$$

The update law for the subset of parameters, $\hat{\theta}^*$, is defined as,

$$\dot{\hat{\theta}}^* = -\gamma \mathbf{J}^\top \underline{\widehat{\Omega}} E \tag{4.197}$$

where $\gamma > 0$, and the concatenated Jacobian, $\mathbf{J} \in \mathbb{R}^{mq(n+1)\times 2}$, is defined as,

$$\mathbf{J} = \left[\begin{array}{c} \mathrm{J}_1 \\ \vdots \\ \mathrm{J}_m \end{array} \right] \tag{4.198}$$

for $\mathrm{J}_j = \left.\frac{\partial \theta_j}{\partial \theta^*}\right|_{\theta^* = \hat{\theta}_j^*}$, as in Equation (4.186). Additionally, the regressor tensor, $\underline{\widehat{\Omega}} \in \mathbb{R}^{mq(n+1)\times m}$, is defined as,

$$\underline{\widehat{\Omega}} = \left[\begin{array}{ccc} \hat{\omega}_1 & \cdots & 0 \\ \vdots & \ddots & \vdots \\ 0 & \cdots & \hat{\omega}_m \end{array} \right] \tag{4.199}$$

A simulation of this formulation was conducted, and results showing two salient points can be scene in Figures 4-21 and 4-22. In Figure 4-21, initial conditions were chosen such that no prior knowledge of the parameters were assumed. It can be seen that the observer enters a local minimum with error entering a marginally stable state. It was noted, however, that when the initial conditions were started arbitrarily high, the system would avoid local minima, and converge to the true parameters. This is shown in Figure 4-22, with initial conditions at 500% their true values, and rapid parameter convergence is observed.

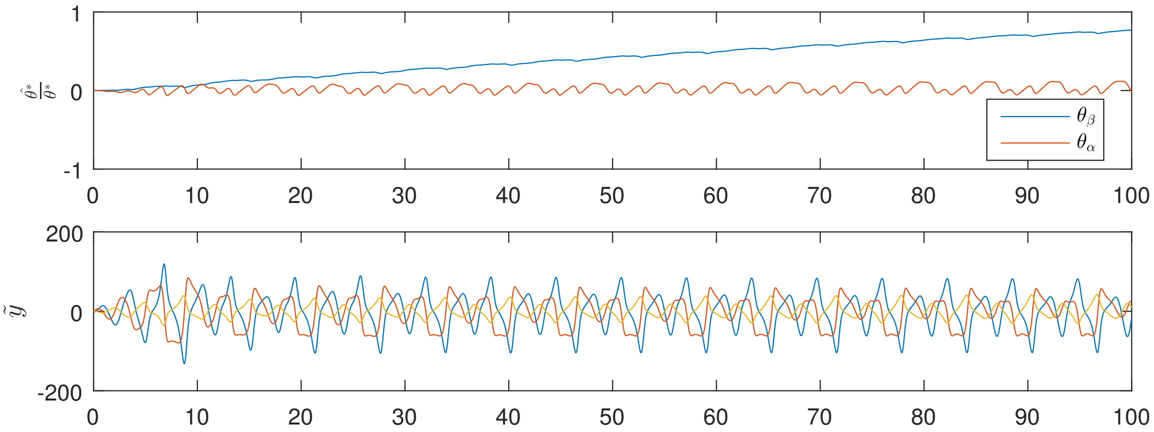

Figure 4-21: Test case for a third-order MIMO plant showing the convergence of the parameter subset, $\hat{\theta}^*$, comprised of $\hat{\theta}_\beta$ and $\hat{\theta}_\alpha$; and the error output, $\tilde{y}_j$. The parameters were initialized to $\hat{\theta}^*_0 = 0$.

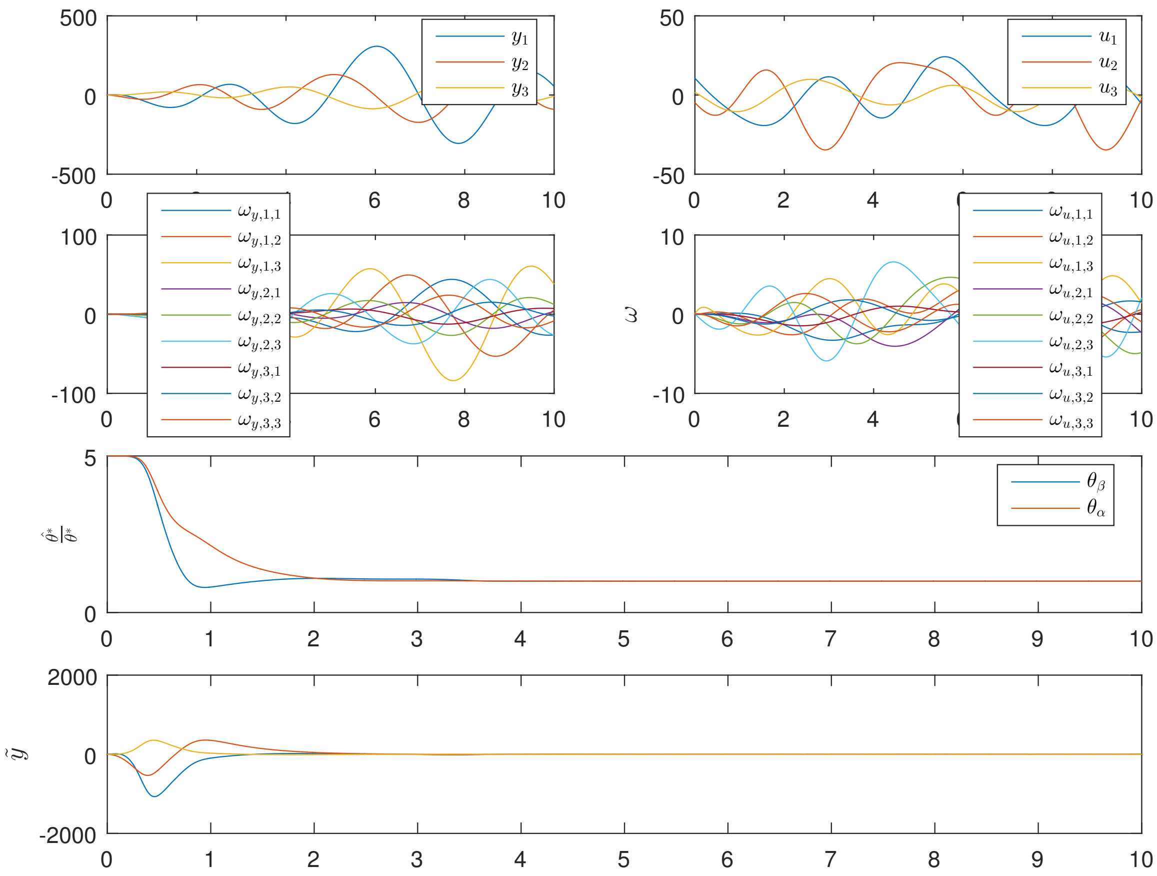

Figure 4-22: Test case for a third-order MIMO plant showing the convergence of the parameter subset, $\hat{\theta}^*$, comprised of $\hat{\theta}_\beta$ and $\hat{\theta}_\alpha$; and the error output, $\tilde{y}_j$. The parameters were initialized to $\hat{\theta}^*_0 = 5\theta^*$.

Extension to Multiple Constant System

The final test case of this observer composition is that of the multiple-constant case, for a system,

$$\begin{aligned} \dot{x} &= \bar{\alpha} A x + \bar{\beta} B u \\ y &= C^{\top} x \end{aligned} \tag{4.200}$$

where $A \in \mathbb{R}^{q\times q}$, is defined as, $B \in \mathbb{R}^{q\times n}$, and $C \in \mathbb{R}^{q\times m}$; for $u \in \mathbb{R}^n$ and $y \in \mathbb{R}^m$. To determine the relationship of the subset of parameters to the full set, a transfer function must be determined between the input and output channels. First, a SISO system is used as an example, but can be generalized to an m output, n input MIMO system. This SISO takes the form,

$$A = \begin{bmatrix} a_{11} & a_{12} & a_{13} \\ a_{21} & a_{22} & a_{23} \\ a_{31} & a_{32} & a_{33} \end{bmatrix} \quad B = \begin{bmatrix} b_1 \\ b_2 \\ b_3 \end{bmatrix} \quad C = \begin{bmatrix} 1 & 0 & 0 \end{bmatrix} \tag{4.201}$$

and the coefficient matrices, $\bar{\alpha}$ and $\bar{\beta}$ are defined as,

$$\bar{\alpha} = \begin{bmatrix} \alpha_1 & 0 & 0 \\ 0 & \alpha_2 & 0 \\ 0 & 0 & \alpha_3 \end{bmatrix} \quad \bar{\beta} = \begin{bmatrix} \beta_1 & 0 & 0 \\ 0 & \beta_2 & 0 \\ 0 & 0 & \beta_3 \end{bmatrix} \tag{4.202}$$

The transfer function can be defined as,

$$\frac{Y(s)}{U(s)} = \frac{P(s)}{Q(s)} \tag{4.203}$$

with the numerator, $P(s)$,

$$\begin{aligned} P(s) = (\beta_1 b_1)s^2 &+ (-\beta_1 b_1 \alpha_3 (a_{33} + a_{22}) + \beta_2 b_2 (\alpha_1 a_{12}) + \beta_3 b_3 (\alpha_1 a_{13}))s \\ &+ (\beta_1 b_1 \alpha_2 \alpha_3 (a_{22} a_{33} - a_{23} a_{32}) + \beta_2 b_2 \alpha_1 \alpha_3 (a_{13} a_{32} - a_{12} a_{33}) \\ &+ \beta_3 b_3 \alpha_1 \alpha_2 (a_{12} a_{23} - a_{13} a_{22})) \end{aligned} \tag{4.204}$$

and the denominator, $Q(s)$,

$$\begin{aligned}Q(s) = s^3 &- (\alpha_1 a_{11} + \alpha_2 a_{22} + \alpha_3 a_{33})\, s^2 + (\alpha_1\alpha_2(a_{11}a_{22} - a_{12}a_{21}) \\ &+ \alpha_1\alpha_3(a_{11}a_{33} - a_{13}a_{31}) + \alpha_2\alpha_3(a_{22}a_{33} - a_{23}a_{32}))s \\ &+ \alpha_1\alpha_2\alpha_3(-a_{11}(a_{22}a_{33} - a_{23}a_{32}) + a_{12}(a_{21}a_{33} - a_{23}a_{31}) \\ &- a_{13}(a_{21}a_{32} - a_{22}a_{31}))\end{aligned} \tag{4.205}$$

It is noted that the elegant solution of Equation (4.135) no longer emerges, and instead, the transfer function form is dependent on the order. This can be achieved in a recursive means, but an alternative method is proposed below. The filter, F, of the equivalent system are again defined by,

$$F = \begin{bmatrix} 0 & 1 & \dots & 0 \\ \vdots & \vdots & \ddots & \vdots \\ 0 & 0 & \dots & 1 \\ -a_{f,q} & -a_{f,q-1} & \dots & -a_{f,1} \end{bmatrix} \tag{4.206}$$

and an input vector, g,

$$g = \begin{bmatrix} 0 & \cdots & 0 & 1 \end{bmatrix}^\top \tag{4.207}$$

The regressor dynamics are defined as,

$$\begin{aligned}\dot{\omega}_{u,1} &= F\omega_{u,1} + gu_1 \\ &\vdots \\ \dot{\omega}_{u,n} &= F\omega_{u,n} + gu_n \\ \dot{\omega}_{y,1} &= F\omega_{y,1} + gy_1 \\ &\vdots \\ \dot{\omega}_{y,m} &= F\omega_{y,m} + gy_m\end{aligned} \tag{4.208}$$

with an output, y_j, defined as,

$$y_j = \theta_j^\top \begin{bmatrix} \omega_{u,1} \\ \vdots \\ \omega_{u,n} \\ \omega_{y,j} \end{bmatrix} \tag{4.209}$$

The parameters, θ_j, are notationally defined as,

$$\theta_j = \begin{bmatrix} b_{u,1,j,q} & \cdots & b_{u,1,j,1} & b_{u,2,j,q} & \cdots & b_{u,n,j,1} & b_{y,j,q} & \cdots & b_{y,j,1} \end{bmatrix}^\top \tag{4.210}$$

The equivalent system is alternatively defined as,

$$\begin{aligned} \dot{\hat{x}} &= \hat{\bar{\alpha}} A \hat{x} + \hat{\bar{\beta}} B u \\ \hat{y} &= C \hat{x} \end{aligned} \tag{4.211}$$

where the subset of parameters, $\hat{\theta}^*$, are comprised of the coefficients of $\hat{\bar{\alpha}}$ and $\hat{\bar{\beta}}$. An estimated transfer function, $\widehat{G}_{i,j}(s)$, is then defined as,

$$\widehat{G}_{i,j}(s) = C_j (s\mathrm{I} - \hat{\bar{\alpha}} A)^{-1} \hat{\bar{\beta}} B_i = \frac{\hat{b}_{i,j,1} s^{q-1} + \cdots + \hat{b}_{i,j,q}}{s^q + \hat{a}_{j,1} s^{q-1} + \cdots + \hat{a}_{j,q}} \tag{4.212}$$

Using this transfer function, a full output channel, $\widehat{Y}_j$, is defined as,

$$\widehat{Y}_j(s) = \sum_{i=1}^{n} \widehat{G}_{i,j}(s) U_i(s) \tag{4.213}$$

for $j = [1 \cdots m]$. The estimated parameters, $\hat{\theta}_j$, are then defined as,

$$\begin{aligned} &\hat{\theta}_j = \\ &\begin{bmatrix} \hat{b}_{1,j,q} & \cdots & \hat{b}_{1,j,1} & \hat{b}_{2,j,q} & \cdots & \hat{b}_{n,j,1} & a_{f,q} - \hat{a}_{j,q} & \cdots & a_{f,1} - \hat{a}_{j,1} \end{bmatrix}^\top \end{aligned} \tag{4.214}$$

where $\hat{b}_{i,j,k}$ and $\hat{a}_{i,j,k}$ are defined as in Equation (4.212), $a_{f,k}$ are the coefficients of the filter, F. The Jacobian, J_j, for each output channel, j, can be constructed as,

$$J_j = \begin{bmatrix} \left.\frac{\partial\theta_j}{\partial\beta_1}\right|_{\beta_1=\hat{\beta}_1} & \cdots & \left.\frac{\partial\theta_j}{\partial\beta_q}\right|_{\beta_q=\hat{\beta}_q} & \left.\frac{\partial\theta_j}{\partial\alpha_1}\right|_{\alpha_1=\hat{\alpha}_1} & \cdots & \left.\frac{\partial\theta_j}{\partial\alpha_q}\right|_{\alpha_q=\hat{\alpha}_q} \end{bmatrix} \tag{4.215}$$

The Jacobian can be explicitly defined, as previously with Equation (4.193), however, the Jacobian must be defined separately for any q states or definition of unknown parameters. Therefore, in the interest of generality, a numerically perturbed Jacobian is used, defined by,

$$\begin{aligned} \left.\frac{\partial\theta_j}{\partial\beta_k}\right|_{\beta_k=\hat{\beta}_k} &\approx \frac{1}{\Delta x}\left(\theta_j|_{\beta_k=\hat{\beta}_k+\Delta x} - \theta_j|_{\beta_k=\hat{\beta}_k}\right) \\ \left.\frac{\partial\theta_j}{\partial\alpha_k}\right|_{\alpha_k=\hat{\alpha}_k} &\approx \frac{1}{\Delta x}\left(\theta_j|_{\alpha_k=\hat{\alpha}_k+\Delta x} - \theta_j|_{\alpha_k=\hat{\alpha}_k}\right) \end{aligned} \tag{4.216}$$

for $k \in [1 \cdots q]$. This is achieved by finding the first order difference of the parameter function, where the step size was chosen as $\Delta x = 1e-6$. Finally, the update law is defined similarly as,

$$\dot{\hat{\theta}}^* = -\gamma \mathbf{J}^\top \underline{\widehat{\Omega}} E \tag{4.217}$$

with $\mathbf{J}$ defined as in Equation (4.198), and $\underline{\widehat{\Omega}}$ defined as in Equation (4.199). This observer was simulated using the inputs and outputs, and subsequently the regressors shown in Figure 4-23. Figure 4-24 shows the rapid convergence for initial conditions

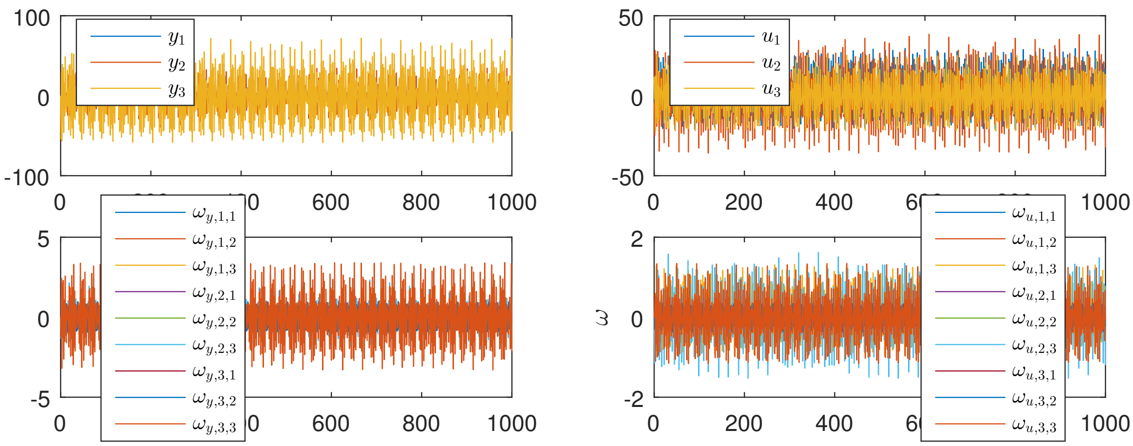

Figure 4-23: Simulated inputs, $u_i(t)$; outputs, $y_i(t)$ and their associated regressors, $\omega_{i,j,k}$.

set to $\hat{\theta}_0^* = 1.5\theta^*$. This is consistent with the results of Figure 4-22, which also show rapid convergence with higher initial conditons. Figure 4-25 shows the results of the parameter initial conditions, $\hat{\theta}_0^* = 0$. In both Figure 4-24 and 4-25, the top

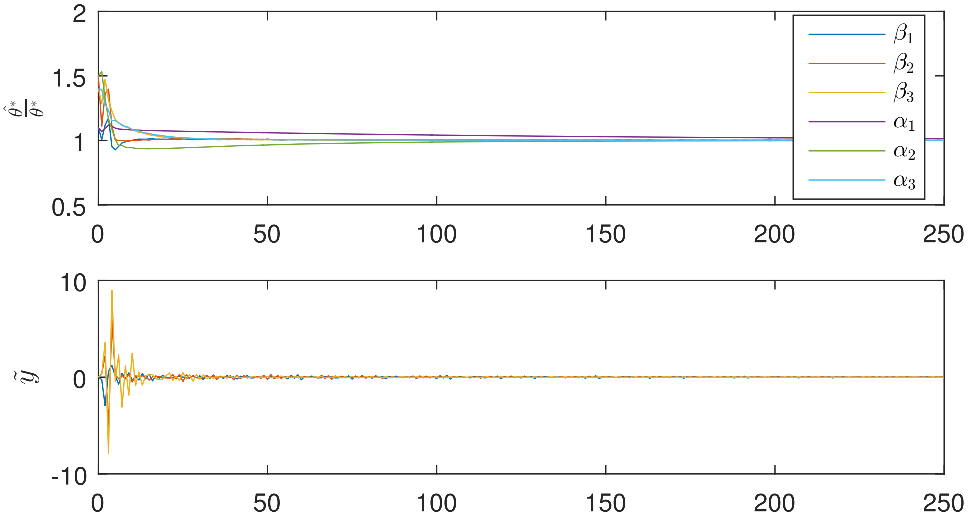

Figure 4-24: Jacobian observer MIMO, multi-constant system simulation, with $\hat{\theta}_0^* = 1.5\theta^*$, and inputs generated with a combination of cosine signals of varying frequencies.

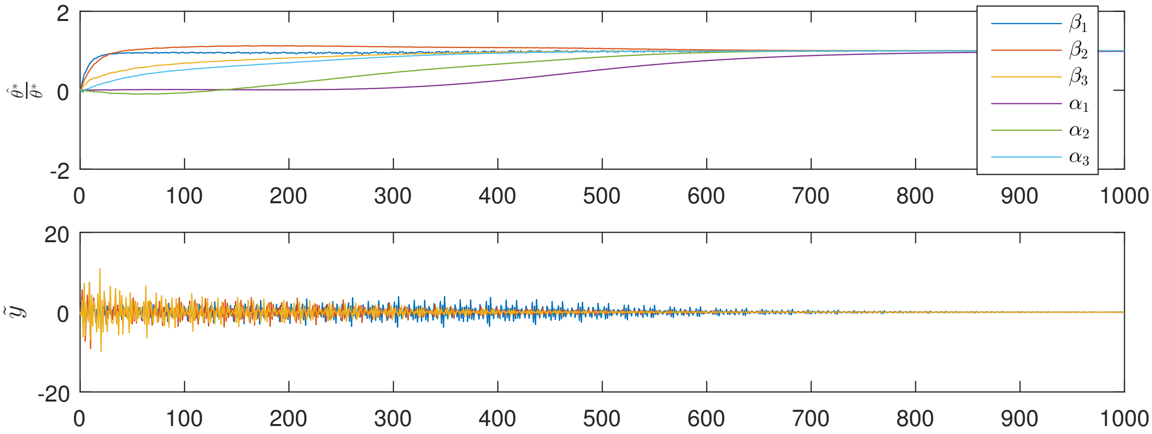

Figure 4-25: Jacobian observer MIMO, multi-constant system simulation, with $\hat{\theta}_0^* = 0$, and inputs generated with a combination of cosine signals of varying frequencies.

plot shows the normalized value of the parameter, $\hat{\theta}_i^*$, where a value of 1 indicates convergence. The bottom plots show the relative output error, $\tilde{y}$. These results show that the Jacobian adaptive observer also rapidly converges onto parameters with no a-priori knowledge, as consistent with Figure 4-21.

Application to the ANCF II Model

The next appropriate application is to a system akin to the electrolyte dynamics of Equation (3.157). For this purpose, a simulation of a linear basis electrolyte concentration, $\boldsymbol{c}_e^*$, will be fed through the Jacobian adaptive observer structure. This system assumes there is an invertible function of the electrolyte potential, $\boldsymbol{\phi}_e$, as shown in Figure 4-26.

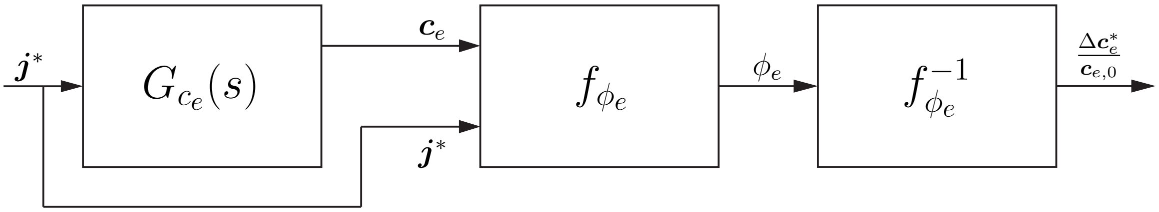

Figure 4-26: Block diagram of the electrolyte subsystem, assuming measurable inputs and outputs.

The system is defined by,

$$\begin{aligned} \dot{\boldsymbol{c}}_e^* &= A\boldsymbol{c}_e + B\gamma \boldsymbol{j}^* \\ \boldsymbol{c}_e^* &= C\boldsymbol{c}_e^* \end{aligned} \tag{4.218}$$

where γ is a known, scalar conditioning gain applied to the molar flux, $\boldsymbol{j}^*$. The system matrices: A, B, and C, are defined by,

$$A = \mathbf{M}_*^{-1}\mathbf{K}_* \tag{4.219}$$

for $A \in \mathbb{R}^{N\times N}$;

$$B = \gamma^{-1}\mathbf{M}_*^{-1}\mathbf{L}_* \tag{4.220}$$

for $B \in \mathbb{R}^{N\times N}$; and,

$$C = \mathrm{I} \tag{4.221}$$

for $C \in \mathbb{R}^{N\times N}$. The weight matrix, $\mathbf{M}_*$, as used in Equations (4.219) and (4.220) is constructed using an element matrix defined by,

$$\mathrm{M}^i = \int_0^1 \boldsymbol{v}_i \boldsymbol{v}_i^\top d\bar{x}_i \tag{4.222}$$

where the basis function, $\boldsymbol{v}_i$, is defined as in Equation (3.108). M^i is then broken into its individual components, such that,

$$\mathrm{M}^i = \begin{bmatrix} \mathrm{M}^i_{11} & \mathrm{M}^i_{12} \\ \mathrm{M}^i_{21} & \mathrm{M}^i_{22} \end{bmatrix} \tag{4.223}$$

Then the full matrix, $\mathbf{M}_*$, is defined as,

$$\mathbf{M}_* = \begin{bmatrix} \mathrm{M}^1_{11} & \mathrm{M}^1_{12} & & \\ \mathrm{M}^1_{21} & \mathrm{M}^1_{22} + \mathrm{M}^2_{11} & \mathrm{M}^2_{12} & \\ & \mathrm{M}^2_{21} & \ddots & \mathrm{M}^{N-1}_{12} \\ & & \mathrm{M}^{N-1}_{21} & \mathrm{M}^{N-1}_{22} \end{bmatrix} \tag{4.224}$$

Additionally, the stiffness matrix, $\mathbf{K}_*$, is constructed in a similar fashion, such that,

$$\begin{aligned} \mathrm{K}^i &= \int_0^1 \boldsymbol{v}_i \frac{d^2 \boldsymbol{v}_i^\top}{d\bar{x}_i^2} d\bar{x}_i \\ &= -\int_0^1 \frac{d\boldsymbol{v}_i}{d\bar{x}_i} \frac{d\boldsymbol{v}_i^\top}{d\bar{x}_i} d\bar{x}_i \end{aligned} \tag{4.225}$$

broken into its individual components,

$$\mathrm{K}^i = \begin{bmatrix} \mathrm{K}^i_{11} & \mathrm{K}^i_{12} \\ \mathrm{K}^i_{21} & \mathrm{K}^i_{22} \end{bmatrix} \tag{4.226}$$

The full stiffness matrix, $\mathbf{K}_*$, is then constructed as,

$$\mathbf{K}_* = \begin{bmatrix} \frac{D_{e,1}}{\left(l_1'\right)^2}\mathrm{K}_{11}^1 & \frac{D_{e,1}}{\left(l_1'\right)^2}\mathrm{K}_{12}^1 & & \\ \frac{D_{e,1}}{\left(l_1'\right)^2}\mathrm{K}_{21}^1 & \frac{D_{e,1}}{\left(l_1'\right)^2}\mathrm{K}_{22}^1 + \frac{D_{e,2}}{\left(l_2'\right)^2}\mathrm{K}_{11}^2 & \frac{D_{e,2}}{\left(l_2'\right)^2}\mathrm{K}_{12}^2 & \\ & \frac{D_{e,2}}{\left(l_2'\right)^2}\mathrm{K}_{21}^2 & \ddots & \frac{D_{e,N-1}}{\left(l_{N-1}'\right)^2}\mathrm{K}_{12}^{N-1} \\ & & \frac{D_{e,N-1}}{\left(l_{N-1}'\right)^2}\mathrm{K}_{21}^{N-1} & \frac{D_{e,N-1}}{\left(l_{N-1}'\right)^2}\mathrm{K}_{22}^{N-1} \end{bmatrix} \tag{4.227}$$

Finally, the input matrix, $\mathbf{L}_*$, uses the same matrix component, M^i, as in Equation (4.223), with no separator elements, such that,

$$\mathbf{L}_* = \bar{\beta} \begin{bmatrix} \mathrm{M}_{11}^1 & \mathrm{M}_{12}^1 & & & & \\ \mathrm{M}_{21}^1 & \mathrm{M}_{22}^1 + \mathrm{M}_{11}^2 & \mathrm{M}_{12}^2 & & & \\ & \mathrm{M}_{21}^2 & \mathrm{M}_{22}^2 & & & \\ & & & \mathrm{M}_{11}^4 & \mathrm{M}_{12}^4 & \\ & & & \mathrm{M}_{21}^4 & \mathrm{M}_{22}^4 + \mathrm{M}_{11}^5 & \mathrm{M}_{12}^5 \\ & & & & \mathrm{M}_{21}^5 & \mathrm{M}_{22}^5 \end{bmatrix} \tag{4.228}$$

for 2 elements in the anode, 1 element in the cathode and 2 elements in the separator. The input parameters, $\bar{\beta} \in \mathbb{R}^{N \times N}$, are defined as the diagonal matrix,

$$\bar{\beta} = \mathrm{diag}\left(\begin{bmatrix} \frac{t_a^0 a^-}{\epsilon_e^-} & \frac{t_a^0 a^-}{\epsilon_e^-} & \frac{t_a^0 a^-}{\epsilon_e^-} & \frac{t_a^0 a^+}{\epsilon_e^+} & \frac{t_a^0 a^+}{\epsilon_e^+} & \frac{t_a^0 a^+}{\epsilon_e^+} \end{bmatrix}^\top \right) \tag{4.229}$$

The separator element is not included in the $\mathbf{L}_*$ matrix because there are no flux induced dynamics in the separator, only diffusion.

The known portions of the system include M^i and K^i, while the unknown parameters from a BMS perspective are,

$$\theta^* = \begin{bmatrix} \frac{t_a^0 a^-}{\epsilon_e^-} & \frac{t_a^0 a^+}{\epsilon_e^+} & \frac{D_{e,-}}{\left(l_-'\right)^2} & \frac{D_{e,s}}{\left(l_s'\right)^2} & \frac{D_{e,+}}{\left(l_+'\right)^2} \end{bmatrix}^\top \tag{4.230}$$

It is assumed that each volume has its own static diffusion coefficient, which is used for elements within that electrode. Additionally, each volume has its own respective input coefficients. A Jacobian adaptive observer was constructed as prescribed earlier in Section 4.3.3, to estimate an unknown set of parameters, $\hat{\theta}^*$, using the update law,

$$\dot{\hat{\theta}}^* = -\Gamma(t)\mathbf{J}^\top \underline{\widehat{\Omega}} E \tag{4.231}$$

where the learning gain was chosen as,

$$\Gamma(t) = \begin{cases} 0 & t < t_l \\ 10 & t \geq t_l \end{cases} \tag{4.232}$$

The time-varying learning gain, $\Gamma(t)$, is defined as such to ensure the regressors are mostly converged onto their true values, $\tilde{\omega} \to 0$, by the learning time, t_l.

A persistently exciting signal representing the conditioned molar flux, $\gamma \boldsymbol{j}^*$, was applied, $U(t)$; with a normalized change in electrolyte concentration, $\frac{\Delta \boldsymbol{c}_e^*(t)}{\boldsymbol{c}_{e,0}^*}$, measured as the output, $Y(t)$. These signals are shown in Figure 4-27, with $\boldsymbol{c}_{e,0}^* = 1000$, for a duration of 1000 seconds. Figure 4-28 shows the resulting simulation when the unknown parameters were initialized to $\hat{\theta}_0^* = 1.5\theta^*$. Figure 4-29 shows the simulation results for an initialized parameter value of $\hat{\theta}_0^* = 0$. In both cases, learning was started at $t_l = 100\,\mathrm{s}$, at which point the parameters rapidly converge to their true values, normalized to a value of 1. It is noted that the separator parameters, $\widehat{\frac{D_{e,2}}{(l_2')^2}}$, converge the slowest in both cases, as the dynamics of the separator rely on diffusion characteristics to be observed.

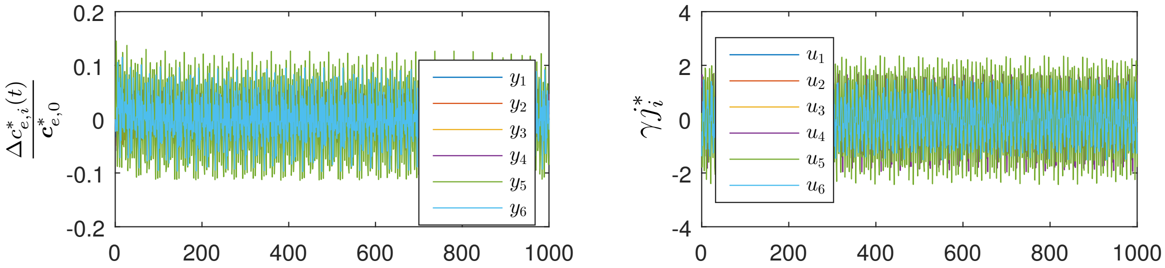

Figure 4-27: Inputs, $u_i(t)$; and outputs, $y_i(t)$, for the simulated electrolyte plant.

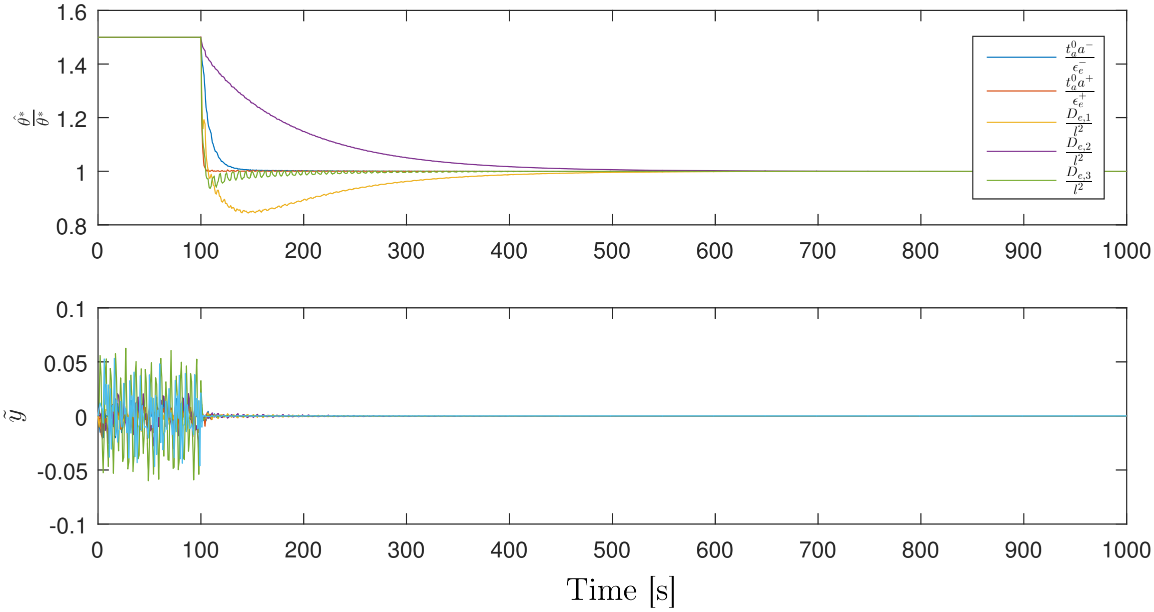

Figure 4-28: Jacobian observer for electrolyte plant, with $\hat{\theta}_0^* = 1.5\theta^*$. The adaptive learning is started at $t_l = 100\,\mathrm{s}$.

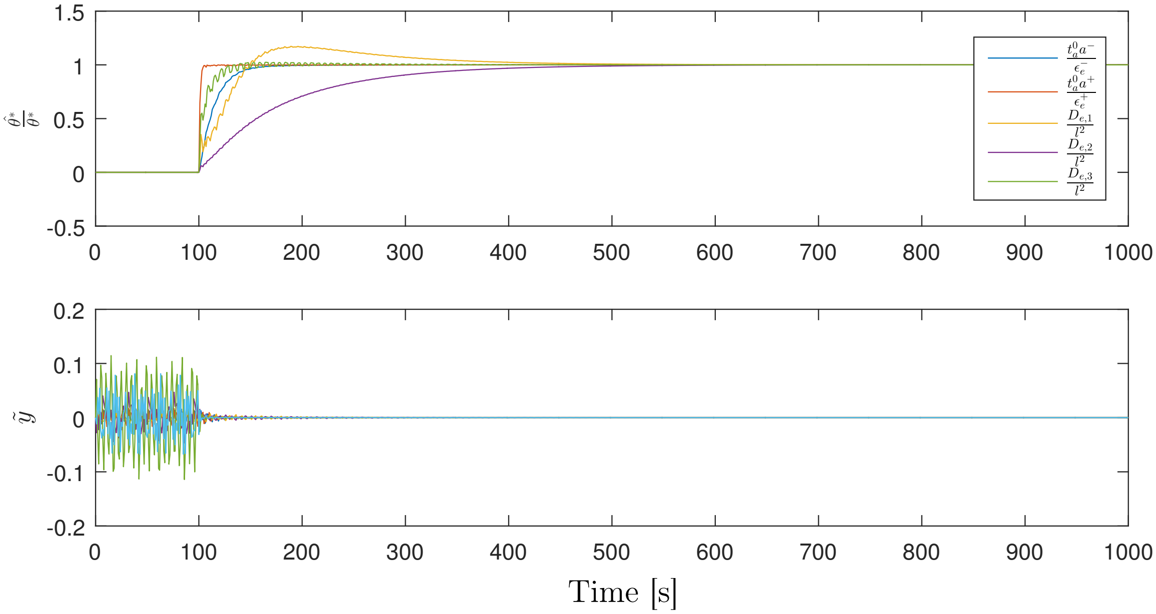

Figure 4-29: Jacobian observer for electrolyte plant, with $\hat{\theta}_0^* = 0$. The adaptive learning is started at $t_l = 100\,\mathrm{s}$.

4.4 Full Observer Construction and Challenges

The three observers described in Section 4.3 constitute the foundational framework for a BMS to be constructed using the ANCF II model structure. However, this endeavor only handles the spatiotemporal dynamics, with a method for determining the molar flux a-priori. This section will now discuss some approaches and difficulties of combining these observers into a complete structure. The difficulty in using higher order models is the mutual dependence of the output voltage on the solid potential, $\phi_s(x,t)$; the electrolyte potential, $\phi_e(x,t)$; the open-circuit potential, $\mathcal{U}(x,t)$; and ohmic losses, $R_f I(t)$. For the purposes of this section, ohmic losses are ignored, as they were in Chapter 3. Error in any of these terms may be masked by error in other terms, and therefore the system may have infinite solutions for a given output. The Butler-Volmer kinetics constrain this to a single set, allowing for the accurate evolution of concentration state dynamics. The inversion of these functions, and its application to the work discussed in Section 4.3.2, is addressed in Section 4.4.1. Figure 4-30 shows the notional full-scale observer. In this case, the plant model, $G_p(s,t)$, can be replaced by measurements from a battery cell. Section 4.3 describes the construction of the adaptive observers for the solid concentration, $G_{c_s}(s)$; the electrolyte concentration,

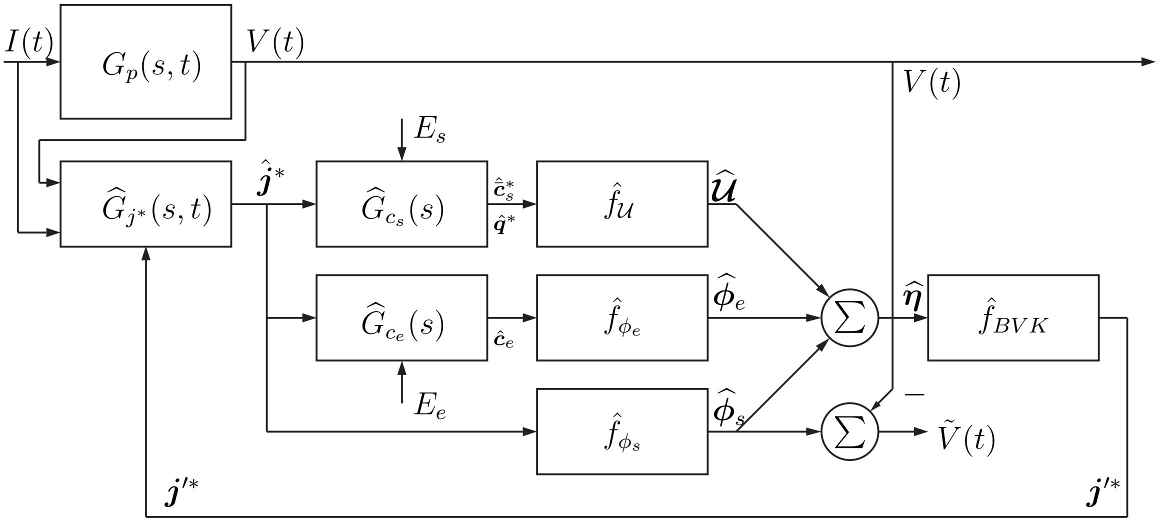

Figure 4-30: Block diagram of a notional full-scale observer using the adaptive observers constructed in Section 4.3. The plant model, $G_p(s,t)$, is theoretically replaced by a battery cell.

$G_{c_e}(s)$; and the a-priori flux plant, $G_{j^*}(s,t)$. For each of these, it was assumed that there was a completely invertible function of the contribution of the overpotential to each of these concentrations. Namely, that the error vectors, E_e and E_s, were perfectly accurate. However, this is not the case, and the sensitivity of the observers may vary as a function of input current and concentrations.

The problem is then determining how much of a calculated output voltage error is a function of each of the cell potentials. To minimize the set of possible solutions, the lithium concentrations can be constrained such that the total lithium in the cell remains constant. This has been achieved for the SPM [23] [35], but that model ignores variation in the electrolyte, and as such, the prescribed means of constraint are not directly applicable. Another method of overcoming this challenge is to implement a machine learning algorithm to determine the appropriate learning gains, Γ, of the observers. One approach to this is discussed in Section 4.4.2.

4.4.1 Nonlinear Butler-Volmer Kinetics Inversion

At any given time, there exists an estimate for the states representing the solid concentration, $\hat{\bar{\boldsymbol{c}}}^*_s(t)$ and $\hat{\boldsymbol{q}}^*(t)$; the electrolyte concentration, $\hat{\boldsymbol{c}}_e(t)$; and an a-priori estimate of the molar flux, $\hat{\boldsymbol{j}}^*(t)$. As shown in Section 3.5, these values can be converted to the open-circuit potential, $\widehat{\boldsymbol{\mathcal{U}}}(t)$, and the electrolyte potential, $\widehat{\boldsymbol{\phi}}_e(t)$. Additionally, the a-priori estimate of the flux, $\hat{\boldsymbol{j}}^*(t)$, can be used to calculate the estimated solid potential, $\widehat{\boldsymbol{\phi}}_s(t)$. These terms combine to form the overpotential, $\widehat{\boldsymbol{\eta}}(t)$; and the exchange current density, $\widehat{\boldsymbol{i}}_0$. The resulting molar flux, $\boldsymbol{j}'^*$, calculated in a similar fashion to Equation (3.187), becomes,

$$\boldsymbol{j}'^{\pm}_{\delta,j} = 2\widehat{\boldsymbol{i}}^{\pm}_{0\delta,j}\sinh\left(\frac{F}{2RT}\widehat{\boldsymbol{\eta}}_{\delta,j}\right) \tag{4.233}$$

where $\boldsymbol{j}'^*$ is a transformation of $\boldsymbol{j}'^{\pm}_{\delta,j}$, such that,

$$T\boldsymbol{j}'^* = \boldsymbol{j}'_\delta \tag{4.234}$$

This emergent molar flux, $\boldsymbol{j}'^*$, is used as the "measured" molar flux described in the a-priori observer discussion, where an error term,

$$\tilde{\boldsymbol{j}}^* = \hat{\boldsymbol{j}}^* - \boldsymbol{j}'^* \tag{4.235}$$

drives the update of the regressor coefficients, as in Equation (4.115). The concept is that as $\tilde{\boldsymbol{j}}^* \to 0$ and the error in the voltage output, $\tilde{V}(t) \to 0$, the system converges to the true states.

4.4.2 Machine Learning with Applications to ABMSs

The final open problem is determining how much of the output voltage error is a function of error in each of the concentrations. The larger this error, the more learning of the states and parameters can be achieved. Referring to Figure 4-30, the error terms, E_s and E_e, are not directly measurable. One means of constructing these vectors is an invertible function of potentials, such that,

$$\boldsymbol{c}'^*_{ss} = f_{\mathcal{U}}^{-1}\left(\boldsymbol{\mathcal{U}}'^*\right) \tag{4.236}$$

$$\boldsymbol{c}'^*_{e} = f_{\phi_e}^{-1}\left(\boldsymbol{\phi}'^*_{e}, I(t)\right) \tag{4.237}$$

These functions exist, but what is unknown is the overpotential that is a summation of the terms, $\mathcal{U}$ and $\boldsymbol{\phi}_e$, and subtracted from the solid potential, $\boldsymbol{\phi}_s$. The only measurable output is the voltage, $V(t)$, which is the difference between the solid potential, $\boldsymbol{\phi}_s$, at the current collectors. Therefore, for every node, i, it is desirable to have a formulation,

$$\mathcal{U}'^*_i = \alpha_i(t)\left(\widehat{\phi}^*_{s,i} - \eta'^*_i\right) \tag{4.238}$$

$$\phi'^*_{e,i} = \beta_i(t)\left(\widehat{\phi}^*_{s,i} - \eta'^*_i\right) \tag{4.239}$$

for $0 \leq \alpha_i(t), \beta_i(t) < 1$ and constrained by $\alpha_i(t) + \beta_i(t) = 1$. Therefore, $\beta_i = 1 - \alpha_i$. Additionally, the overpotential, $\boldsymbol{\eta}'^{*}$, is some component of the solid potential, $\widehat{\boldsymbol{\phi}}_s^{*}$,

$$\eta_i'^{*} = \gamma_i(t)\widehat{\phi}_{s,i}^{*} \tag{4.240}$$

where $0 < \gamma_i(t) < 1$. The solid potential is defined as,

$$\int_0^1 \boldsymbol{v}_i \frac{d^2\boldsymbol{v}_i^{\top}}{d\bar{x}_i^2} d\bar{x}_i \widehat{\phi}_{s,i}^{*} = a^i F \int_0^1 \boldsymbol{v}_i \boldsymbol{v}_i^{\top} d\bar{x}_i \hat{j}_i^{*} \tag{4.241}$$

with boundary conditions,

$$\begin{aligned} \widehat{\phi}_{s,i}^{*}(0^-, t) &= 0 \\ \widehat{\phi}_{s,i}^{*}(0^+, t) &= V(t) \end{aligned} \tag{4.242}$$

The values of $\alpha(t)$, $\beta(t)$ and $\gamma(t)$ are nebulous, time-varying gains that must be estimated. One such way of achieving this end is to construct a machine learning algorithm that uses full knowledge of a simulated system to establish a probability distribution for these terms, to be used in-situ, when only the measured values of current, $I(t)$, and voltage, $V(t)$, are available. Subsequently, the estimated concentration states, $\hat{\boldsymbol{c}}_s^{*}(t)$, $\hat{\boldsymbol{q}}^{*}(t)$ and $\hat{\boldsymbol{c}}_e(t)$, would be supplemented in the implemented version. Using a labeled input layer to the neural network,

$$\begin{bmatrix} V(t) & I(t) & \bar{c}_{s,i}^{*}(t) & q_i^{*}(t) & \boldsymbol{c}_{e,i}^{\top}(t) \end{bmatrix}^{\top} \tag{4.243}$$

and an output layer,

$$\begin{bmatrix} \alpha_i(t) & \gamma_i(t) \end{bmatrix}^{\top} \tag{4.244}$$

a probability distribution can be generated for the outputs of Equation (4.246), as a function of the features shown in Equation (4.243). This is achieved by many simulations to enumerate the myriad hidden layers of this hypothetical system. Subsequently, for the full observer, this same neural network is fed with an input layer of,

$$\left[\begin{array}{ccccc} V(t) & I(t) & \hat{c}^*_{s,i}(t) & \hat{q}^*_i(t) & \hat{\boldsymbol{c}}^\top_{e,i}(t) \end{array}\right]^\top \tag{4.245}$$

to determine the estimated outputs,

$$\left[\begin{array}{cc} \hat{\alpha}_i(t) & \hat{\gamma}_i(t) \end{array}\right]^\top \tag{4.246}$$

in this way, it is possible to determine the overpotential, and its contributions of electrolyte potential and open-circuit potential. Other input features could include filtered current inputs and voltage outputs, similar to the method used to estimate the molar flux. In that way, error vectors, E_s and E_e, can be constructed as,

$$E_{s,i} = \hat{c}^*_{ss,i} - f^{-1}_{\mathcal{U}}\left(\left[1 - \hat{\alpha}_i(t)\hat{\gamma}_i(t)\right]\widehat{\phi}^*_{s,i}\right) \tag{4.247}$$

$$E_{e,i} = \hat{\boldsymbol{c}}_{e,i} - f^{-1}_{\phi_e}\left(\left[1 - \hat{\gamma}_i(t) - \hat{\alpha}_i(t)\hat{\gamma}_i(t)\right]\widehat{\phi}^*_{s,i}, I(t)\widehat{\phi}^*_{s,i}\right) \tag{4.248}$$

for $i \in [1 \cdots N]$. Previously in literature [24] [23], methods for determining the overpotential of the single-particle model have been established, but the challenge facing higher order models is a non-definite electrolyte concentration. These states need to be estimated, and there is no directly invertible Butler-Volmer kinetics.

THIS PAGE INTENTIONALLY LEFT BLANK

Chapter 5

Conclusion

The sections of this thesis are presented to give the reader a reasonably complete understanding of the state of the art with respect to battery management systems. The importance of Li-ion battery cells is increasing as consumers demand highly mobile technologies requiring high energy density power storage. This has been an intense area of focus in literature, and an overview of batteries is presented in Chapter 1. Yet this demand is met with another challenge, beyond the chemistry required to suit these needs: estimating the performance and life of these cells once deployed. Just as a conventional internal combustion vehicle needs a gas gauge, so too does a high performance battery.

The concept of a state and parameter estimator, for the purposes of informed control, is achieved through the implementation of a battery management system (BMS), as discussed in Chapter 2. Conventionally, a BMS is constructed by linearizing a variety of the models presented in Chapter 3, but the linearization of these models can only produce accurate results if the discharging or charging profile does not include high currents relative to the capacity of the battery, notionally $I(t) \leq 1C$. Therefore, in the interest of safety and efficiency, better models need to be constructed with the intention of control and estimation as a focus during their design. Additionally, adaptive observers need to be designed using these models as a basis for estimation, such that metrics like the state of charge (SoC) and state of health (SoH) can be determined.

5.1 Summary of Results

This thesis works to solve the latter two problems addressed above. It is shown in Chapter 3 the complete formulation of a high accuracy battery model, established by previous work [5], with new features such as improved computational efficiency and agnostic determination of diffusion characteristics. This thesis goes on to further reduce the order of the model, as described in Section 3.5, without significant reduction of accuracy in the results, as shown in Table 3.2 and 3.3. This novel Li-ion model, known as the ANCF II, leverages mixed basis functions to ensure high accuracy results, while reducing the degrees of freedom for less critical states. This model is shown to have sufficient accuracy for the purposes of adaptive observer design.

Once the accuracy of the new model is shown, this thesis continues by creating foundational adaptive observers for the dynamic plant of the ANCF II model in Chapter 4. Section 4.3.1 describes the construction of an adaptive observer for the solid electrode, using a novel combination of spatio-temporal filters for the purpose of the matrix regressor construction. Section 4.3.2 shows the novel construction of an a-priori estimate of molar flux using output voltage measurements, and a set of filtered input current values. Finally, Section 4.3.3 shows the novel construction of a Jacobian MIMO adaptive observer, intended to learn a subset of parameters used to define a known system matrix. This allows all learning to be confined to the space of unknowns.

5.2 Future Work

The future of this research effort is briefly described in Section 4.4. The adaptive observers presented in Chapter 4 define parameter estimation of the dynamic states, but the error vector that defines the progression of the parameter estimation is not directly measurable as an output. Therefore, it is suggested to implement a machine learning algorithm to determine the error vector relative to both the solid concentration states and the electrolyte concentration states. This algorithm could implement a neural network that takes the measured output voltage and input current, as well as the current state estimates, as an input layer, and provide a fractional coefficient vector as an output layer to define the various potentials within the cell. The key in this formulation is that there needs to be a high enough correlation between the truly measurable values and the output layer, with minimal dependency on the current state values. To ensure this, additional filters of the input current, $I(t)$, can be provided for the input layer.

Once this inversion process is achieved, a full adaptive observer for the ANCF II model will have been constructed. Using this observer, a system designer can implement new, previously intractable control algorithms based on higher fidelity cell information. Such an availability will greatly increase the capability of a given cell, especially in severe contexts such as that of an electric vehicle, while subsequently reducing the cost of implementation by ensuring a cell is properly sized. It is within this framework that the next generation of mobile technology will transcend the limitations currently facing batteries and their management, allowing wider adoption of low-cost, high capacity energy storage, while guaranteeing safe and enduring operation.

THIS PAGE INTENTIONALLY LEFT BLANK

Bibliography

[1] Milton Abramowitz and Irene A Stegun. *Handbook of Mathematical Functions with Formulas, Graphs, and Mathematical Tables.* National Bureau of Standards Applied Mathematics Series - 55, 1964.

[2] Anuradha M Annaswamy, Fredrik P Skantze, and Ai-Poh Loh. Adaptive control of continuous time systems with convex/concave parametrization. *Automatica*, 34(1):33–49, 1998.

[3] Pankaj Arora, Marc Doyle, and Ralph E White. Mathematical modeling of the lithium deposition overcharge reaction in lithium-ion batteries using carbon-based negative electrodes. *Journal of the Electrochemical Society*, 146(10):3543–3553, 1999.

[4] Mordecai Avriel. *Nonlinear programming: analysis and methods.* Courier Corporation, 2003.

[5] Pierre Bi. *Control-oriented modeling and adaptive parameter estimation of a Lithium ion intercalation cell.* Master's thesis, Massachusetts Institute of Technology, 2015.

[6] Pierre Y Bi, Anuradha M Annaswamy, and Aleksandar Kojic. Control-oriented modeling and adaptive parameter estimation of a Lithium ion intercalation cell. *Conference on Decision and Control*, pages 7322–7328, 2015.

[7] Long Cai and Ralph E. White. An Efficient Electrochemical–Thermal Model for a Lithium-Ion Cell by Using the Proper Orthogonal Decomposition Method. *Journal of the Electrochemical Society*, 157(11):A1188–A1195, 2010.

[8] Long Cai and Ralph E. White. Lithium ion cell modeling using orthogonal collocation on finite elements. *Journal of Power Sources*, 217:248–255, 2012.

[9] Chengyu Cao, Anuradha M Annaswamy, and Aleksandar Kojic. Parameter convergence in nonlinearly parameterized systems. *IEEE Transactions on automatic control*, 48(3):397–412, 2003.

[10] R Carroll and D Lindorff. An adaptive observer for single-input single-output linear systems. *IEEE Transactions on Automatic Control*, 18(5):428–435, 1973.

[11] Nalin A. Chaturvedi, Reinhardt Klein, Jake Christensen, Jasim Ahmed, and Aleksandar Kojic. Algorithms for advanced battery-management systems. *IEEE Control Systems Magazine*, 30(3):49–68, 2010.

[12] Domenico Di Domenico, Anna Stefanopoulou, and Giovanni Fiengo. Lithium-Ion Battery State of Charge and Critical Surface Charge Estimation Using an Electrochemical Model-Based Extended Kalman Filter. *Journal of Dynamic Systems, Measurement, and Control*, 132(6):061302, 2010.

[13] Camila Domonoske. Half A Million 'Hoverboards' Recalled Over Risk Of Fire, Explosions. *National Public Radio*, July 2016.

[14] Marc Doyle. Comparison of Modeling Predictions with Experimental Data from Plastic Lithium Ion Cells. *Journal of The Electrochemical Society*, 143(6):1890, 1996.

[15] Marc Doyle, Thomas F. Fuller, and John Newman. Modeling of Galvanostatic Charge and Discharge of the Lithium/Polymer/Insertion Cell. *Journal of The Electrochemical Society*, 140(6):1526, 1993.

[16] Guodong Fan, Ke Pan, and Marcello Canova. A Comparison of Model Order Reduction Techniques for Electrochemical Characterization of Lithium-ion Batteries. *Conference on Decision and Control*, pages 3922–3931, 2015.

[17] Bernard Friedland. *Control system design: an introduction to state-space methods*. Courier Corporation, 2012.

[18] Thomas F. Fuller. Simulation and Optimization of the Dual Lithium Ion Insertion Cell. *Journal of The Electrochemical Society*, 141(1):1, 1994.

[19] Xuebing Han, Minggao Ouyang, Languang Lu, and Jianqiu Li. Simplification of physics-based electrochemical model for lithium ion battery on electric vehicle. Part II: Pseudo-two-dimensional model simplification and state of charge estimation. *Journal of Power Sources*, 278:814–825, 2015.

[20] Xiaosong Hu, Shengbo Li, and Huei Peng. A comparative study of equivalent circuit models for li-ion batteries. *Journal of Power Sources*, 198:359–367, 2012.

[21] Yiran Hu, S Yurkovich, Y Guezennec, and BJ Yurkovich. Electro-thermal battery model identification for automotive applications. *Journal of Power Sources*, 196(1):449–457, 2011.

[22] Petros A Ioannou and Jing Sun. *Robust adaptive control*. Courier Corporation, 2012.

[23] Benjamin Jenkins, Anuradha M Annaswamy, and Aleksandar Kojic. Matrix Regressor Adaptive Observers for Battery Management Systems. *Conference on Decision and Control*, pages 707–714, 2015.

[24] Benjamin Jenkins, Anuradha M Annaswamy, and Aleksandar Kojic. Matrix regressor adaptive observers for battery management systems. In *Intelligent Control (ISIC), 2015 IEEE International Symposium on*, pages 707–714. IEEE, 2015.

[25] Arjun Kharpal. Samsung's Galaxy Note 7 Phones Caught Fire because of the "Aggressive" Battery Design: Report. *CNBC*, December 2016.

[26] L Gordon Kraft. Controllable form state variables obtained from an arbitrarily fast adaptive observer. In *Decision and Control including the 15th Symposium on Adaptive Processes, 1976 IEEE Conference on*, volume 15, pages 1088–1094. IEEE, 1976.

[27] Gerhard Kreisselmeier. Adaptive observers with exponential rate of convergence. *IEEE transactions on automatic control*, 22(1):2–8, 1977.

[28] Yuang-Shung Lee and Ming-Wang Cheng. Intelligent control battery equalization for series connected lithium-ion battery strings. *IEEE Transactions on Industrial Electronics*, 52(5):1297–1307, 2005.

[29] Gerd Luders and K Narendra. An adaptive observer and identifier for a linear system. *IEEE Transactions on Automatic Control*, 18(5):496–499, 1973.

[30] James F Manwell and Jon G McGowan. Lead acid battery storage model for hybrid energy systems. *Solar Energy*, 50(5):399–405, 1993.

[31] James Marcicki, Marcello Canova, A. Terrence Conlisk, and Giorgio Rizzoni. Design and parametrization analysis of a reduced-order electrochemical model of graphite/LiFePO4 cells for SOC/SOH estimation. *Journal of Power Sources*, 237:310–324, 2013.

[32] Donald W Marquardt. An algorithm for least-squares estimation of nonlinear parameters. *Journal of the Society for Industrial and Applied Mathematics*, 11(2):431–441, 1963.

[33] Christopher Mayhew, Wei He, Christoph Kroener, Reinhardt Klein, Nalin Chaturvedi, and Aleksandar Koji. Investigation of projection-based model-reduction techniques for solid-phase diffusion in Li-ion batteries *. pages 123–128, 2014.

[34] Jad Mouawad. Report on Boeing 787 Dreamliner Battery Flaws Finds Lapses at Multiple Points. *The New York Times*, December 2014.

[35] Scott J Moura. Estimation and Control of Battery Electrochemistry Models: A Tutorial. *Conference on Decision and Control*, pages 3906–3912, 2015.

[36] Scott J Moura, Nalin A Chaturvedi, and Miroslav Krstić. Adaptive partial differential equation observer for battery state-of-charge/state-of-health estimation via an electrochemical model. *Journal of Dynamic Systems, Measurement, and Control*, 136(1):011–015, 2014.

[37] K S Narendra and A M Annaswamy. *Stable Adaptive Systems*. Prentice-Hall Information and System Sciences Series. Prentice Hall, Englewood Cliffs, 1989.

[38] John Newman. FORTRAN Programs for the Simulation of Electrochemical Systems, 1998.

[39] John Newman and Karen E. Thomas-Alyea. *Electrochemical Systems*. 2004.

[40] Kong Soon Ng, Chin-Sien Moo, Yi-Ping Chen, and Yao-Ching Hsieh. Enhanced coulomb counting method for estimating state-of-charge and state-of-health of lithium-ion batteries. *Applied energy*, 86(9):1506–1511, 2009.

[41] Gang Ning and Branko N. Popov. Cycle Life Modeling of Lithium-Ion Batteries. *Journal of The Electrochemical Society*, 151(10):A1584, 2004.

[42] Björn Nykvist and Måns Nilsson. Rapidly falling costs of battery packs for electric vehicles. *Nature Climate Change*, 5(4):329–332, 2015.

[43] Sabine Piller, Marion Perrin, and Andreas Jossen. Methods for state-of-charge determination and their applications. *Journal of power sources*, 96(1):113–120, 2001.

[44] Saeed Khaleghi Rahimian, Sean Rayman, and Ralph E White. Extension of physics-based single particle model for higher charge/discharge rates. *Journal of Power Sources*, 224:180–194, 2013.

[45] Tom Randall. Here's how electric cars will cause the next oil crisis, February 2016. [Online; posted 25-February-2016].

[46] Venkat Rao, Gaurav Singhal, Anshul Kumar, and Nicolas Navet. Battery model for embedded systems. In *VLSI Design, 2005. 18th International Conference on*, pages 105–110. IEEE, 2005.

[47] Shriram Santhanagopalan, Qingzhi Guo, Premanand Ramadass, and Ralph E. White. Review of models for predicting the cycling performance of lithium ion batteries. *Journal of Power Sources*, 156(2):620–628, 2006.

[48] Shriram Santhanagopalan and Ralph E. White. Online estimation of the state of charge of a lithium ion cell. *Journal of Power Sources*, 161:1346–1355, 2006.

[49] Bruno Scrosati. History of lithium batteries. *Journal of solid state electrochemistry*, 15(7-8):1623–1630, 2011.

[50] Ahmed A. Shabana and Refaat Y. Yakoub. Three Dimensional Absolute Nodal Coordinate Formulation for Beam Elements: Theory. *Journal of Mechanical Design*, 123(4):606, 2001.

[51] Ehsan Shafiei, Hedinn Thorkelsson, Eyjólfur Ingi Ásgeirsson, Brynhildur Davidsdottir, Marco Raberto, and Hlynur Stefansson. An agent-based modeling approach to predict the evolution of market share of electric vehicles: a case study from iceland. *Technological Forecasting and Social Change*, 79(9):1638–1653, 2012.

[52] Kandler A. Smith, Christopher D. Rahn, and Chao Yang Wang. Control oriented 1D electrochemical model of lithium ion battery. *Energy Conversion and Management*, 48(9):2565–2578, 2007.

[53] Gilbert Strang. *Introduction to Applied Mathematics*. Cambridge Press, Wellesley, MA, 1 edition, 1986.

[54] Venkat R. Subramanian, Vinten D. Diwakar, and Deepak Tapriyal. Efficient Macro-Micro Scale Coupled Modeling of Batteries. *Journal of The Electrochemical Society*, 152(10):A2002, 2005.

[55] Shuxia Tang, Yebin Wang, Zafer Sahinoglu, Toshihiro Wada, Satoshi Hara, and Miroslav Krstic. State-of-charge estimation for lithium-ion batteries via a coupled thermal-electrochemical model. In *2015 American Control Conference (ACC)*, pages 5871–5877. IEEE, 2015.

[56] J-M Tarascon and Michel Armand. Issues and challenges facing rechargeable lithium batteries. *Nature*, 414(6861):359–367, 2001.

[57] K Thomas, John Newman, and R Darling. Mathematical Modeling of Lithium Batteries. In Springer-Verlag, editor, *Advances in Lihium-ion Batteries*, pages 345–392. New York, NY, 2002.

[58] Mark W Verbrugge and Robert S Conell. Electrochemical and thermal characterization of battery modules commensurate with electric vehicle integration. *Journal of the Electrochemical Society*, 149(1):A45–A53, 2002.

[59] Mark W Verbrugge and Ping Liu. Electrochemical characterization of high-power lithium ion batteries using triangular voltage and current excitation sources. *Journal of Power Sources*, 174(1):2–8, 2007.

[60] Dan Wang, Shaoyun Ge, Hongjie Jia, Chengshan Wang, Yue Zhou, Ning Lu, and Xiangyu Kong. A demand response and battery storage coordination algorithm for providing microgrid tie-line smoothing services. *IEEE Transactions on Sustainable Energy*, 5(2):476–486, 2014.

[61] Refaat Y. Yakoub and Ahmed A. Shabana. Three Dimensional Absolute Nodal Coordinate Formulation for Beam Elements: Implementation and Applications. *Journal of Mechanical Design*, 123(4):614, 2001.